TESIS DE LA UNIVERSIDAD DE ZARAGOZA

2024 385

Lorena Grima Soriano

Nuevas funcionalidades de materiales cerámicos procesados por láser en el campo de la energía y la salud

Director/es
Peña Torre, José Ignacio
Sanjuan Alvarez, María Luisa

ISSN 2254-7606

Prensas de la Universidad Universidad Zaragoza

Universidad de Zaragoza
Servicio de Publicaciones

ISSN 2254-7606

Universidad Zaragoza
1542

Tesis Doctoral

NUEVAS FUNCIONALIDADES DE MATERIALES CERÁMICOS PROCESADOS POR LÁSER EN EL CAMPO DE LA ENERGÍA Y LA SALUD

Autor

Lorena Grima Soriano

Director/es

Peña Torre, José Ignacio
Sanjuan Alvarez, María Luisa

UNIVERSIDAD DE ZARAGOZA
Escuela de Doctorado

Programa de Doctorado en Física

2024

Tesis Doctoral

Nuevas funcionalidades de materiales cerámicos procesados por láser en el campo de la energía y la salud

Autor

Lorena Grima Soriano

Director/es

María Luisa Sanjuán Álvarez
José Ignacio Peña Torre

Instituto de Nanociencia y Materiales de Aragón

2024

La presente tesis doctoral con título ***"Nuevas funcionalidades de materiales cerámicos procesados por láser en el campo de la energía y la salud"*** se presenta como una tesis por compendio de publicaciones, todas ellas publicadas antes del depósito de la tesis.

Las referencias de las mismas son:

- L. Grima, J.I. Peña, M.L. Sanjuán, Pyrochlore-like ZrO_2-PrO_x compounds: The role of the processing atmosphere in the stoichiometry, microstructure and oxidation state, Journal of Alloys and Compounds **923**, 166449 (2022)
- L. Grima, J.I. Peña, M.L. Sanjuán, Ceramics with eutectic microstructure in the ZrO_2–PrO_x system. Journal of the American Ceramic Society **106**, 7098–7108 (2023)
- L. Grima, G.A. Mutch, P.B. Oliete, W. Bucheli, R.I. Merino, E.I. Papaioannou, J.J. Bailey, M.D. Kok, D.J.L. Brett, P.R. Shearing, I.S. Metcalfe, M.L. Sanjuán, High CO_2 permeability in supported molten-salt membranes with highly dense and aligned pores produced by directional solidification, Journal of Membrane Science **630**, 119057 (2021)
- L. Grima, M. Díaz-Pérez, J. Gil Cortés, D. Sola, J.I. Peña, Generation of a porous scaffold with a starting composition in the CaO-SiO_2-MgO-P_2O_5 system in a simulated physiological environment, Applied Sciences 10, 312 (2020)

Resumen

Durante la realización de este trabajo, se implementó la técnica de fusión zonal láser con el objetivo de obtener muestras con aplicaciones potenciales en los sectores de energía y salud.

La aplicación de esta técnica permitió examinar áreas específicas dentro del diagrama de fases PrO_x-ZrO_2. En este contexto, se analizaron muestras con una composición cercana a la relación estequiométrica Pr/Zr, así como composiciones más enriquecidas en Pr, bajo diversas condiciones de procesamiento láser. La combinación de estos estudios con la caracterización estructural y microestructural facilitó una comprensión más profunda de cómo las condiciones de crecimiento láser inciden en la estructura y microestructura de las muestras resultantes. Además, se pudo observar cómo la composición resultante de las muestras podría influir en la capacidad catalítica de los dispositivos generados.

Por otra parte, se llevó a cabo la síntesis de muestras que incorporaban una fase de MgO, la cual, bajo condiciones específicas, demostró la capacidad de experimentar una disolución, dando origen a la formación de estructuras porosas. La habilidad de estas estructuras para proporcionar un entorno poroso y controlado ofrece oportunidades significativas para diseñar y optimizar materiales con propiedades aplicables en varios campos, como la formación de membranas duales con separación selectiva al CO_2, así como la obtención de implantes óseos.

ÍNDICE

Contenido

1. Introducción

La presente memoria recoge la investigación realizada en dos ámbitos, aparentemente disjuntos, relacionados con la salud y el medio ambiente, respectivamente. El nexo común es la utilización de la técnica de solidificación direccional mediante láser para la obtención de materiales con nuevas funcionalidades.

Las dos primeras partes de la tesis están enfocadas hacia la producción y caracterización de materiales con el fin último de reducir el efecto de gases contaminantes en el medio ambiente.

En la actualidad, se observa con creciente claridad que el impacto humano en el entorno planetario es de carácter irreversible. La progresión del fenómeno del calentamiento global, la alarmante extinción de numerosas especies tanto animales como vegetales, y la contaminación generalizada de los recursos hídricos, los suelos y la atmósfera, arrojan luz sobre la posibilidad de un colapso ecológico, cuyas consecuencias serían de una magnitud devastadora.

La emisión constante de gases contaminantes y de efecto invernadero a la atmósfera conlleva un grave deterioro de la calidad ambiental y, por ende, de la pureza del aire que respiramos. Este proceso también ha provocado un aumento considerable de la temperatura media del planeta. Desde finales del siglo XIX, la temperatura promedio de la Tierra ha experimentado un incremento de 1.2°C y es relevante señalar que los últimos siete años han sido testigos de las temperaturas más elevadas registradas en la historia. Según la Organización Meteorológica Mundial (OMM), existe la posibilidad de que durante este año 2024 alcancemos valores de temperatura media global

incompatible con la supervivencia de muchas especies de flora y fauna, como los arrecifes de coral, un hecho que ha sido advertido durante años por el Grupo Intergubernamental de Expertos sobre el Cambio Climático (IPCC).[1]

Ante esta preocupante coyuntura, se plantean tres alternativas fundamentales:

a) Reducción de las emisiones de gases contaminantes o de efecto invernadero, como el CO_2, el CH_4, los NO_x, etc.

b) Implementación de métodos destinados a la captura y almacenamiento del CO_2, que abarcan desde el almacenamiento subterráneo hasta su depósito en los océanos, así como reacciones químicas con sales u óxidos de metales alcalinos y alcalinotérreos para la formación de carbonatos sólidos.

c) Reutilización del CO_2 generado en el proceso de combustión de combustibles fósiles como fuente de energía alternativa.[2,3]

Estas opciones representan enfoques cruciales para mitigar los efectos adversos del cambio climático y la degradación ambiental en curso, y requieren una acción concertada a nivel global para lograr un impacto significativo en la sostenibilidad de nuestro planeta.

En la última parte de la tesis se aborda el uso de la técnica de fusión zonal por láser para la producción de estructuras porosas biocompatibles, generadas in situ, que puedan utilizarse en injertos o implantes en el cuerpo humano. El incremento en la edad de la población conlleva una mayor prevalencia de patologías musculoesqueléticas, tales como fracturas, osteoporosis e infecciones y tumores óseos.

Las terapias convencionales, como el uso de autoinjertos, aloinjertos y xenoinjertos, presentan limitaciones inherentes, como la disponibilidad limitada de hueso, problemas de rechazo del injerto y riesgos de transmisión de enfermedades. Aunque se han empleado implantes y dispositivos biomédicos para sustituir huesos y articulaciones, estas soluciones enfrentan limitaciones como fatiga, fracturas, toxicidad y desgaste. Además, el comportamiento de estos implantes y dispositivos no satisface completamente los requisitos específicos del tejido óseo.[4-6]

Por ello se ha detectado la necesidad de emplear matrices porosas, conocidas como andamios, que proporcionan soporte estructural y mecánico para la adhesión y proliferación celular. Dicha necesidad radica en la capacidad de estos dispositivos para ofrecer una solución más integral y personalizada para abordar defectos óseos, promoviendo una regeneración guiada y mejorando la integración a largo plazo. Además, permiten la entrega controlada de factores de crecimiento y medicamentos, lo que puede acelerar el proceso de curación y mejorar la funcionalidad del tejido regenerado. Los andamios o *scaffolds* proporcionan un soporte estructural que guía el crecimiento y la regeneración del tejido óseo.

2. Objetivos de la tesis

El objetivo principal de esta tesis se centra en la investigación de materiales cerámicos que han sido procesados mediante técnicas basadas en la fusión y solidificación direccional mediante láser, con un enfoque específico en su aplicación en biomedicina y en el cuidado del medio ambiente.

Para alcanzar este objetivo principal, se han establecido los siguientes objetivos específicos:

1. El **primer objetivo** de la tesis está orientado hacia la disminución de la cantidad de gases de combustión contaminantes liberados a la atmósfera. Para ello se van a estudiar las propiedades estructurales de algunos compuestos del sistema PrO_x-ZrO_2 y la relación entre su estructura y la valencia mixta del Pr. Los materiales estudiados en este punto se plantean como posibles soportes para catalizadores de tres vías (TWC, de *three way catalysts*) en vehículos de combustión por sus propiedades como compuestos para almacenamiento de oxígeno (OSC, de *oxygen storage compounds*).
2. El **segundo objetivo** de la tesis consiste en la fabricación mediante fusión con láser de materiales densos que contengan óxido de magnesio como una de sus fases, de modo que, tras la disolución de este último, den lugar a estructuras porosas aplicables en diferentes campos relacionados con la salud y el medio ambiente.

   Para ello se ha llevado a cabo, en primer lugar, la producción, a modo de "prueba de concepto", de una membrana dual densa que sea selectiva al dióxido de carbono (CO_2). Este proceso se basa en la infiltración de carbonatos fundidos en una matriz porosa que se obtendrá a partir de un eutéctico fibrilar solidificado direccionalmente. Esta membrana podría tener aplicaciones en la captura y separación de CO_2, lo que contribuiría a abordar los desafíos asociados con las emisiones de gases de efecto invernadero.

   En segundo lugar, se ha fabricado un material denso que, en contacto con sistemas fisiológicos, dé lugar a un *scaffold* poroso que combine las ventajas mecánicas de un soporte denso con la necesidad biológica de la inclusión de

poros en un implante óseo. Controlando el tamaño de los poros del implante se podría llegar a producir la infiltración de células óseas, como osteoblastos y osteocitos, contribuyendo así al proceso de osteointegración, así como el crecimiento de vasos sanguíneos en el interior del implante, lo que favorece la irrigación del tejido. Este implante óseo proporcionaría un sustrato tridimensional que sirve como andamio para la adhesión de células óseas y la formación de nueva estructura ósea, facilitando así la regeneración del hueso en el área afectada.

2.1. Objetivo 1: Estudio de la interconexión entre la composición, estructura, propiedades y estado de oxidación de muestras del sistema PrO_x-ZrO_2.

El funcionamiento de un vehículo convencional o de combustión interna se basa en la reacción de un combustible con el oxígeno. La conversión de la energía química en energía mecánica permite poner en funcionamiento el vehículo, pero a costa de la emisión de gases nocivos que se conocen como gases de escape.

En el caso de una combustión estequiométrica de un hidrocarburo (HC), los únicos productos de la combustión deberían ser CO_2 y H_2O. Sin embargo, esta combustión ideal no siempre tiene lugar, y puede producirse una combustión incompleta, ya sea debido a la falta o al exceso de O_2, que da lugar a nuevos productos como CO, NO_x e hidrocarburos no consumidos.

Los **óxidos de nitrógeno (NO_x)** son uno de los productos más tóxicos emitidos durante la combustión en nuestros motores; se forman debido al exceso de oxígeno en la combustión, que se combina con el nitrógeno del aire. Los NO_x son muy nocivos para

la salud y, en exposición elevada y continuada, pueden provocar cáncer. Además, contribuyen a la destrucción de la capa de ozono, ya que tanto el NO como el NO_2 pueden reaccionar con el ozono (O_3) presente en la capa de ozono formando NO_3, lo que disminuye la concentración de O_3. El NO_3 por su parte puede reaccionar con el hidrógeno de la atmósfera para dar lugar a HNO_3 y el llamado *smog* fotoquímico.

Los catalizadores de tres vías (TWC) son los encargados de transformar los gases de escape producidos por combustión incompleta (CO, NO_x y HC no consumidos) en CO_2, H_2O y N_2. Un TWC debe promover simultáneamente la oxidación del CO y de los HC a CO_2 y H_2O y la reducción de los óxidos nitrosos a N_2 mediante las reacciones (1-3):

$$CO + ½\ O_2 \rightarrow CO_2 \qquad (1)$$

$$C_nH_{2n+2} + (3n+1)/2O_2 \rightarrow nCO_2 + (n+1)\ H_2O \qquad (2)$$

$$2NO_x + 2xCO \rightarrow N_2 + 2xCO_2 \qquad (3)$$

Un TWC se compone habitualmente de un monolito que suele ser de alúmina y un recubrimiento cerámico que incluye un metal precioso y un soporte cerámico con propiedades OSC, cuya función es promover la reacción catalítica almacenando o suministrando oxígeno según se requiera. El fundamento de la OSC es la combinación de la reacción redox de una tierra rara, habitualmente Ce, y el transporte de oxígeno. El material de referencia es el CeO_2, normalmente en solución sólida con otros óxidos,[7-12] y su uso se basa en la expresión (4) (en notación de Kröger–Vink):

$$2Ce^{4+} + O_O + 2e^- \leftrightarrow 2Ce^{3+} + ½O_2(g) + V_O^{\bullet\bullet} \qquad (4)$$

donde O_O y $VO^{\bullet\bullet}$ representan un oxígeno de la red y una vacante de oxígeno, respectivamente.

La solución sólida de la ceria con otros óxidos pretende mejorar su capacidad de almacenamiento de oxígeno, así como su estabilidad al someterlo a altas temperaturas. Para estabilizar la ceria habitualmente se usa circonio, siendo las composiciones intermedias de Ce/Zr las más apropiadas para aplicaciones catalíticas. El sistema CeO_2-ZrO_2 (CZO) presenta el problema de que no hay compuestos de equilibrio para composiciones intermedias. De acuerdo con el diagrama de fases (DF) (figura 1) del sistema CZO, exhaustivamente estudiado por Yashima et al.,[13] la solubilidad de un compuesto en el otro en fases estables es despreciable, aunque es posible en fases metaestables.

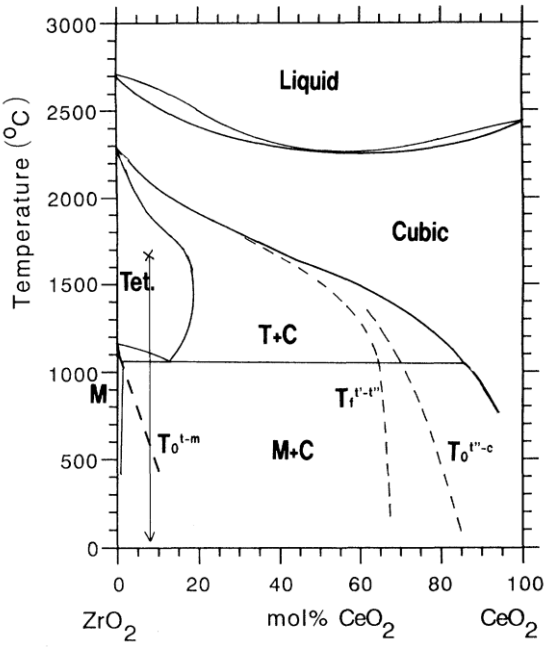

Figura 1. PD del sistema CZO. Las líneas continuas indican las fases estables y las discontinuas las fases metaestables.

Insertar praseodimio en compuestos de Ce mejora su OSC y además permite trabajar a temperaturas menores que en el caso de la ceria, ya que el intercambio de oxígeno se produce a temperaturas más bajas.[14-18] Además, evita la de-activación a alta temperatura observada en la ceria. Los compuestos de tipo $Ce_{1-x}Pr_xO_2$ no sólo tienen aplicación como TWC, sino que sus propiedades redox los hacen susceptibles de ser utilizados en otros muchos dispositivos que requieran almacenamiento y liberación de O_2 en función de las condiciones ambientales. En cuanto al sistema PrO_2/ZrO_2, los pocos trabajos publicados concluyen que el Pr aporta una mayor OSC.[19]

El objetivo de esta parte de la tesis consiste en la producción y caracterización de compuestos del sistema PrO_x-ZrO_2 que puedan utilizarse, entre otras aplicaciones, como soporte de catalizadores de tres vías (TWC) para la supresión o modificación de gases nocivos emitidos por los automóviles, tales como CO, hidrocarburos (HC) no consumidos y NO_x.

Los óxidos mixtos de praseodimio y circonio han surgido como una opción prometedora en la búsqueda de materiales eficientes para la captura y liberación controlada de oxígeno en diversas aplicaciones. La capacidad de los materiales a base de praseodimio para cambiar su estado de oxidación de Pr^{3+} a Pr^{4+} y viceversa facilita la absorción y liberación controlada de oxígeno, lo que los convierte, a priori, en sistemas OSC análogos a los compuestos de cerio. La reacción redox del praseodimio equivalente a del cerio se observa en la expresión (5):

$$2Pr^{4+} + O_O + 2e^- \leftrightarrow 2Pr^{3+} + \tfrac{1}{2}O_2(g) + VO^{\bullet\bullet} \qquad (5)$$

Además, el óxido de circonio (ZrO_2) actúa como un soporte estructural crucial, proporcionando estabilidad y facilitando la difusión de oxígeno a través de la matriz.

Las propiedades de conducción de oxígeno (OSC) del sistema ZrO_2–PrO_x han sido objeto de estudio, tanto en composiciones próximas a la región de pirocloro $Pr_2Zr_2O_7$ como en la región enriquecida en Pr[20-23]. En términos generales, los mejores resultados, en cuanto a consumo de H_2 en experimentos de TPR, se obtienen en compuestos con una estructura similar a la fluorita y con contenidos de Pr iguales o superiores al 75%.

La capacidad de ajustar las propiedades del sistema mediante la variación de la relación PrO_x/ZrO_2 abre nuevas posibilidades para adaptar el material a requisitos específicos de diferentes aplicaciones.

En este trabajo, hemos llevado a cabo un estudio de materiales del sistema ZrO_2–PrO_x. Como se puede observar en la figura 2, existen discrepancias o ambigüedades entre diversos diagramas de fases publicados para este sistema, especialmente en las regiones de alta temperatura. La razón más evidente de dichas discrepancias es la dificultad en el control de la valencia del Pr.

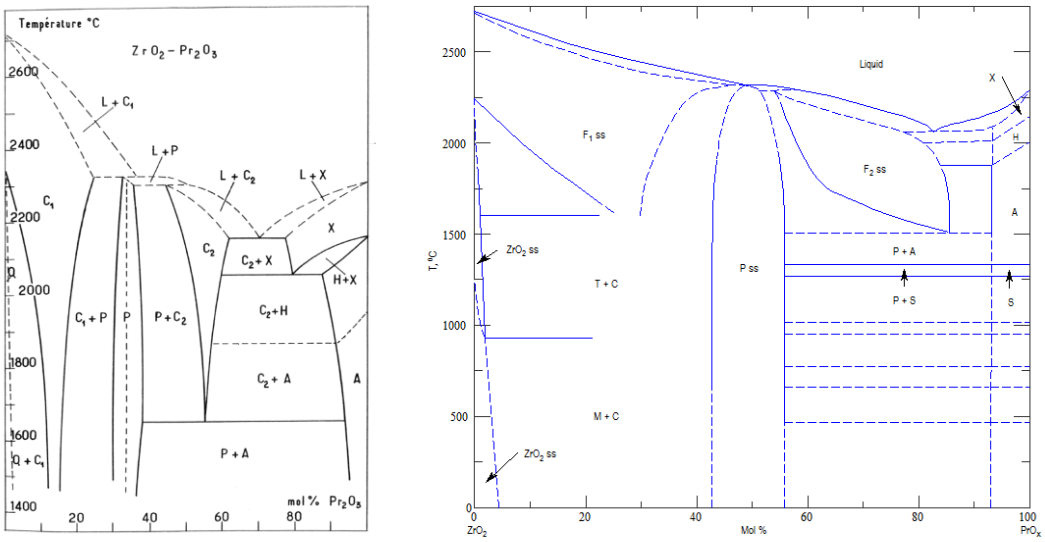

Figura 2. Diagrama de fases del sistema ZrO_2-Pr_2O_3 (o PrO_x) publicado por Rouanet[24] (a) y porKrasil'nikov[25] (b).

Con el fin de estudiar la influencia del estado de oxidación del Pr en la formación de unas fases u otras, en este trabajo se ha llevado a cabo un estudio en dos regiones de composiciones del sistema ZrO_2-PrO_x. Las muestras se han obtenido utilizando una técnica de fusión y solidificación asistida por láser en atmósfera controlada, con el fin de identificar las fases formadas en un rango de condiciones ambientales, que abarcan desde condiciones más oxidantes hasta menos oxidantes.

La primera de ellas es la región de la solución sólida en torno al 50%. En esta región se han estudiado la composición estequiométrica $Pr_2Zr_2O_7$ y las composiciones límite según el diagrama de la figura 2 (b), $Pr_{1.7}Zr_{2.3}O_{7+x}$ y $Pr_{2.24}Zr_{1.76}O_{7-x}$.

La estructura de las muestras esperada para estas composiciones es una estructura tipo pirocloro, que pasamos a describir a continuación.

Estructura pirocloro

La disposición cristalina de los compuestos de composición $A_2B_2O_7$ y estructura de tipo pirocloro (con grupo espacial Fd-3m) puede comprenderse como una superestructura de la fluorita, en la que tanto los cationes como los aniones se ordenan en dos sitios cristalográficos diferentes.[26] El catión A se une a ocho átomos de oxígeno y ocupa el sitio 16d, mientras que el catión B presenta coordinación octaédrica y se sitúa en el sitio 16c. Aunque presentan la misma simetría puntual, los sitios 16c y 16d no son equivalentes cristalográficamente. Los átomos de oxígeno ocupan dos sitios distintos, 48f (O(1)) y 8b (O(2)), que están coordinados tetraédricamente por dos cationes B y dos cationes A (el O(1)), o por cuatro cationes A (el O(2)), como se observa en la figura 3.

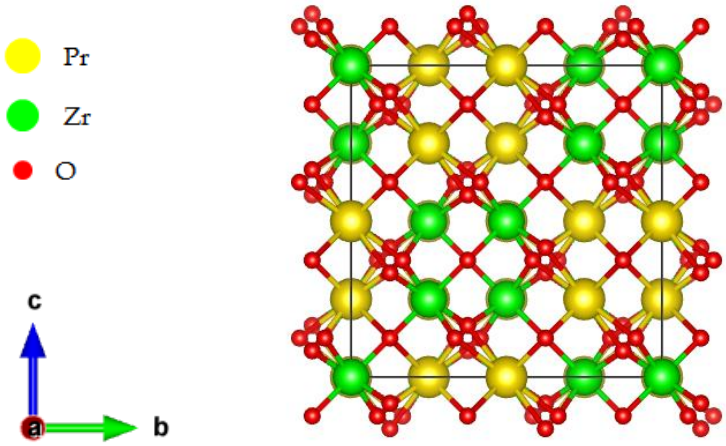

Figura 3. Estructura tridimensional de compuestos $A_2B_2O_7$ de tipo pirocloro.

Un tercer sitio de anión, normalmente no ocupado (8a), se encuentra coordinado tetraédricamente con cuatro cationes B. En pirocloros defectivos o con desorden puede ocurrir que el sitio 8a esté parcialmente ocupado, debido a la falta de estequiometría o al desorden catiónico. En pirocloros en los que el catión A es una tierra rara con

propiedades de valencia mixta, como Ce o Pr, la ocupación parcial del sitio 8a también puede producirse para compensar un mayor estado de oxidación de la tierra rara, pudiendo usarse como indicador del grado de oxidación de la muestra.

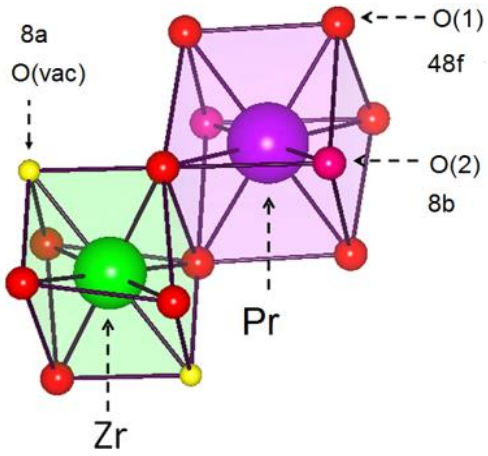

Figura 4. Representación de los sitios cristalográficos ocupados por Pr y Zr en una estructura pirocloro.

El $Pr_2Zr_2O_7$ es un ejemplo característico de pirocloro ordenado, es decir sin intercambio de sitios catiónicos. La figura 4 muestra los entornos catiónicos de Pr y Zr en este compuesto.

Además de compuestos con composición cercana a la del pirocloro, se han estudiado composiciones más ricas en Pr, como $Pr_{2.4}Zr_{1.6}O_x$ y Pr_3ZrO_x, fuera del campo de soluciones sólidas con estructura pirocloro. Asimismo, se ha estudiado la evolución de la composición y la microestructura cerca del punto eutéctico que presenta el diagrama de fases ZrO_2-Pr_2O_3 para un 82.4% de óxido de praseodimio ($PrO_{1.5}$) y un 17.6% en ZrO_2, según la figura 2 (a).

Un material eutéctico es un sólido con una microestructura homogénea formada por un constituyente compuesto por dos o más fases. Solidifica según una reacción en la que el líquido se transforma isotérmicamente en dos fases sólidas de manera

simultánea. La temperatura a la que ocurre la transformación se denomina temperatura eutéctica y presenta un mínimo en el diagrama de fases, es decir es la menor temperatura a la que el sólido puede transformarse en líquido, siendo, por tanto, inferior a la temperatura de fusión de los componentes puros y de sus aleaciones. Para que esta reacción tenga lugar, el compuesto tiene que tener una composición determinada, denominada eutéctica. Fuera de ella se forma, además del constituyente, fase primaria, también llamada proeutéctica.

Cuando los compuestos de composición eutéctica solidifican direccionalmente, el proceso de extracción de calor desde el estado fundido da lugar a un avance del frente de solidificación en la dirección del flujo de calor. Este fenómeno conduce a un alineamiento y continuidad notables de las fases a lo largo del eje de crecimiento, generando así una microestructura altamente anisótropa.

Las microestructuras presentes en los eutécticos solidificados direccionalmente pueden ser agrupadas en cuatro categorías distintas. Cuando existe una cierta regularidad en la distribución de las fases, se denominan eutécticos regulares; en contraste, se les asigna la etiqueta de eutécticos irregulares en ausencia de tal periodicidad. Según la geometría de la distribución, se puede distinguir entre eutécticos laminares, compuestos por láminas alternadas de las dos fases, y eutécticos fibrilares, conformados por fibras de una fase inmersas en una matriz continua de la otra fase, con el aspecto mostrado en la figura 5.

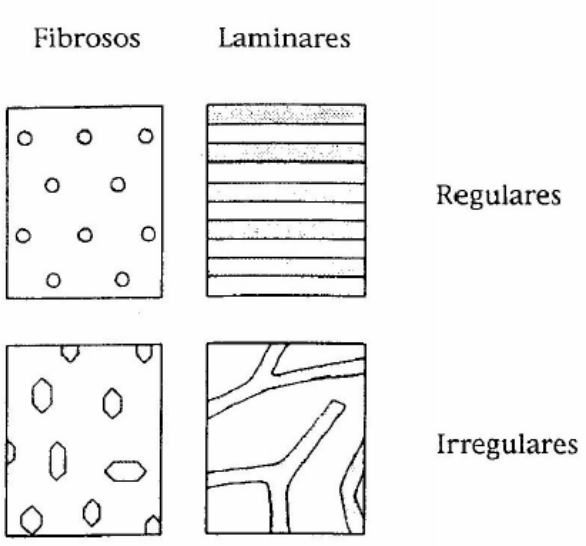

Figura 5. Tipos de eutécticos según su geometría.

Jackson y Hunt establecieron una ley que relaciona la velocidad de procesado (V) con el espaciado entre las fases (λ) en un eutéctico regular, tal y como se observa en la expresión 6:[27,28]

$$\lambda^2 V = k \qquad (6)$$

donde k es una constante que depende de magnitudes tales como el calor latente de fusión, los coeficientes de difusión, la energía superficial y otros parámetros, que se pueden deducir del diagrama de fases. Lo habitual es determinarla experimentalmente y su valor varía mucho al tratar sistemas diferentes.

En virtud de esta expresión la separación entre las fases podría controlarse variando la velocidad de crecimiento.

2.2. Objetivo 2: Fabricación mediante solidificación direccional asistida por Láser de materiales con porosidad controlada, con aplicaciones en salud y medio ambiente.

La fabricación mediante fusión por láser de materiales densos, combinada con la disolución controlada de óxido de magnesio, abre nuevas perspectivas en la creación

de estructuras porosas con aplicaciones interesantes en ámbitos como la salud y el medio ambiente.

Fabricación de membranas con permeación selectiva al CO_2.

En la actualidad, resulta urgente abordar la problemática derivada de las emisiones de dióxido de carbono (CO_2) para contrarrestar el calentamiento global. La quema de combustibles fósiles y otras actividades humanas ha generado un aumento sustancial del CO_2, el principal gas de efecto invernadero, contribuyendo significativamente al calentamiento global. En este sentido, se revela crucial la investigación en tecnologías de captura y almacenamiento de dióxido de carbono, destacando la necesidad de desarrollar y mejorar métodos efectivos para separar selectivamente y almacenar el CO_2 proveniente de reacciones químicas, gases de combustión y el aire.[29]

En la actualidad, la separación del dióxido de carbono se lleva a cabo a escala comercial mediante tecnologías de absorción o adsorción. Algunos ejemplos son la separación de dióxido de carbono en procesos de producción de hidrógeno,[30] así como la recuperación eficiente de CO_2,[31] para los que se emplean procesos de absorción de aminas que presentan notables penalizaciones energéticas.[32]

En este sentido, se está intentando sustituir los absorbentes líquidos por adsorbentes sólidos[33] como óxidos metálicos,[34,35] hidrocalcitas[36] y zeolitas,[37] así como la captura directa de dióxido de carbono del aire mediante el uso de adsorbentes de amina soportados en sólidos.[38,39]

La separación de dióxido de carbono a una escala mucho mayor en procesos continuos, eficientes, de bajo coste, sólidos y limpios, con penalizaciones energéticas mínimas

podría conseguirse mediante un proceso de membrana. En comparación con los procesos de absorción, los procesos de membrana no requieren variaciones de temperatura y/o presión, lo que reduce las penalizaciones energéticas y permite una operación continua. No obstante, las membranas deben poseer tanto una alta permeabilidad (transporte a través de la membrana) como una elevada selectividad (separación selectiva de un componente) para lograr una separación eficiente.

Idealmente, las membranas deberían separar selectivamente los componentes deseados de una mezcla, permitiendo un transporte rápido a través de ellas.

En la separación de gases a través de una membrana, la fuerza impulsora para el transporte proviene de la diferencia de presión parcial entre los lados de alimentación y permeado de la membrana ($p_f - p_p$), representados en la figura 6. Para que ocurra la transferencia de permeante desde el lado de alimentación al de permeado, es necesario que $p_f > p_p$.

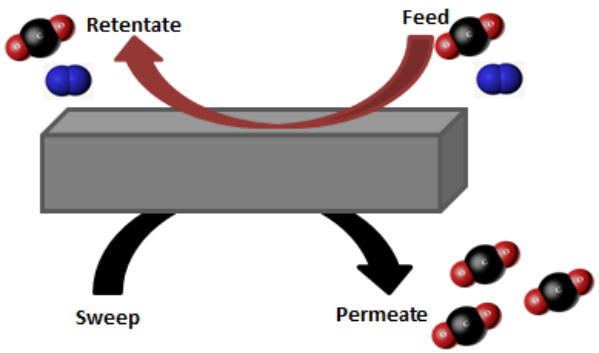

Figura 6. Representación gráfica de una membrana con separación selectiva de CO_2 de una mezcla de gases. Extraída de G. A. Mutch, et al [42]

Atendiendo a esta estrategia, una manera de aumentar la permeabilidad sin comprometer la selectividad es utilizando membranas de transporte facilitado, en las que el transporte del permeante está mediado por portadores. Los portadores pueden incorporarse en membranas porosas mediante la adición de grupos funcionales con alta afinidad por el permeante o, en membranas de líquidos soportados, a través del uso de líquidos con una reactividad adecuada hacia el permeante.

Este último enfoque teóricamente podría ofrecer una alta permeabilidad y selectividad infinita; la membrana puede considerarse "pseudo-densa", con el líquido "cerrando" los caminos de menor resistencia, al mismo tiempo que ofrece un camino selectivo con alta difusividad.

En este sentido y en el caso de permeación selectiva al CO_2, se han diseñado las membranas duales o membranas de sales fundidas, que se basan en la combinación de un sólido inorgánico poroso (la matriz o soporte) y una mezcla de carbonatos fundidos infiltrados dentro del espacio poroso, como agente portador. Empleando carbonatos fundidos se conseguiría, teóricamente, una selectividad infinita para el dióxido de carbono. Por otro lado, la combinación de una fase sólida con una fase líquida evitaría problemas derivados de la expansión térmica. En la mayoría de los casos, la sal de carbonato fundido utilizada para las membranas de sal fundida es la mezcla ternaria eutéctica de Li_2CO_3, Na_2CO_3 y K_2CO_3 en proporciones molares de 43.5%, 31.5% y 25%, respectivamente. Esta combinación es la que presenta menor punto de fusión (~400 °C), aunque también se han realizado investigaciones con Li_2CO_3 puro y mezclas binarias.

Las dos características principales del soporte que determinan la permeabilidad de la membrana son sus propiedades conductoras y su microestructura.

Aunque puede haber permeación en membranas fabricadas con un soporte hecho de un material aislante, como la alúmina, la característica fundamental de las membranas duales consiste en el uso de soportes conductores, sea con conducción electrónica, iónica o mixta, de tal manera que la conducción en el soporte participa en el mecanismo de permeación. En ese caso se produce un doble mecanismo de transporte acoplado (de ahí el término dual) entre los iones CO^{3-}, a través de los carbonatos fundidos, y los portadores iónicos o electrónicos a través del soporte. Las reacciones que tienen lugar en ambos lados de las membranas dependen del tipo de conducción del soporte:

Si el soporte es un conductor puramente electrónico (figura 7 (b)) se requiere la presencia de oxígeno en el gas de alimentación para formar el ion carbonato, produciéndose la reacción 7.

$$CO_2\,(g) + 1/2O_2\,(g) + 2e^-\,(s) \rightleftarrows CO_3^{2-} \qquad (7)$$

Si el soporte es un conductor puramente iónico (figura 7 (a)), con iones de oxígeno como portadores, el carbonato se forma a partir de los iones aportados por el soporte, produciéndose la reacción 8.

$$CO_2\,(g) + O^{2-}\,(s) \rightleftarrows CO_3^{2-} \qquad (8)$$

Finalmente, para un conductor mixto ambas reacciones pueden tener lugar, dependiendo de la existencia o no de oxígeno en el gas de alimentación.

Si bien inicialmente se usaron soportes basados en metales, (acero principalmente) las reacciones entre los carbonatos y el metal en las intercaras internas a temperaturas mayores de 650°C limitan la estabilidad a largo plazo. Además, la falta de conductividad de ion oxígeno exige la presencia de oxígeno en el gas de alimentación para formar iones de carbonato y transportarlos a través de la sal fundida. Por todo ello, en la actualidad se investiga casi exclusivamente en soportes basados en óxidos conductores iónicos o mixtos.

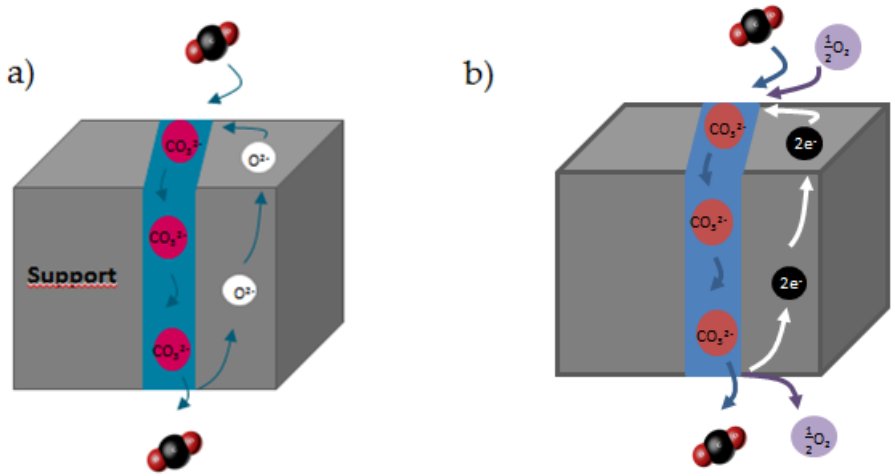

Figura 7. Mecanismos de transporte de CO_2 propuestos para membranas de carbonato fundido soportadas utilizando (a) un soporte que conduce iones de oxígeno y (b) un soporte conductor electrónico. Modificada de G. A. Mutch, et al [42]

De entre los materiales conductores de iones oxígeno, los más estudiados como soportes para membranas de sales fundidas son los óxidos con estructura tipo fluorita, como la ceria dopada con Sm (SDC) o Gd (GDC) y la circona estabilizada con ytria (YSZ), debido a su alta conductividad iónica.

En el caso de los soportes con conductividad mixta electrónica y iónica (CEIM) ya no se requiere oxígeno en la corriente de gas de alimentación, aunque la presencia de este gas puede ser conveniente en algunos casos.

La mayoría de los materiales CEIM utilizados como soportes para sales fundidas son estructuras tipo perovskita, como (La, Sr)(Co, Fe)$O_{3-\delta}$ (LSCF). Este material exhibe una alta conductividad iónica y electrónica mixta a temperaturas superiores a 700 °C; la conductividad electrónica es de ~10^2 S cm^{-1} y la conductividad de oxígeno de ~10^{-1} S cm^{-1}.

Otros ejemplos de conductores mixtos empleados en membranas duales son $La_{0.85}Ce_{0.1}Ga_{0.3}Fe_{0.65}Al_{0.05}O_{3-\delta}$ (LCGFA) y $SrFe_{0.8}Nb_{0.2}O_{3-\delta}$[40] que también mostraron una buena estabilidad química a largo plazo, así como estabilidad térmica cíclica bajo atmósferas ricas en dióxido de carbono.

El segundo factor que influye en la permeabilidad son los aspectos relativos a la microestructura de la membrana, tales como el porcentaje de porosidad, así como la conectividad y el alineamiento de la misma.

De acuerdo con el mecanismo convencional de transporte de CO_2 en una membrana dual con soporte conductor iónico de oxígeno, el flujo de CO_2 (J) a través de la membrana (volumen o número de moles del permeante transportado por unidad de área de membrana y por unidad de tiempo), viene dado por la expresión 9:

$$J = \frac{RT}{4LF^2}\sigma_{eff}\ln\left(\frac{p_{CO_2(p)}}{p_{CO_2(f)}}\right) \qquad (9)$$

Donde L es el espesor de la membrana, F es la constante de Faraday, p_{CO_2}(feed) y p_{CO_2}(permeate) son las presiones parciales de CO_2 en los lados de alimentación y permeado, respectivamente, y σ_{eff} es la conductividad ambipolar efectiva que resulta del transporte simultáneo pero separado de especies iónicas en las fases de carbonato fundido y óxido sólido. Suponiendo un número de transporte electrónico despreciable en el soporte, la conductividad ambipolar efectiva se expresa mediante la expresión 10:

$$\sigma_{\text{eff}} = \frac{\left[\left(\frac{\Phi}{\tau}\right)_C \sigma_C\right]\left[\left(\frac{\Phi}{\tau}\right)_{SO} \sigma_{SO}\right]}{\left[\left(\frac{\Phi}{\tau}\right)_C \sigma_C\right] + \left[\left(\frac{\Phi}{\tau}\right)_{SO} \sigma_{SO}\right]} \qquad (10)$$

Donde σc, (φ/τ)c y σso, (φ/τ)so son la conductividad y la relación de fracción de volumen a factor de tortuosidad de las fases de carbonato y óxido sólido, respectivamente.[41] En el caso de un llenado completo de los poros por carbonatos, φc es igual a la porosidad del soporte, comúnmente representada por ε.

Según las ecuaciones anteriores, el rendimiento de la membrana depende de propiedades intensivas del material, como las conductividades de carbonato fundido y óxido sólido, así como de características geométricas y microestructurales, siendo estas últimas influenciadas por el método de preparación del soporte.

A partir del flujo (J) dado por la expresión 9 se pueden definir la permeabilidad y la permeancia mediante las expresiones 11 y 12, respectivamente. La permeabilidad la podemos definir como el flujo normalizado por el grosor de la membrana (L) y la fuerza impulsora (11), mientras que la permeancia se normaliza únicamente por la fuerza impulsora (12).

$$Permeabilidad\ (P) = J\frac{L}{p_f - p_p} \qquad (11)$$

$$Permeancia\ (p) = \frac{J}{p_f - p_p} \qquad (12)$$

En la siguiente figura (figura 8) extraída de G. A. Mutch, et al.[42] se muestran algunos de los valores de permeancia de CO_2 reportados para membranas de carbonatos fundidos.

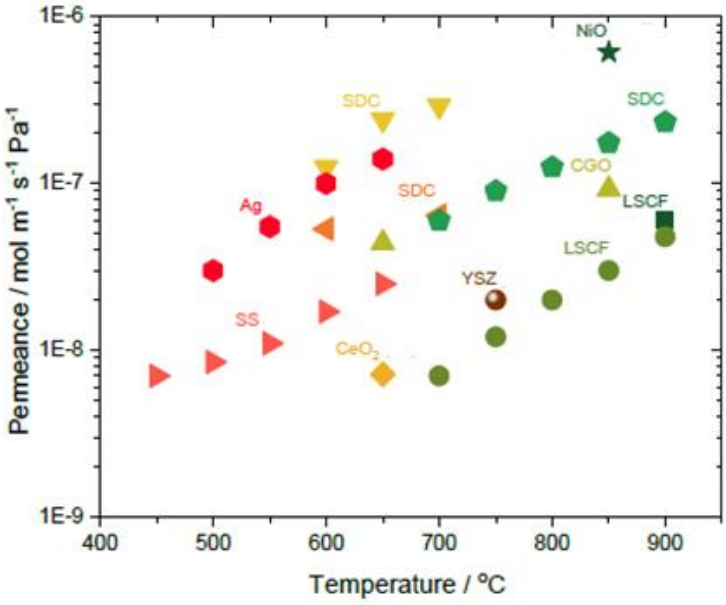

Figura 8. Ejemplos de permeancia de dióxido de carbono en función de la temperatura para membranas duales de carbonato fundido. Extraída de G. A. Mutch, et al [42]

En esta figura podemos observar que los mejores resultados de permeancia, en membranas similares a la producida en esta parte de la tesis, son aquellos obtenidos para soportes de ceria dopada con samario (SDC) y ceria dopada con gadolinio (CGD). Para la fabricación de una membrana de sal fundida se busca un soporte delgado (o, más específicamente, un grosor de membrana activa pequeño) con alta porosidad y con baja tortuosidad. En algunos estudios[43, 44] se reporta que la permeancia de CO_2 a través de membranas de este tipo aumenta cuando el grosor de la misma es menor. La estructura porosa de los soportes, que abarca aspectos como el volumen de poros, su

tamaño, la conectividad entre poros y la tortuosidad, también ejerce una influencia significativa en la permeación del dióxido de carbono. Asimismo, la porosidad en las superficies externas del soporte define el área interfacial líquido-gas y las longitudes de la frontera de triple fase en los lados de alimentación y permeado de la membrana.

En esta parte del trabajo se pretende fabricar una membrana de carbonatos fundidos empleando como matriz un conductor de O^{2-} obtenido a partir de un eutéctico fibrilar. Un punto crucial para lograr una buena funcionalidad de la membrana es la elección del material que conforma el soporte. Este debe presentar unas propiedades adecuadas tanto desde el punto de vista intrínseco (conducción iónica, por ejemplo) como microestructural, ya que hemos visto que el flujo de permeación depende de ambos tipos de propiedades.

Las características deseables de un soporte de membrana imponen condiciones restrictivas en la selección de materiales para la solidificación direccional:

- En primer lugar, el crecimiento eutéctico fibrilar requiere que la proporción de la fase minoritaria no supere aproximadamente el 29% en volumen.[45] De lo contrario, en general, se observará crecimiento laminar.
- En segundo lugar, debe producirse un crecimiento acoplado para lograr una microestructura fibrilar ordenada y libre de colonias.
- En tercer lugar, la fase minoritaria (fibras) debe ser fácilmente atacada químicamente sin afectar a la matriz, que se convertirá en el soporte de la membrana, y dicha matriz debe ser un conductor de iones de oxígeno con buena conductividad.

- Por último, se requiere compatibilidad en la expansión térmica entre los materiales que forman la matriz y las fibras, para evitar, por ejemplo, la formación de grietas durante la solidificación.

Después de explorar diferentes sistemas, encontramos que el sistema ZrO_2–MgO es una combinación adecuada de óxidos, ya que cumple con los requisitos mencionados anteriormente. Según el diagrama de fases (PD) ZrO_2–MgO (figura 9),[46] existe un punto eutéctico alrededor del 55.07% mol de MgO[47] con Te ≈ 2108 °C.

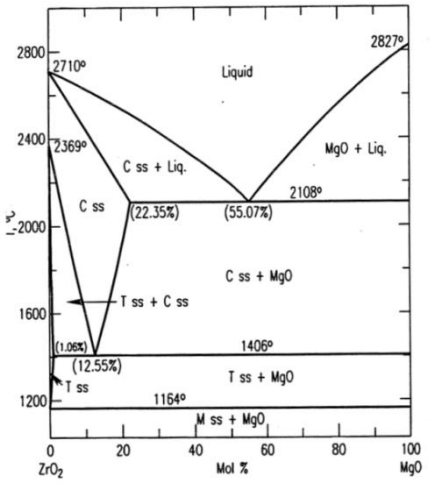

Figura 9. Diagrama de fases del sistema ZrO_2-MgO.

Tras la solidificación, las fibras de MgO, con diámetro de entre 1 y 2 μm para velocidades de procesado de 10 a 25 mm/h, están embebidas en una fase cúbica de circona estabilizada con magnesio (MgSZ) con ~20% de contenido de Mg^{2+}.[48] La incorporación de iones Mg^{2+} dentro de la fase inicialmente monoclínica de ZrO_2 introduce un número correspondiente de vacantes de oxígeno que estabilizan la MgSZ en su forma cúbica y proporcionan un comportamiento de conducción iónica. La proporción de volumen de las fibras de MgO en el eutéctico predicha por el DF es del

28.7%, cerca del límite entre el crecimiento fibrilar y laminar. Los coeficientes de expansión térmica lineal (CET) de MgO y MgSZ son próximos: el CET de MgO varía de 11 a 14 x 10^{-6} K^{-1} entre 300 y 1000K,[49] que está cerca del CET de materiales relacionados con la circona cúbica, como por ejemplo la circona dopada con 8 mol% de Y_2O_3 (8-YSZ), con un CET de 10,5/11 x10^{-6} K^{-1} en el mismo rango de temperatura.[50] El eutéctico MgO-MgSZ solidificado direccionalmente también muestra una resistencia mecánica adecuada, con valores de módulo de rotura que van desde 150 hasta 450 MPa.[51, 52] Esto sugiere la posibilidad de producir bicristales sin grietas de manera segura durante el enfriamiento después de la solidificación asistida por láser.

Además, aunque inferior a la de 8-YSZ ($\sigma \gtrsim 10^{-2}$ S cm^{-1} a 1020 K),[53] la MgSZ aún presenta una buena conductividad iónica de 2.3 x 10^{-3} S cm^{-1} a 1000 K.[54] Finalmente, el MgO es altamente soluble en ácido clorhídrico, mientras que la MgSZ no lo es, de modo que las fibras pueden eliminarse mediante ataque ácido sin afectar significativamente a la matriz.

Por todo lo anterior, se consideró que el sistema elegido era una buena opción para el diseño de membranas basadas en carbonatos fundidos para la filtración selectiva del CO_2 de una mezcla de gases.

El esquema del procedimiento a seguir para la fabricación de estos dispositivos se resume en la figura 10 y consiste en la síntesis de un material eutéctico fibrilar en el que tenemos fibras de MgO dispuestas en una matriz de circona estabilizada con magnesio; tras un ataque ácido las fibras de MgO desaparecen y queda la matriz de MgSZ con canales en ella. Dichos canales son infiltrados con carbonatos fundidos que son los

encargados de llevar a cabo la permeación selectiva del CO_2. Una vez infiltrado el soporte, la membrana se prepara para la medida de permeación siguiendo el procedimiento descrito en el apartado 3.14 del presente documento.

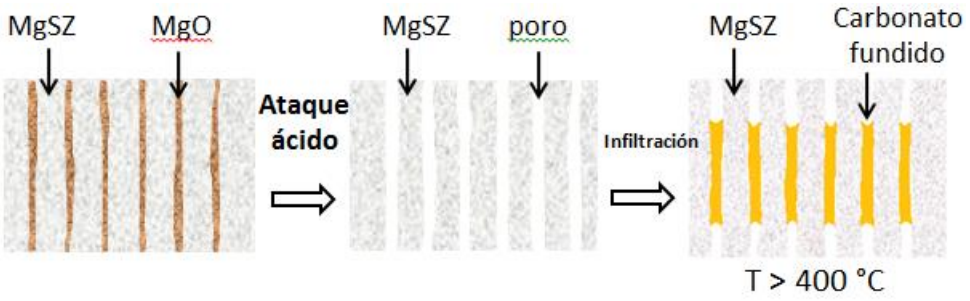

Figura 10. Representación esquemática de la fabricación de las membranas duales de este trabajo.

Fabricación de implantes óseos porosos.

La fabricación de implantes óseos es esencial para abordar diversas condiciones médicas, como fracturas, lesiones o enfermedades óseas degenerativas. Estos implantes son fundamentales para restaurar la integridad estructural y funcional del tejido óseo, facilitando la recuperación y mejora de la calidad de vida de los pacientes. Los avances en este campo buscan desarrollar materiales biomiméticos y técnicas innovadoras para mejorar la integración, la resistencia y la biocompatibilidad de estos implantes, impulsando así la eficacia de los tratamientos ortopédicos.

Algunas características esenciales que deben incluir los materiales empleados en regeneración ósea son las siguientes:

1. **Porosidad controlada**: La porosidad es crucial para permitir la infiltración celular, vascularización y la deposición de minerales. Los poros deben estar distribuidos de manera uniforme para facilitar la difusión de nutrientes y la eliminación de desechos.

2. **Biocompatibilidad**: El *scaffold* debe ser compatible con el entorno biológico circundante, evitando respuestas inmunológicas adversas. La interacción armoniosa entre el *scaffold* y las células del tejido circundante es esencial para la integración exitosa.
3. **Degradación controlada**: Un *scaffold* eficaz debe ser bioabsorbible, permitiendo una degradación gradual que coincida con el ritmo de la formación del nuevo tejido. Este proceso controlado evita la necesidad de intervenciones quirúrgicas adicionales para retirar el implante.
4. **Propiedades mecánicas adecuadas**: El *scaffold* debe proporcionar un soporte mecánico suficiente durante el período crítico de curación y regeneración, evitando fracturas o colapsos prematuros.
5. **Estímulo para la regeneración ósea**: La superficie del *scaffold* debe ser propicia para la adhesión y proliferación celular, así como para la formación de tejido óseo. Materiales con propiedades osteoinductivas y osteoconductivas son altamente deseables.

Los materiales más estudiados para la regeneración de tejidos duros han sido biocerámicas basadas en silicatos, ya que muchas de ellas tienen la capacidad de generar una capa de hidroxiapatita (HAp) en contacto con un fluido corporal simulado (SBF), estimulando así la proliferación y adhesión de células osteoblásticas.

También se han estudiado sistemas multifásicos eutécticos como $Ca_3(PO_4)_2$–$CaSiO_3$,[55-57] $Ca_3(PO_4)_2$–$CaMg(SiO_3)_2$,[58] $CaSiO_3$–$CaMg(SiO_3)_2$[59] y $Ca_3(PO_4)_2$–$CaSiO_3$–$CaMg(SiO_3)_2$.[60]

Las desventajas principales de cerámicas, vidrios, *bioglasses* y cristales bioactivos radican en su fragilidad en forma porosa y en la limitada bioactividad de sus

superficies cuando son completamente densos.[61, 62] Una estrategia para abordar estas dificultades consiste en la concepción de cerámicas bioactivas con la capacidad de desarrollar una estructura porosa in situ tras su implantación. Para lograr esto, es esencial que los materiales estén compuestos por al menos dos fases, una de naturaleza bioactiva y otra reabsorbible. La elección adecuada de las fases permite ajustar propiedades mecánicas, bioactividad, liberación de iones y tasa de absorción según las necesidades específicas del tejido óseo.

Estos biomateriales ofrecen un andamiaje tridimensional que no solo brinda un soporte estructural robusto, sino que también proporciona un respaldo mecánico esencial para el óptimo funcionamiento celular.

La elección del material para estas matrices debe considerar aspectos como la no toxicidad, biocompatibilidad, osteoproducción, osteoconducción, bioabsorbibilidad y propiedades mecánicas adecuadas para respaldar el crecimiento y remodelación ósea.[63-65]

En esta parte del trabajo se pretende llevar a cabo la fabricación de un implante cerámico que sea capaz de generar porosidad in situ a la vez que favorecer la formación de nuevo hueso en tejidos dañados. Para ello se pretende elaborar muestras cerámicas multifásicas que, mediante la disolución de MgO en contacto con sistemas biológicos, den lugar a *scaffolds* porosos combinando los beneficios mecánicos de una estructura densa con los requerimientos de porosidad en la regeneración ósea.

Se eligió el óxido de magnesio como fase reabsorbible debido al papel de los iones Mg^{2+} en la remodelación ósea, el desarrollo esquelético, el metabolismo humano y procesos celulares como la adhesión de células óseas y la proliferación de osteoblastos.[66,67]

3. Materiales y métodos

En el contexto de la presente investigación, se ha llevado a cabo un proceso de preparación y caracterización de materiales con el propósito de abordar los dos objetivos anteriormente definidos que, aunque cada uno enfocado en aplicaciones distintas, comparten algunas técnicas de preparación y caracterización.

3.1. Conformado de los precursores cerámicos

El prensado isostático se emplea con el propósito de compactar materiales pulverulentos para conferirles una configuración final que puede ser esférica, tubular, cilíndrica o anular, entre otras. En este método específico de prensado, el material en polvo se introduce en una matriz de moldeo que presenta una baja resistencia a la deformación, como gomas o elastómeros. Mediante la aplicación de presión sobre un fluido a temperatura ambiente, dicha presión se distribuye de manera uniforme a lo largo de toda la superficie del molde, y, en consecuencia, se transmite de manera uniforme al material en polvo que se pretende compactar, tal y como esquematizamos en la figura 11.

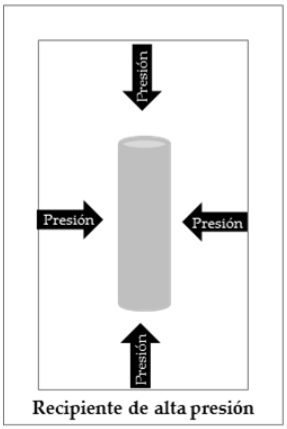

Figura 11. Representación esquemática de la técnica de prensado isostático en frío.

Para llevar a cabo la compactación isostática se emplea una prensa de fabricación propia (figura 12), disponible en el área de Ciencia de Materiales e Ingeniería Metalúrgica, y se sigue el siguiente procedimiento: En primer lugar, se colocan unos gramos de la mezcla en un mortero de ágata y se añaden dos gotas del aglutinante polyvinilalcohol (PVA). Tras homogeneizar los polvos durante unos minutos se comienza a verter el material en tubos cilíndricos de látex, con ayuda de un embudo. Es de vital importancia mantener la muestra en vertical, para lo que se emplea un casquillo metálico, el cual se coloca alrededor del tubo de látex, impidiendo que se doble. Para evitar que el material se salga del recipiente se emplean unos alambres metálicos, que sujetan el tubo cilíndrico al mismo. Todo este sistema se introduce en un recipiente plástico y éste en la vasija de una prensa isostática, donde se somete al material a una presión de 200 MPa al aplicar una fuerza de 10 Ton. Tras esperar un tiempo de dos minutos se retira la presión lentamente. Una vez retirada la presión, se extrae de nuevo el conjunto metálico y se procede a la retirada de los alambres y el tubo en el que estas iban colocadas.

Figura 12. Prensa para compactación isostática.

Para el desarrollo del primer objetivo de la tesis se ha llevado a cabo la preparación de óxidos mixtos de ZrO_2 y PrO_x con las siguientes composiciones nominales: $Pr_{1.70}Zr_{2.30}O_{7+x}$ (P1.70ZO), $Pr_2Zr_2O_{7+x}$ (PZO), $Pr_{2.24}Zr_{1.76}O_{7+x}$ (P2.24ZO), $Pr_{2.4}Zr_{1.6}O_{7+x}$ (P2.4ZO), $Pr_3Zr_1O_{7+x}$ (P3ZO) y $Pr_{1-x}Zr_xO_{2-y}$ con x≈0,175.

A partir de la mezcla en polvo con las cantidades de Pr_6O_{11} y ZrO_2 correspondientes a cada composición, se procede a la obtención de precursores cerámicos mediante la compactación isostática. El diámetro obtenido del compacto cerámico es de aproximadamente 2 mm y unos 60 mm de longitud.

Para la obtención de las muestras del segundo objetivo de la tesis se mezclaron polvos comerciales de ZrO_2 (Aldrich, 99%) y MgO (Alfa Aesar, 99.99%) en las proporciones adecuadas para obtener una mezcla con la composición eutéctica del sistema ZrO_2-MgO. Dicha mezcla se conformó en forma cilíndrica mediante compactación isostática en frío, siguiendo el procedimiento comentado anteriormente, a 200 MPa durante 3 minutos.

Para la fabricación del implante óseo se utilizó un 14% en peso de SiO_2 (pureza: 99.8%, Alfa Aesar, Haverhill, Massachusetts, Estados Unidos), un 18.7% de silicato de calcio (pureza > 99%, Merck, Darmstadt, Alemania), un 36.6% de MgO (pureza > 99%, Merck, Darmstadt, Alemania) y un 30.7% de $Ca_3(PO_4)_2$ (Carlo Erba, Barcelona, España).

3.2. Sinterización

Una vez llevado a cabo el conformado, se someten las muestras a un proceso de sinterización, que pretende aumentar la resistencia mecánica de las muestras al

disminuir la porosidad presente en ellas, con el objetivo de hacerlas más manejables para tratamientos posteriores.

La sinterización de las muestras orientadas al cumplimiento del objetivo 1 y de las muestras generadas para su futura transformación en un implante poroso se llevó a cabo en un horno marca Hobersal 1600°C y tiene lugar en tres etapas:

1. Rampa de calentamiento: en esta etapa la temperatura sube desde temperatura ambiente hasta 1500 °C a una velocidad de 5°C/min para las muestras del sistema PrO_x-ZrO_2 y hasta 1300 °C a la misma velocidad para el caso de las muestras con aplicación biomédica.

2. Mantenimiento de la temperatura a 1500 °C o 1300 °C durante 12h, según corresponda.

3. Disminución de la temperatura desde el punto más alto hasta temperatura ambiente con una velocidad igual a la de calentamiento.

Las muestras orientadas a la fabricación de la membrana con permeación selectiva, tras su conformado por compactación isostática, se sinterizaron a 1500 °C durante 12 horas en un horno abierto. Las barras resultantes tienen aproximadamente 80 mm de longitud.

3.3. Fusión Zonal con láser

Tras la obtención de las barras sinterizadas, la siguiente etapa es la solidificación direccional o fusión zonal por láser. Esta técnica se basa en la focalización de un haz láser sobre el extremo de un precursor hasta inducir la formación de una gota de

material en estado fundido, seguida de la inserción de una semilla cristalina en la misma. El cilindro precursor es desplazado con ayuda de unos ejes, que permiten tanto el desplazamiento longitudinal como la rotación, hacia la región de material fundido. Simultáneamente se extrae el material ya solidificado dando lugar a un cilindro solidificado direccionalmente.

El diseño de la instalación permite focalizar el haz láser produciendo un calentamiento localizado con gradientes térmicos muy pronunciados entre el fundido y el sólido. La figura 13 recoge de forma gráfica la información anteriormente explicada: en la figura 13 (a) se representa de forma esquemática el proceso de solidificación direccional, mientras que la figura 13 (b) muestra la instalación experimental:

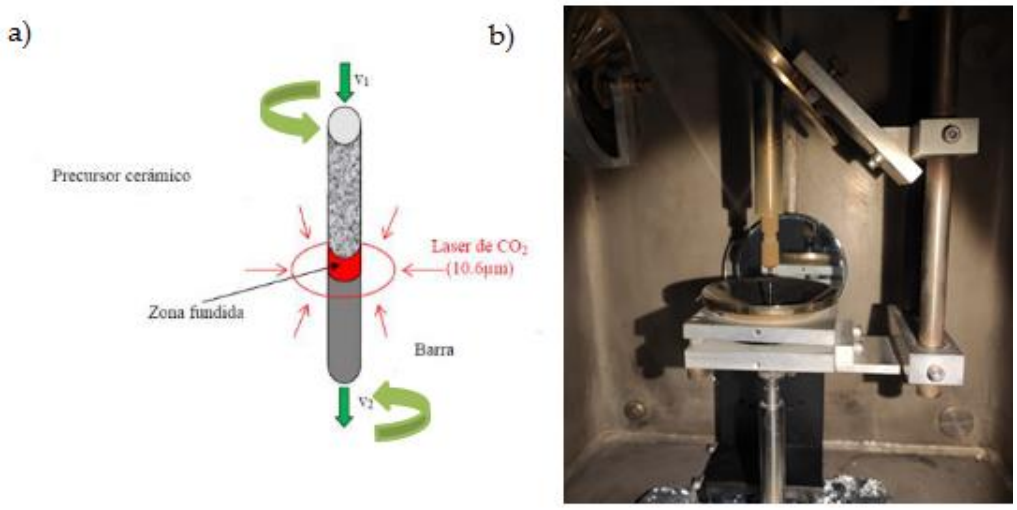

Figura 13. Representación esquemática (a) y diseño real (b) de la instalación de fusión zonal láser.

En situaciones específicas, puede resultar beneficioso realizar el crecimiento cristalino en una atmósfera controlada. Para este propósito, se puede incorporar al equipo una cámara con ventanas selladas que permite controlar la atmósfera de trabajo.

Es importante destacar que los ejes en los cuales se fijan los cilindros poseen la capacidad de movimientos tanto de rotación como de traslación. La aplicación de un movimiento de rotación es especialmente útil cuando el material que se pretende fundir exhibe una baja conductividad térmica, ya que la rotación facilita una homogeneización más rápida de la temperatura en toda la sección del cilindro.

En este trabajo, para llevar a cabo la fusión zonal se ha empleado un láser de CO_2 (Blade- 600, Electronic Engineering) de onda continua. La longitud de onda de emisión de dicho láser es de 10.6 μm y la potencia máxima que puede llegar a alcanzar es de 600 W.

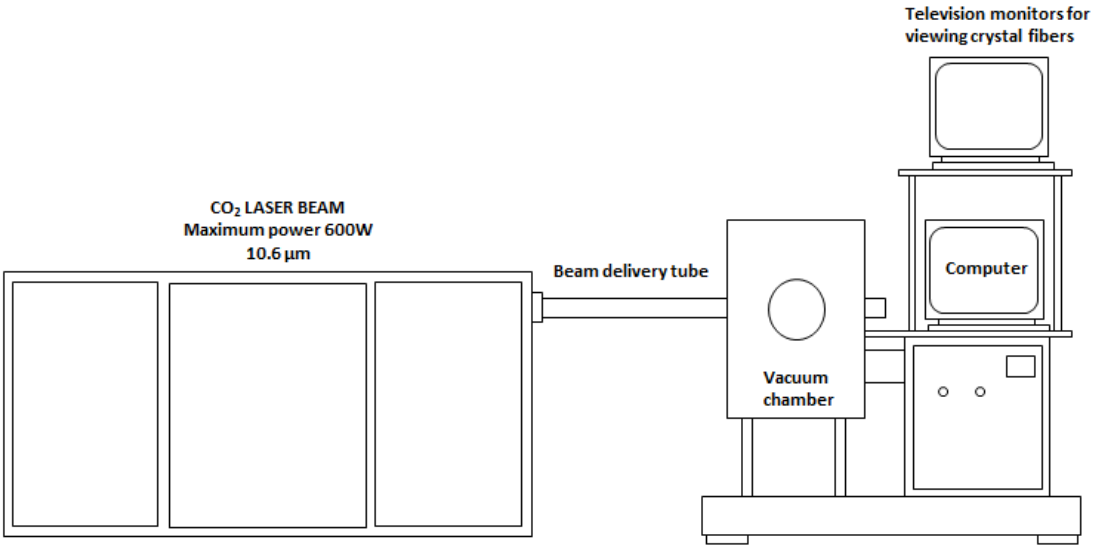

Figura 14. Representación esquemática de la configuración del equipo de fusión zonal por láser.

La configuración del equipo empleado es tal y como se esquematiza en la figura 14.

Mediante esta técnica se pueden alcanzar temperaturas superiores a 2700 ºC, suficientes para producir la fusión de los materiales cerámicos que se estudian. La potencia con la que se trabajó para la fusión del material fue de alrededor de 150 W.

En el presente trabajo, las muestras procesadas por láser se obtuvieron en un proceso de tres etapas. Las dos primeras etapas consisten en un proceso de densificación donde se elimina la porosidad que todavía posee el precursor sinterizado y conlleva el adelgazamiento de la muestra, lo que favorece la difusión de calor y gases en el interior, así como el mejor alineamiento de la muestra, lo que favorece el crecimiento posterior. La última etapa es la etapa de crecimiento, donde el material cerámico vuelve a fundir y solidifica con una microestructura controlada. Las velocidades de la etapa de crecimiento empleadas en el desarrollo del objetivo 1 han sido 25, 100 y 300 mm/h y las atmósferas de crecimiento O_2, aire, N_2 y una mezcla de Argón con un 5% de H_2. En este punto hay que tener en cuenta que para las atmósferas de O_2, N_2 y Ar+5%H_2 se ha trabajado con una ligera sobrepresión con respecto a la presión atmosférica y para la atmósfera de aire se ha trabajado a presión atmosférica.

Para el objetivo 2.1 se ha trabajado a una velocidad crecimiento de 25 mm/h, en todos los casos en aire a presión atmosférica. Una vez procesadas, las barras tenían una longitud de aproximadamente 80 mm y un diámetro de entre 1.2 y 1.5 mm.

Durante la fabricación de las muestras orientadas al logro del objetivo 2.2 se ha llevado a cabo una primera densificación láser de las muestras a una velocidad de 250 mm/h con el objetivo de eliminar parte de la porosidad de la muestra y posteriormente se ha llevado a cabo el crecimiento de las muestras en aire a velocidades de 50, 100 y 300 mm/h, empleando una contrarrotación a 50 rpm. Las muestras obtenidas presentaban una longitud de aproximadamente 50 mm y un diámetro entre 2 y 2.5 mm.

Ventajas y desventajas de la fusión zonal láser.

A continuación, se presentan las principales ventajas y desventajas de la fusión zonal láser:

Ventajas de la Fusión Zonal Láser:

1. **Precisión en el Calentamiento:** La fusión zonal láser permite un calentamiento altamente focalizado.
2. **Alta Temperatura Alcanzable:** superiores a 2000 °C
3. **Control del Entorno:** La posibilidad de emplear atmósferas controladas, oxidantes o reductoras, para obtener materiales con propiedades específicas.
4. **Observación Directa**, lo que facilita la detección de defectos macroscópicos, transiciones de fase y estudios de transporte de masa en la zona líquida.
5. **Las altas velocidades de crecimiento**, debido a los elevados gradientes térmicos y la baja cantidad de material requerida, para disponer de muestras que puedan ser caracterizadas.

Desventajas de la Fusión Zonal Láser:

1. **Limitación de Producción:** solo permite el crecimiento de una barra a la vez, lo que dificulta su aplicación a nivel industrial.
2. **Riesgo de Agrietamiento:** Los elevados gradientes de temperatura generados pueden causar el agrietamiento de algunos materiales.
3. **Evaporación de Componentes Volátiles:** La estrecha focalización del haz láser puede provocar una elevada evaporación de componentes volátiles durante el crecimiento, lo que puede modificar la composición del material resultante.

Este es uno de los inconvenientes que hemos tenido que enfrentar en nuestro trabajo. Durante la fabricación de las muestras destinadas al objetivo 1, la evaporación de óxidos de praseodimio durante el procesado láser hacía imposible conocer con exactitud la composición de la muestra que iba a resultar tras el procesado.

3.4. Ataque ácido

Para la fabricación de los soportes de membranas porosos a partir de eutécticos fibrilares, tras el procesado láser cada varilla se cortó en secciones de aproximadamente 2 mm de longitud. Con el fin de eliminar las fibras de MgO, dichas secciones se atacaron con ácido, mediante inmersión en una solución de HCl 1 M en agua destilada a 60 °C, tal y como representamos en la figura 15.

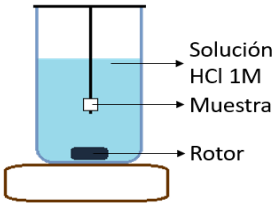

Figura 15. Representación del procedimiento empleado para el vaciado de las muestras en HCl (1M) a 60°C.

Para verificar el grado de ataque se midió la pérdida de peso, usando como valor de referencia la proporción en peso de las fibras de MgO en el eutéctico MgSZ-MgO (21%). Se observó que alcanzar pérdidas de masa superiores al 80% de la fase de MgO requería tratamientos de ≥20 días. Para aumentar el grado de ataque por parte del HCl a las fibras de MgO, cada 2-3 días se procedía a la limpieza de las muestras por ultrasonidos. Para ello se sacaban las muestras que estaban siendo atacadas por HCl y

se pasaban a un vaso con agua destilada que se colocaba en el interior de un baño de ultrasonidos. El proceso se refleja en la figura 16.

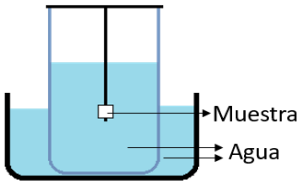

Figura 16. Representación del procedimiento empleado para el lavado de las muestras en agua destilada, en un baño de ultrasonidos.

Para aumentar la superficie efectiva de la membrana, se insertaron siete secciones porosas de MgSZ en orificios circulares (de aproximadamente 1.6 mm de diámetro) previamente perforados con láser en una placa cerámica de YSZ de espesor igual a 500 μm. La perforación de las láminas de YSZ fue llevada a cabo por la Dra. Ruth Lahoz, del INMA. Se utilizó Ceramabond 885 para asegurar las secciones dentro de la placa, tal y como se indica en la figura 17 (a), con el programa de temperatura de la figura 17 (b).

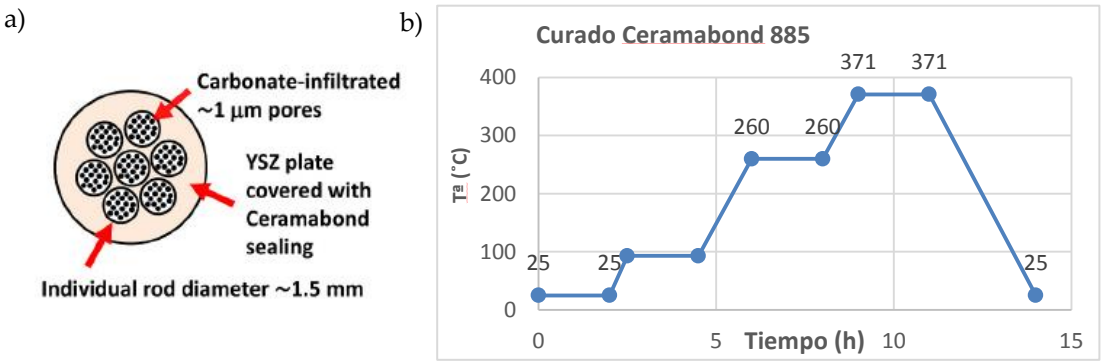

Figura 17. En la figura (a) se observa el montaje de las secciones circulares en la placa de YSZ, mientras que en la figura (b) mostramos el programa de temperatura empleado para sellar dichas secciones a la placa.

Para llevar a cabo por estudios de permeabilidad posteriores, es necesario montar la membrana fabricada sobre el tubo de circona que como veremos se insertará en el equipo de medida de permeabilidad. Para ello hacemos uso de Ceramabond 885 y procedemos a su curado del mismo modo que en el caso anterior.

3.5. Estudios de biodegradabilidad.

Para investigar la biodegradabilidad de las barras solidificadas direccionalmente, se procedió a su seccionamiento en forma de discos de unos 2 mm de grosor. Tras ser sometidas a un lavado con acetona, se sumergieron en un fluido corporal simulado (SBF), conforme a la metodología propuesta por Kokubo et al.,[68, 69] contenido en envases de polietileno mantenidos a una temperatura de 37 °C bajo condiciones estáticas. El pH inicial del SBF se ajustó en el rango de 7.2 a 7.4, correspondiente al pH normal del plasma humano. Transcurridas 4 semanas, se extrajeron los discos y se procedió al secado al aire a temperatura ambiente.

3.6. Microscopía electrónica de barrido (SEM)

El análisis composicional y morfológico de todas las muestras se llevó a cabo mediante Microscopía electrónica de barrido de emisión de campo (FESEM) haciendo uso de un microscopio Carl Zeiss MERLIN (figura 18) con un detector de dispersión de energía de rayos X (EDX) incorporado.

Figura 18. Microscopio Carl Zeiss MERLIN empleado para estudiar la microestructura de las muestras de este trabajo

El equipo consta de un cañón de emisión de electrones por emisión de campo de punta caliente y permite observaciones de hasta 0.8 nm de resolución espacial, empleando voltajes de aceleración entre 0.02 y 30 kV. Dispone de detectores de electrones secundarios y retrodispersados en la cámara y en la columna (in-lens), un detector de rayos X para análisis de la energía de los rayos X dispersados X-Max (20mm2) con SDD (Silicon Drift Detector) de Oxford Instruments y un detector HKL EBSD (Electron Back Scatter Diffraction), Nordlys II, para el registro y análisis de diagramas de difracción de electrones retrodispersados y mapas de orientación cristalográfica, que se procesan con los programas CHANNEL5 o AZtec. El equipo dispone también de un modo "Ojo de pez", que permite tener una imagen en el interior de la cámara. Los softwares de procesamiento de datos empleados han sido AZtec e INCA.

La obtención de imágenes mediante microscopía electrónica de barrido se basa en la focalización de un haz de electrones sobre la muestra utilizando lentes

electromagnéticas. Este haz de electrones se desplaza por la muestra, y diversos detectores, que pueden captar electrones secundarios o retrodispersados, se encargan de recolectar los electrones emitidos durante la interacción entre el haz de electrones y la superficie de la muestra en cada punto.

En la figura 19 se muestra un esquema de las diferentes técnicas derivadas de la interacción de los electrones con el material analizado.

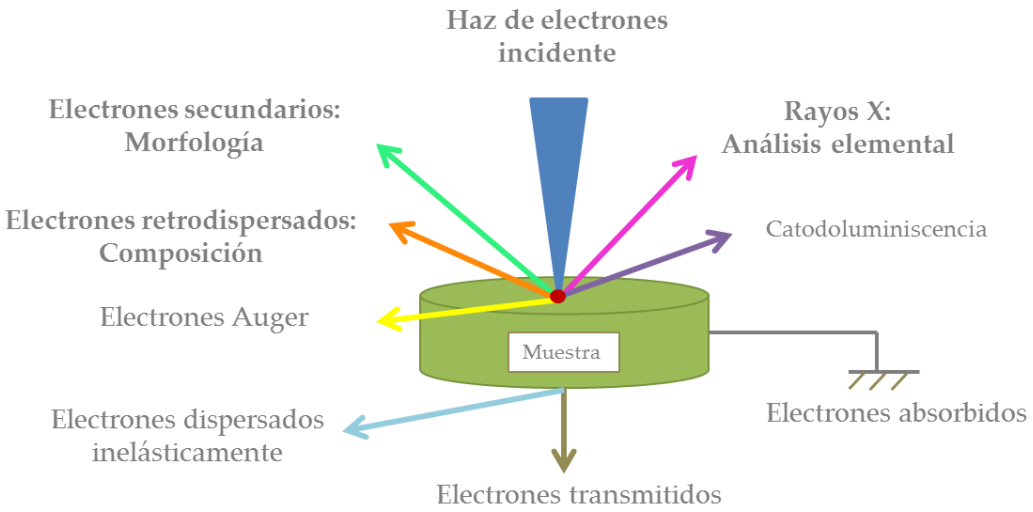

Figura 19. Representación esquemática de las diferentes técnicas derivadas de la interacción de los electrones con la materia.

A continuación, se describen los modos de operación del SEM empleados durante este trabajo:

- Modo de Imagen de Electrones Secundarios (SEI): En este modo, el SEM detecta electrones secundarios emitidos por la muestra debido a la interacción con el haz de electrones primarios. Los electrones secundarios proporcionan imágenes de alta resolución de la topografía de la superficie de la muestra. Este modo es

especialmente útil para observar la morfología de las muestras y analizar características superficiales.

- Modo de Imagen de Electrones Retrodispersados: En el modo de imagen de electrones retrodispersados se detectan electrones que son reflejados hacia atrás por la muestra. Este detector suele emplearse para la obtención de imágenes de muestras con varias fases. Según la densidad electrónica de cada fase será más o menos probable la formación de electrones retrodispersados; esta propiedad es la responsable de los distintos contrastes de fase, de modo que las fases más ligeras aparecerán más oscuras y las fases más densas, más claras.

- Modo de microanálisis por dispersión de energía de rayos-X: La espectroscopia de dispersión de energía de rayos X (EDX o EDS-SEM) permite la identificación y cuantificación de elementos químicos presentes en la muestra. Los electrones que impactan la muestra excitan los átomos; el análisis de la energía de los rayos X característicos emitidos permite determinar la composición elemental.

Las medidas fueron realizadas en el Servicio de Microscopía Electrónica, del Servicio General de Apoyo a la Investigación (SAI) de la Universidad de Zaragoza.

3.7. Difracción de rayos X

Además, se llevaron a cabo experimentos de difracción de rayos X (XRD) en polvo, obtenido por molienda de porciones de las barras. Las medidas fueron realizadas en el Servicio de Difracción y EXAFS, que forma parte del Servicio General de Apoyo a la Investigación (SAI) de la Universidad de Zaragoza, utilizando un difractómetro de Rayos X de ánodo rotatorio Rigaku D/max 2500, que se muestra en la figura 20.

El equipo está dotado de una fuente de rayos X con ánodo rotatorio de cobre, opera a 40 Kv y 80 mA y usa un monocromador de grafito para seleccionar la radiación de la línea K_α del Cu. La mayoría de los difractogramas se tomaron entre 5° y 70° con un *step* de 0.03° y 1s/step.

Los parámetros de red de las muestras analizadas se determinaron a partir de los datos de DRX con ayuda del software FullProf.[70]

Figura 20. Difractómetro empleado en las medidas de DRX

3.8. Raman

Las medidas de Raman se llevaron a cabo usando un espectrómetro Dilor XY, Francia, equipado con un detector CCD refrigerado con nitrógeno líquido. La excitación y detección se producen en un microscopio Olympus BH-2 a través de objetivos X50 de distancia de trabajo larga (~8 mm) o corta (≤1 mm). El mismo microscopio se utilizó para registrar imágenes ópticas de las muestras. La mayoría de las medidas Raman se hizo a temperatura ambiente usando como excitación diversas líneas (514.5, 496.5 y 488 nm) de un láser de Ar^+ de marca Coherent, modelo Innova 305C, o la línea de 568.4 nm de un láser de Kr^+ de Melles Griot, modelo 643-RYP-A02, dependiendo de las propiedades emisoras de las muestras y la disponibilidad de los láseres. Para las

medidas a temperatura variable se usó una platina calefactora Linkam TS1500V, que permite hacer medidas en atmósfera controlada. En esta tesis se hicieron medidas en aire y en vacío hasta 1000 °C.

3.9. Susceptibilidad magnética

La susceptibilidad magnética ($\tilde{\chi}$) es una magnitud que mide la respuesta de un material a un campo magnético externo (**H**). Esta respuesta se manifiesta en la magnetización (**M**) del material, que representa la densidad de momento magnético inducido. La relación entre la magnetización, la susceptibilidad y el campo magnético aplicado se describe mediante la ecuación fundamental de la susceptibilidad magnética (13):

$$\mathbf{M} = \tilde{\chi}\mathbf{H} \qquad (13)$$

Si el tensor $\tilde{\chi}$ es isótropo se puede prescindir del carácter vectorial y escribir, la expresión 14

$$M = \chi H \qquad (14)$$

donde M es la magnetización del material, es decir, la densidad de momento magnético inducido en el material, χ es la susceptibilidad magnética, que es una propiedad intrínseca del material, y H es la intensidad del campo magnético aplicado.

La susceptibilidad magnética es intrínseca a la estructura y las propiedades microscópicas del material y en este trabajo se empleó para analizar el estado de oxidación del praseodimio presente en las muestras fabricadas durante el desarrollo del primer objetivo de la tesis. En este trabajo se determina la susceptibilidad

magnética molar (χ_m) que se define como la susceptibilidad por mol de material. Para ello se hizo uso de un magnetómetro SQUID Quantum Design MPMS5 y se sometió a las muestras a un campo magnético de 1000 Oe. Las medidas fueron realizadas en el Servicio de Medidas Físicas, englobado en el Servicio General de Apoyo a la Investigación (SAI) de la Universidad de Zaragoza.

3.10. Espectroscopía de fotoelectrones emitidos por rayos X (XPS)

En esta técnica, la muestra es irradiada con rayos X de alta energía, generados típicamente por un tubo de rayos X. La interacción de estos rayos X con los átomos de la superficie de la muestra da lugar a la emisión de electrones de niveles internos, creando huecos electrónicos. La identificación de los átomos presentes en el compuesto sometido a análisis se basa en la siguiente ecuación (15):

$$E_{enlace} = E_{fotones} - (E_{cinética} + \phi) \qquad (15)$$

En esta ecuación, E_{enlace} representa la energía asociada a un electrón atraído por un núcleo; $E_{fotones}$ es la energía de los fotones de rayos X utilizados por el espectrómetro, y $E_{cinética}$ es la energía de los electrones eyectados de la muestra. La función de trabajo constituye un factor de corrección instrumental y se relaciona con la energía mínima requerida para expulsar un electrón de un átomo. Tanto la función de trabajo como la energía de los fotones son conocidas, siendo la energía cinética medida por el detector. Esto deja la energía de enlace como la única incógnita. El espectro resultante muestra picos de intensidad correspondientes a los diferentes elementos presentes en la muestra, y la posición de estos picos está relacionada con la energía de enlace de los electrones emitidos. Además de proporcionar información sobre la composición

elemental, la técnica también puede ofrecer detalles sobre el estado de oxidación de los elementos y la presencia de diferentes especies químicas en la superficie.

Esta técnica la empleamos para determinar el estado de oxidación del praseodimio presente en las muestras del sistema ZrO_2-PrO_x. Las medidas se han realizado en el Laboratorio de Microscopías Avanzadas (LMA) del Instituto de Nanociencia y Materiales de Aragón. El equipo empleado es el espectrofotómetro de fotoelectrones de rayos X (XPS/AES) Modelo Kratos Axis Ultra DLD y el software de análisis de datos, el CasaXPS.

3.11. Termogravimetría

La termogravimetría (TG) se emplea para estudiar los cambios en la masa de una muestra a medida que se somete a un programa controlado de temperatura.

Durante un experimento de termogravimetría, la muestra se coloca en una celda de medición y se calienta o enfría a una velocidad controlada. Un sistema de registro continuo mide la masa de la muestra en función de la temperatura o del tiempo. La curva termogravimétrica resultante muestra cambios en la masa de la muestra a lo largo del tiempo o de la temperatura. Las pérdidas de masa o ganancias están asociadas con cambios físicos o químicos en la muestra.

En este trabajo se empleó la termogravimetría para estudiar los procesos de oxidación o reducción que podían tener lugar en las muestras al someterlas a un programa de temperatura.

Para ello se empleó un TA Instruments SDT2960 para medidas TGA que permite calentar en atmósfera de nitrógeno o aire hasta una temperatura máxima de 900 °C.

Las medidas fueron realizadas en el Servicio de Análisis Térmico del INMA.

3.12. Nano-TC de rayos X

La nanotomografía computarizada de rayos X (nano-TC de rayos X) es una técnica que permite obtener de imágenes tridimensionales detalladas de estructuras internas de materiales en dimensiones a nivel nanométrico.

La nano-CT de rayos X utiliza rayos X para penetrar y atravesar un material y recopila datos en múltiples ángulos. Luego, mediante algoritmos computacionales avanzados, se reconstruye una imagen tridimensional de la muestra, revelando información detallada sobre su estructura interna a escala nanométrica.

Esta técnica se utilizó en el presente trabajo para analizar la disposición interna (tamaño, conectividad) de los canales obtenidos en los eutécticos de MgSZ/MgO tras el vaciado con HCl. Las medidas fueron realizadas por el Dr. Bailey, del Electrochemical Innovation Lab, Department of Chemical Engineering, University College London, en un equipo Zeiss Xradia 810 Ultra (Carl Zeiss).

3.13. Espectroscopía de impedancia

La espectroscopia de impedancia se utiliza para estudiar la respuesta eléctrica de sistemas en función de la frecuencia de la señal aplicada. Esta técnica se empleó para determinar la conductividad eléctrica total de las muestras producidas para la fabricación de la membrana con permeación selectiva al CO_2. Las medidas fueron realizadas por la Dra. R. I. Merino, del INMA, utilizando un equipo SI 126.0

Schlumberger Instruments, en un rango de frecuencias de 1 a 10^6 Hz y temperaturas entre 25 y 600 - 850 °C, según el material a estudiar.

3.14. Medidas de permeación

En principio, la membrana fabricada está pensada para trabajar en un rango de temperaturas de entre 400 °C y 800 °C. El límite inferior de temperatura está condicionado por el punto de fusión de la mezcla eutéctica de carbonatos que, como hemos comentado previamente, facilita el paso selectivo de CO_2 a través de los canales de la membrana fabricada. El límite superior lo marca la estabilidad del soporte y/o de los carbonatos.

Los experimentos de permeación se llevaron a cabo durante sendas estancias de investigación predoctoral en el laboratorio Materials, Concepts and Reaction Engineering (MatCoRE) de la Universidad de Newcastle, liderado por el Prof. Ian Metcalfe. Para ello se utilizó un reactor de membrana fabricado a medida y operado a presión atmosférica. El reactor tiene integrado un horno (Figura 21(a)) con un controlador (Figura 21 (b)) que permite establecer un programa de temperaturas.

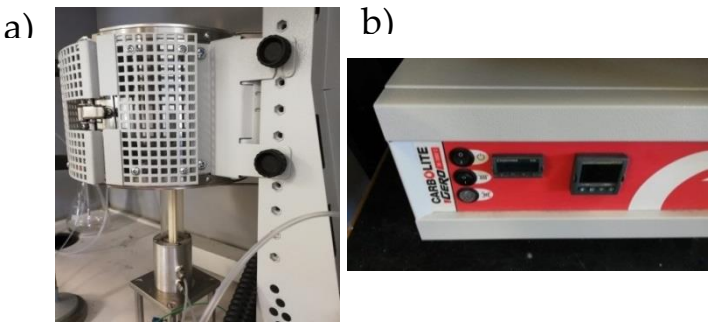

Figura 21. Imagen del sistema de medidas de permeación, que incluye un horno (a), con un controlador de temperatura (b).

Con el fin de determinar con precisión la temperatura, se colocó un termopar (figura 22) lo más cerca posible de la membrana, la cual estaba adherida a un tubo de YSZ mediante pasta de oro.

a)  b) 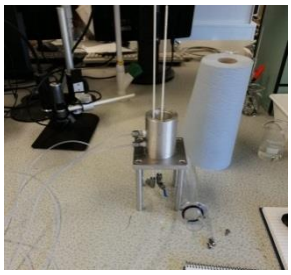

Figura 22. Controlador de temperaturas (a) y termopar (b) del sistema de medidas de permeación.

El dispositivo de permeación (figura 23) consta de dos cámaras: una cámara interna en el lado de alimentación y una cámara externa en el lado de permeado, cerradas por la membrana y un tubo de cuarzo, respectivamente.

Figura 23. Dispositivo de permeación.

El gas de alimentación consistió en una mezcla con un 50% mol de CO_2, 25% mol de N_2 y 25% mol de O_2, mientras que el gas de barrido en el lado del permeado fue argón de alta pureza. Dado que la selectividad de los carbonatos fundidos al CO_2 es a priori muy elevada, el uso de N_2 en el lado de alimentación tiene como función detectar posibles

fugas transmembrana; es decir, si se detectaba N_2 significativamente por encima de los niveles de fondo, se detenían los experimentos debido a la evidencia de una fuga.

Todos los gases fueron suministrados y certificados por BOC Ltd. Los flujos en ambos lados, de alimentación y permeado, se mantuvieron a una velocidad total de flujo de gas de 30 ml min^{-1}.

Los gases en el lado de permeado (CO_2, N_2 y O_2) fueron analizados mediante un espectrómetro de masas (HIDEN, HALO 100-RC) (figura 24(a)). Se tuvo en cuenta la superposición de las señales de CO y N_2 en el canal m/z = 28 y se corrigió el flujo de N_2 en consecuencia. La concentración de CO_2 en el lado de permeado también se analizó mediante un analizador de infrarrojos (XTREAM-Enhanced General-Purpose Process Gas (XEGP), Emerson Process Management Limited) (figura 24 (b)) en serie y después del espectrómetro de masas.

a) b)

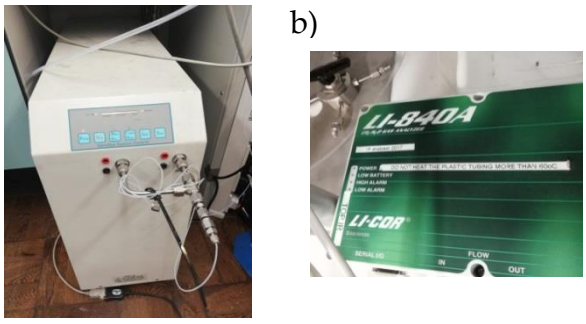

Figura 24. Analizadores de los gases de salida (a) Espectrómetro de masas y (b) infrarrojo.

Tanto el analizador de infrarrojos como el espectrómetro de masas se calibraron antes de cada experimento para tener en cuenta errores sistemáticos y deriva del instrumento, mediante el flujo de gases de N_2 y CO_2 con fracción molar certificada. La

fracción molar de los gases de calibración se eligió lo más cercana posible a la fracción molar esperada en el lado de permeado durante los experimentos de permeación. Se utilizó argón para la calibración de fondo de todos los instrumentos.

El flujo de gases al aparato de permeación se controló mediante controladores de flujo de masa (Brooks Smart II). Las tasas de flujo se confirmaron en la salida del lado de permeado utilizando un medidor de flujo digital Varian (serie 1000).

3.15. Estudios de microindentación

Para estudiar si la dureza de las muestras obtenidas para su uso como implante óseo (objetivo 2.2) es apta para su aplicación, se llevaron a cabo microindentaciones en las superficies pulidas de las muestras sin sumergir, utilizando un indentador Vickers de diamante con forma de pirámide, en un microdurómetro Matsuzawa, MXT 70. Se realizaron las pruebas aplicando una carga de 200 gf durante 15 s. Se efectuaron al menos 10 indentaciones válidas para cada muestra, y los datos se presentan como valores medios con desviaciones estándar.

4. Publicaciones

Journal of Alloys and Compounds 923 (2022) 166449

Contents lists available at ScienceDirect

Journal of Alloys and Compounds

journal homepage: www.elsevier.com/locate/jalcom

Research article

Pyrochlore-like ZrO_2-PrO_x compounds: The role of the processing atmosphere in the stoichiometry, microstructure and oxidation state

L. Grima, J.I. Peña, M.L. Sanjuán*

Instituto de Nanociencia y Materiales de Aragón, Universidad de Zaragoza-CSIC, Facultad de Ciencias, Universidad de Zaragoza, 50009 Zaragoza, Spain

ARTICLE INFO

Article history:
Received 23 March 2022
Received in revised form 11 July 2022
Accepted 20 July 2022
Available online 21 July 2022

Keywords:
Ceramics
Oxide materials
Laser processing
Microstructure
Oxidation
Phase diagrams ZrO2–PrOx
Phase diagram
Processing atmosphere
Praseodymium oxidation
Pyrochlores

ABSTRACT

The object of this work is to study the relation between composition, microstructure and oxidation state of $Pr_{2\pm x}Zr_{2\mp x}O_{7\pm y}$ materials produced by the laser–floating zone (LFZ) technique. Three compositions are studied, nominally $Pr_{1.7}Zr_{2.3}O_{7+y}$, $Pr_2Zr_2O_{7+y}$ and $Pr_{2.24}Zr_{1.76}O_{7\pm y}$, all within the pyrochlore field in the ZrO_2–PrO_x phase diagram. Samples have been processed under four different atmospheres (O_2, air, N_2 and 5%H_2(Ar)), so as to vary the environmental conditions from oxidising to reducing. Sample colouration ranged from dark brown to bright green, owing to varying Pr^{4+} content. A close correlation is found between the phase homogeneity, the microstructure and the Pr content. Pr–deficient samples present a homogeneous microstructural aspect and composition, whereas Pr–rich compositions always break into 5–25 μm–sized grains with pyrochlore phases at the grain centre and ill–crystallised, Pr–rich oxidised phases at the grain–boundaries. Raman spectroscopy shows that different types of oxygen disorder occur depending on composition and processing atmosphere: in Pr–poor samples oxygen interstitials are created to compensate for Zr^{4+} excess charge, whereas in Pr–rich samples oxygen disorder occurs around the Pr^{3+} or Pr^{4+} ions substituting for Zr^{4+}, because of size–mismatch. Magnetic measurements showed a high Pr^{4+} content, which has been attributed to several factors: the highly oxidised state of the feedstock material, the segregation of Pr and O–rich grain boundaries in compositions with praseodymium molar rate > 0.5, and the lower oxide–ion conductivity for PZO compositions, compared to either Pr–poor or Pr–rich compositions. Post–processing thermal annealing in a vacuum at 1000 °C enabled total Pr reduction, with the exception of the Pr–rich P2.24 samples, where some Pr^{4+} ions remained in the oxidised state.

1. Introduction

Cerium–related oxides are currently used in many applications such as three–way catalysts for exhaust gas conversion or air pollution abatement, hydrogen production, solid oxide fuel cells, etc. (see Ref. [1] and references therein). Applications based on the behaviour of ceria as oxygen storage compound (OSC) rely on the redox reaction, $2Ce^{4+} + O_O^x \leftrightarrows 2Ce^{3+} + ½O_2(g) + V_O^{\bullet\bullet}$, where O_O^x and $V_O^{\bullet\bullet}$ stand for a lattice oxygen ion and vacancy, respectively, in Kröger–Vink notation. In its use as OSC, ceria is usually combined with other oxides, such as ZrO_2, to gain stability upon sintering and lower the temperature of redox conversion. More recently, mixing with praseodymium oxides has been tried to further improve the oxygen storage capacity of Ce–based compounds, taking benefit of the Pr redox reaction analogous to that of ceria, $2Pr^{4+} + O_O^x \leftrightarrows 2Pr^{3+} + ½O_2(g) + V_O^{\bullet\bullet}$ [2]. In this line, many reports have been published about OSC properties of binary or ternary solid solutions of CeO_2, ZrO_2 and PrO_x. Most of the work has been devoted to the CeO_2–PrO_x system, where it is found that doping ceria with ~50% of Pr lowers the reduction temperature from ~850 to ~450 °C[3,4].

The OSC properties of the ZrO_2–PrO_x system have also been studied, both around the pyrochlore composition $Pr_2Zr_2O_7$ as in the Pr–rich region, usually in samples synthesized by low–temperature methods [4–9]. In general, the best results (as regards for instance H_2 consumption in temperature–programmed reduction (TPR) experiments) are obtained for fluorite–like compounds with Pr contents equal to or higher than 75%. As the OSC properties of ZrO_2–PrO_x oxides rely on oxygen incorporation and release through the above redox reaction, they involve stoichiometry changes that may result in phase evolution during operation. Then, a detailed knowledge of the phase diagram (PD) allowing for redox effects is mandatory. However, some published phase diagrams still present ambiguities, especially in the high temperature sections (see Fig. S1 of supporting information) [10,11]. In this work we have undertaken a study of ZrO_2–PrO_x materials around the pyrochlore composition, produced by a laser–assisted melting and resolidification technique.

* Corresponding author.
E-mail address: sanjuan@unizar.es (M.L. Sanjuán).

https://doi.org/10.1016/j.jallcom.2022.166449

Processing has been made in four different environments: O_2, air, N_2 and 5%H_2(Ar), so as to identify the phases formed in a range of environmental conditions covering from more to less oxidising ones. The resulting phases have been characterised by means of X–ray diffraction, electron microscopy and microanalysis, magnetic susceptibility, X-ray photoelectron spectroscopy (XPS) and Raman spectroscopy, with the purpose of elucidating the structure, composition, atomic distribution and oxidation effects related to the presence of the Pr component. All these factors (in particular those related with variations in Pr oxidation state and oxygen content) are relevant for redox properties of the mixed compounds. Previous reports of $Pr_2Zr_2O_7$ pyrochlore produced by floating–zone methods have focused mainly on structural and magnetic properties [12,13].

2. Materials and methods

2.1. Synthesis of ceramic precursors

Ceramic rods of $Pr_{2\pm x}Zr_{2\mp x}O_{7\pm y}$ with different Pr content were prepared by solid state reaction. Powders of Pr_6O_{11} (purity 99.9%, Merck, Darmstaadt, Germany) and ZrO_2 (purity 99%, Merck, Darmstaadt, Germany) were sternly heated at 1200 °C and then mixed in three different ratios so as to get nominal compositions $Pr_{1.70}Zr_{2.30}O_{7+x}$ (labelled as P1.70), $Pr_2Zr_2O_{7+x}$ (PZO), and $Pr_{2.24}Zr_{1.76}O_{7+x}$ (labelled as P2.24). To compensate for the likely Pr volatilisation [12], a ~2% Pr excess was added to the nominal compositions. However, volatilisation was seen to vary with the processing atmosphere and solidification rate, being larger in oxidising atmospheres and almost negligible in neutral or reducing atmospheres at the fast processing rates used in this work. As a result, the ZrO_2/PrO_x proportion in oxidising conditions is very close to the nominal one whereas a small Pr excess remains in neutral or reducing atmospheres.

The powder mixture was then introduced in a latex tube, and shaped into a rod using a hydraulic press under a pressure of 200 MPa. After their removal from the tube, the rods were sintered at 1500 °C in air during 12 h. The brownish–colour sintered rods presented a diameter between 3 and 4 mm and were roughly 7 cm in length.

2.2. Crystal growth

Crystalline samples with a diameter of approximately 2 mm were grown, from the sintered rods, by the laser floating zone technique (LFZ) using a CO_2 laser (λ = 10.6 μm) as heating source (Blade- 600, Electronic Engineering). The growth rate was fixed at 300 mm/h, although some samples were processed at 100 mm/h to verify the influence of the growth rate in the stoichiometry and Pr oxidation sate.

In order to study the influence of the processing atmosphere on the stoichiometry and oxidation degree, samples were grown in different atmospheres (O_2, air, N_2, and 5%H_2 in Ar). The growth chamber was kept at a slight overpressure of 0.1–0.25 bar with respect to ambient pressure.

2.3. Characterization

Semi–quantitative compositional analysis and morphology were characterized by means of Field Emission Scanning Electron Microscopy (FESEM) using a Carl Zeiss MERLIN microscope with Energy Dispersive X–ray detector (EDX) incorporated.

XPS spectra were collected in a Kratos Axis SUPRA spectrometer employing a monochromatic Al Kα (1486.6 eV) X-ray source. The spectra were analysed using the CASA-XPS software. A Shirley-like baseline was used for background subtraction.

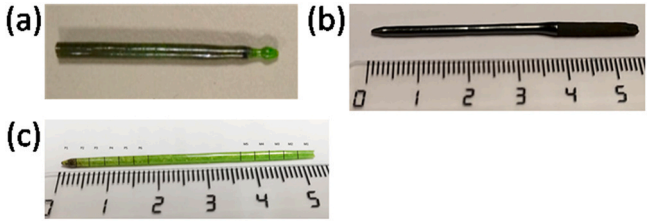

Fig. 1. PZO samples processed at 300 mm/h in 5%H_2(Ar) (a) and O_2 atmosphere (b), and at 100 mm/h in 5%H_2(Ar) (c).

The crystalline nature of the samples was analysed by powder X–ray diffraction (XRD). The data were collected with a D–Max Rigaku, Ru300 diffractometer, using the Cu K_α radiation. Patterns were measured from 5° to 70–80° with 2θ step = 0.03° and 1 or 3 s/step. Lattice parameters were determined from XRD data with the help of FullProf software [14].

Raman measurements were performed using a microprobe spectrometer (Model XY, Dilor, France) with a CCD detector. Spectra were taken at room temperature (RT) with a X50 microscope objective lens, using the 514.5 nm line of an Ar^+ laser (model Coherent INNOVA 305).

Magnetic susceptibility was obtained from magnetization measurements, under a magnetic field of 1000 Oe, performed on a SQUID detector magnetometer Quantum Design MPMS5.

3. Results

Samples with non–uniform colouration were obtained depending on the composition and processing atmosphere, a fact that may be attributed to inhomogeneity in the Pr oxidation state (Fig. 1). In Pr oxides, bright green and dark brown colours are indicative of Pr^{3+} and Pr^{4+} valence states, respectively, according to their different electronic configurations and related absorption bands in the uv–-visible spectral region. When both valence states are present, the sample adopts intermediate coloration between green and brown, depending on the Pr^{3+}/Pr^{4+} proportion. As a general rule, samples processed at 300 mm/h presented a radial colour gradient from greenish in the rod centre to brownish at the edge, this trend being more evident for samples grown in non–oxidising atmospheres. During the crystal growth process the vaporization of a brown powder takes place, especially in oxidising atmospheres. Previous work on LFZ–processed $Pr_xZr_yO_z$ compounds report it to be a praseodymium oxide. [12].

3.1. Scanning electron microscopy and EDX analysis

The microstructure of the processed $Pr_{2\pm x}Zr_{2\mp x}O_{7\pm y}$ samples was studied by Scanning Electron Microscopy (SEM) and their composition analysed by EDX. Fig. 2 shows backscattered–electron images of the transverse sections of PZO samples processed in O_2 (a) and 5% H_2(Ar) (b), and of P1.70 (c) and P2.24 (d) samples processed in 5% H_2(Ar). Other pictures can be found in Fig. S2 of the supporting information. Cation compositions determined by EDX are given in Table 1 in terms of the praseodymium molar rate (PMR, defined as the ratio between cation percentages Pr/(Pr+Zr)). Nominal PMR are 0.425, 0.50 and 0.56 for P1.70, PZO and P2.24 compositions, respectively.

P1.70 samples present large (> 100 μm) crystalline grains and a homogenous grey contrast in the whole sample (Fig. 2c; erosions in the surface are due to polishing). Accordingly, a uniform composition was found in EDX analyses, with PMR depending on the processing atmosphere (see Table 1). Lower PMR are systematically found in oxidising atmospheres in this and other compositions, which is attributed to higher Pr volatilisation. Note that a ~2% Pr

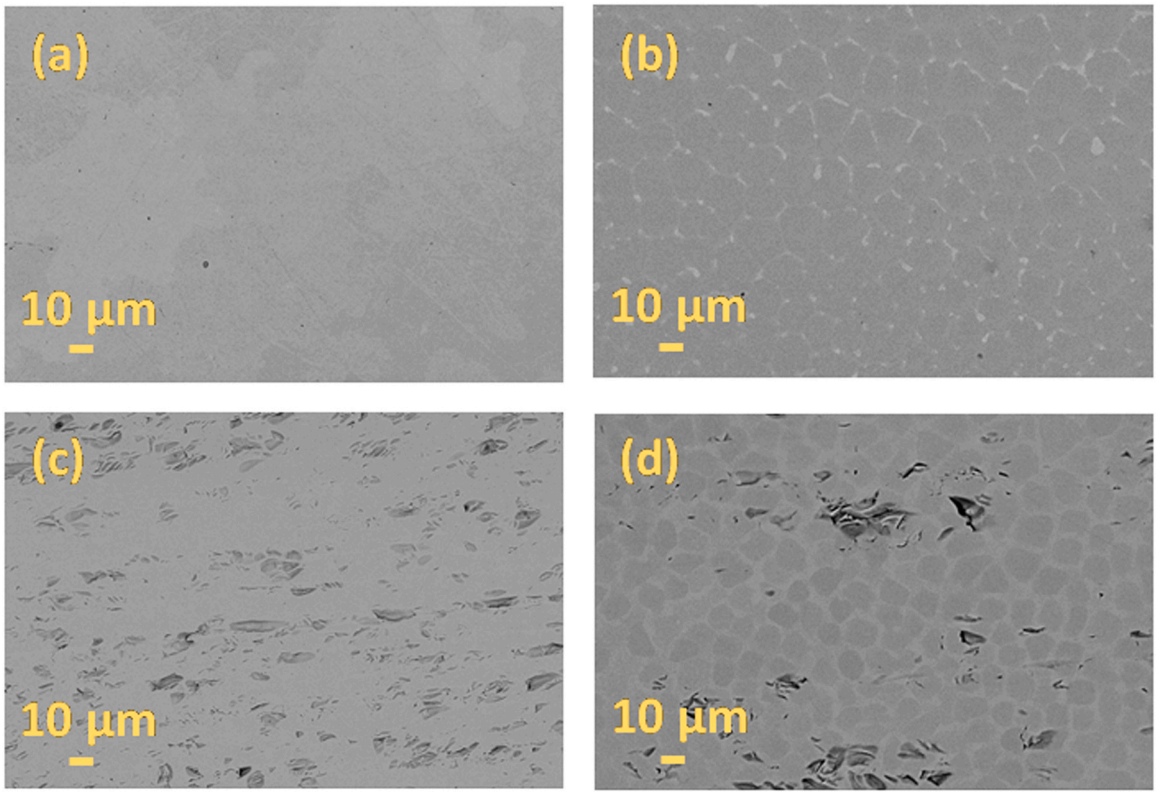

Fig. 2. Scanning Electron Microscopy images of PZO samples processed at 300 mm/h in (a) O_2 and (b) 5%H_2(Ar); (c) P1.70 processed in 5%H_2(Ar) and (d) P2.24 in 5%H_2(Ar).

excess was added to compensate for the eventual Pr loss, with the final result that samples processed in non–oxidising atmospheres present a slight Pr excess with respect to the nominal one.

At the other end, P2.24 samples display ~5–25 µm large quasi–-hexagonal grains throughout the whole transverse section, with dark and light grey contrasts at the grain centre (GC) and boundary (GB), respectively (Fig. 2d). EDX analyses showed that grain boundaries have much higher Pr content (PMR between 0.6 and 0.8) than the grain centres, and also a higher oxygen content, but a precise determination of the composition was not possible because of the narrow width (1–2 µm) of those regions, which is at the limit of EDX resolution. EBSD maps (Fig. S3) confirmed the Pr enrichment at the grain boundaries.

The "average" column in Table 1 represents measurements made over large areas (≥120 µm) so as to get a spatial average. The volume proportion of GB in Pr-rich compounds has been estimated by image analysis and is found to vary between 10% and 20%, but these numbers have to be considered just as indicative, because the GB have not precise spatial limits, neither a homogeneous composition and appear intermixed with the main (grain centre) phase.

Statistical analyses of grain sizes in different samples and atmospheres are given in Fig. S4.

The microstructure of the PZO samples is intermediate between those of P1.70 and P2.24, and depends on the processing atmosphere. Samples processed in oxidising atmospheres exhibit an inhomogeneous grey distribution at a 10–100 µm scale (Fig. 2a) and PMR ranging between 0.47 and 0.5, with average values slightly below 0.5. On the other hand, samples processed in N_2 and in 5% H_2(Ar) present two different types of regions: the first one displays large regions with slight grey contrast variation, as in Pr–poor samples, and PMR close to 0.5; the second one is formed by ~5–20 µm–sized quasi–hexagonal grains (Fig. 2b, S2 and S4), as in Pr–rich samples, with dark contrast at the grain centre (PMR ~0.5) and a narrow light–contrast phase at the boundaries with higher PMR and oxygen content.

In summary, a close correlation exists between the microstructural aspect and the average cation composition: large areas (100 µm scale) with small compositional fluctuations are found when PMR is below or at 0.5, and small grains (20 µm scale) form when the average PMR is higher than 0.5. In these grains segregation is observed between an inner region with PMR close to 0.5 and a Pr and oxygen rich outer shell with PMR reaching values of 0.8. Both types of regions can be present in the same sample, depending on the local cation composition.

Table 1
Praseodymium molar rate derived from EDX analyses of $Pr_{2\pm x}Zr_{2\mp x}O_{7\pm y}$ samples as a function of processing atmosphere. The average PMRs can be compared with nominal ones, 0.425, 0.50 and 0.56 for P1.70, PZO and P2.24 compositions, respectively, and with the actual compositions of the reagent oxide mixtures, where a 2% PrO_x excess was added to compensate for likely Pr volatilisation and thus amount to 0.433, 0.51 and 0.57 for P1.70, PZO and P2.24, respectively. H_2 stands for 5%H_2(Ar) atmosphere.

Label	O_2			Air			N_2			H_2		
P1.70	0.420			0.424			0.428			0.446		
	Range		**Aver.**	**Range**		**Aver.**	**Range**	**GC**	**Aver.**	**Range**	**GC**	**Aver.**
PZO	0.487–0.497		0.495	0.494–0.503		0.498	0.497–0.51	0.519	0.511	0.495–0.51	0.517	0.512
	GC	**GB**	**Aver.**	**GC**	**GB**	**Aver.**	**GC**	**GB**	**Aver.**	**GC**	**GB**	**Aver.**
P2.24	0.555	> 0.6	0.557	0.547	> 0.6	0.559	0.556	> 0.6	0.576	0.554	> 0.6	0.575

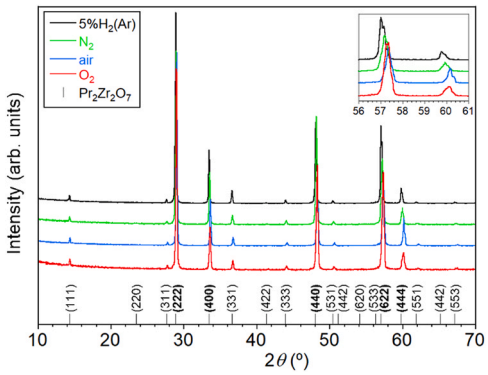

Fig. 3. X–Ray diffractograms of PZO samples processed in different atmospheres. The inset shows a magnification of the 56–61° region and the tics stand for the allowed reflections and (*hkl*) indices of the $Pr_2Zr_2O_7$ pyrochlore (*a*= 10.7099 Å), according to entry #249972 of the ICSD (Inorganic Crystal Structure Database). The main reflections, common to pyrochlore and fluorite lattices (although with doubled indices in the pyrochlore) are indicated in boldface. The remaining reflections are pyrochlore superstructure peaks.

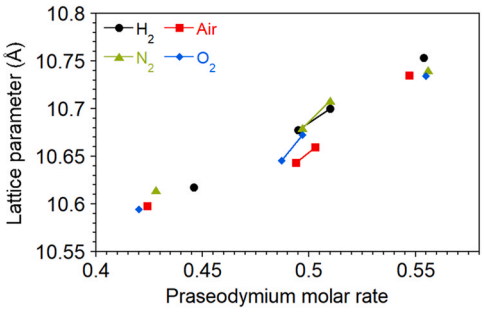

Fig. 4. Evolution of lattice parameters with the Pr molar rate determined from EDX. H_2 stands for 5%H_2(Ar) atmosphere.

3.2. X–ray diffraction

Fig. 3 shows the XRD patterns of PZO samples processed by laser floating zone at 300 mm/h in O_2, Air, N_2 and 5%H_2(Ar). The patterns of the P1.70 and P2.24 samples are shown in Figs. S5 and S6 of the supporting information.

Although the main peaks are characteristic of fluorite–like phases, the presence of weak superstructure additional peaks is indicative of pyrochlore–like phases ($Fd\bar{3}m$ space group, SG). However, most PZO and P2.24 samples evidence shoulders at the low–angle side of high–index reflections (see inset) that suggest some composition inhomogeneity, in agreement with EDX results.

An attempt has been made to determine crystallite sizes by means of the Scherrer formula, including the instrumental linewidth correction. This gives crystallite sizes $\lesssim$ 100 nm, much smaller than the size observed in SEM images. We attribute the apparent discrepancy to the peak linewidth arising not just from the crystallite size but including also other contributions, such as composition fluctuations, strain, etc., of difficult quantification.

XRD patterns were refined using the FullProf package. [14] The presence of compositional fluctuations was handled by including two close phases in the fitting procedure, when necessary, although the real situation should be more like a continuum of phases with a distribution of lattice parameters. Only one phase of pyrochlore type was required for P1.70 compositions whereas two pyrochlores were used for PZO and P2.24 samples. The requirement of two pyrochlores (and not a pyrochlore plus a fluorite phase) was ascertained from a comparison of the pyrochlore superstructure peaks fitted with either one or two pyrochlore phases (Figs. S7 and S8 of the supporting information). The assumption was further supported by the close values of the lattice parameters found for both phases. The lattice parameters obtained are listed in Table 2 and plotted in Fig. 4 as a function of the PMR determined from EDX. In drawing Fig. 4a correspondence has been established between the "phases" with low and high lattice parameters and regions with low and high Pr content found by EDX, respectively. Note that for PZO and P2.24 compositions displaying quasi–hexagonal grains no correspondence exists between the Pr–rich grain boundaries and the ad–hoc second phases introduced in the fitting. The high PMR (> 0.6) found at the grain boundaries should belong to phases with much larger lattice parameters, not expected to be of pyrochlore type. We then conclude that grain boundaries are not detected in these XRD measurements, a fact that may be ascribed to the non–uniform composition and ill crystallisation of those regions.

The gradual increase of the lattice parameters with the Pr content is in consonance with the greater size of both Pr^{3+} and Pr^{4+} compared with Zr^{4+}. Differences in the lattice parameters for a fixed composition may be attributed to variations in the Pr oxidation state. The more reducing the atmosphere, the higher the expected lattice parameter, owing to the larger ionic radius of Pr^{3+} compared to Pr^{4+}. In general, P1.70 and P2.24 samples fit to a single trend, suggesting that for these compositions Pr oxidation effects are small. For PZO samples grown in air or O_2, however, the lattice parameters are much smaller than for other atmospheres, which suggests a higher oxidation state. To elucidate the degree of Pr oxidation (and associated variation of oxygen stoichiometry) as a function of PMR and processing atmosphere we have performed magnetic susceptibility and XPS measurements, which are presented in next sections.

3.3. Magnetic susceptibility

Magnetic susceptibility measurements were performed to get a picture of the relative Pr^{3+}/Pr^{4+} proportion in processed samples, with the assumption that the effective magnetic moments derived from these data are representative of the average Pr oxidation state.

Magnetic susceptibilities of the $Pr_{2\pm x}Zr_{2\mp x}O_{7\pm y}$ samples were obtained from magnetization measurements between 1.8 K and 305 K under a magnetic field of 100 mT (Fig. S9 of the supporting information). The effective magnetic moments per Pr ion (μ_{eff}) were determined from the fit of the high temperature range (from 195 K to 305 K) of the inverse molar susceptibility to the expression $\chi^{-1} = [C/(T - \theta) + \chi_0]^{-1}$, where θ is the Curie–Weiss (CW) temperature and C is the Curie constant. The χ_0 term was added to the usual CW expression to account for the temperature–independent Van–Vleck paramagnetism [15] and was fitted by the procedure specified below. The effective magnetic moments and the relative content of

Table 2
Lattice parameters (in Å) of pyrochlore phases found in $Pr_{2\pm x}Zr_{2\mp x}O_{7\pm y}$ samples processed in different atmospheres. As explained in the text, second phases with larger lattice parameter (assigned to higher PMR) were introduced to fit the low angle tail of the diffraction peaks. H_2 stands for 5%H_2(Ar) atmosphere.

Label	O_2		air		N_2		H_2	
	Low PMR	High PMR	Low PMR	High PMR	Low PMR	High PMR	Low PMR	High PMR
P1.70	10.5941		10.5982		10.6099		10.6184	
PZO	10.6457	10.6722	10.6434	10.6595	10.6796	10.7085	10.6776	10.6998
P2.24	10.7345	10.7460	10.7348	10.7581	10.7406	10.7608	10.7535	10.7684

Pr^{3+} and Pr^{4+} ions were worked out from the relations $\mu_{eff}^2 = 8\,C$ and $\mu_{eff}^2 = \alpha\mu_{Pr3+}^2 + (1-\alpha)\mu_{Pr4+}^2$, where $\mu_{Pr3+} = 3.58\ \mu_B$ and $\mu_{Pr4+} = 2.54\ \mu_B$ are the free–ion magnetic moments of the ground–state multiplets of Pr^{3+} and Pr^{4+} ions, respectively, and μ_B is the Bohr magneton. To account for Pr volatilisation effects, the molecular mass and the number of moles in each sample were worked out using the actual cation compositions determined from EDX analyses, not from the nominal ones.

The value of χ_0 was determined as follows. First of all, we assumed that the $Pr_2Zr_2O_7$ sample solidified in 5%H_2(Ar) atmosphere at 100 mm/h, presenting a bright green colour (see Fig. 1c), contained only Pr^{3+} ions. The fit of the magnetic susceptibility of that sample to a CW term without χ_0 yielded an unreasonably large $\mu_{eff} = 3.69\ \mu_B$, and inclusion of a temperature independent term $\chi_0 = 1.8 \times 10^{-4}$ emu/mol was required to get a magnetic moment equal to the reference value of Pr^{3+}, $\mu_{eff} = 3.58\ \mu_B$. For other compositions and/or atmospheres χ_0 was fixed in a self–consistent way under the assumption that the Van Vleck correction for Pr^{4+} ions can be neglected. Then, χ_0 was varied in an iterative way until the proportion of Pr^{4+} ions resulting from the fit of the inverse molar susceptibility was coincident with the assumed Pr^{4+} content. The effective moments and χ_0 values resulting from this analysis are given in Table 3. The last column shows the percentage of Pr^{4+} ions relative to the total Pr content of each sample. With the approximations involved, the error in the Pr content is estimated to be ± 2%. The PMR column corresponds to values determined from EDX in wide areas of the samples, which average regions with high and low PMR. Fig. 5 displays the Pr^{4+} relative content as a function of the PMR.

We can first notice that for fixed composition the Pr^{4+} content depends on the processing atmosphere, so that a higher Pr^{4+} content is obtained for samples processed in oxidising atmospheres, as a general rule. For nominal P1.70 composition, the Pr^{4+} relative content is between 10% and 20%. A slightly higher percentage (13–24%) is obtained for the Pr–rich side of the pyrochlore field, nominally P2.24. However, it is somewhat surprising to find high Pr^{4+} percentages for intermediate Pr compositions (PMR ~0.5), even for those grown in 5%H_2(Ar). This is contrary to the expectation that Pr is more likely to get oxidised as PMR increases in $Pr_{2\pm x}Zr_{2\mp x}O_{7\pm y}$ compounds, as reported in previous works [6]. The Pr^{4+} content of a given sample is the result of several processes, namely oxygen diffusion across the sample, either in the melt or in the solidified rod, and oxygen release to the LFZ chamber, both depending on the processing atmosphere and sample temperature which in turn depends on the cooling rate. As we are using oxygen–rich precursors (made from Pr_6O_{11} reagents) and relatively fast solidification rates, it is not surprising that oxygen excess remains in the pyrochlores, even for those grown in reducing atmospheres. Experimental evidence supports this hypothesis: first, samples grown at 100 mm/h, such as the one shown in Fig. 1c, present a much lower or even null Pr^{4+} content. Second, annealing the P1.70 and PZO samples at 1000 °C in a vacuum resulted, independently of the processing atmosphere, in a change to green colour (see Fig. S10), as corresponds to the reduction of the existing Pr^{4+} to Pr^{3+}. A noticeable increase of the lattice parameter was accordingly observed for the most oxidised PZO sample (processed in air) after the thermal treatment in vacuum (Fig. S10). The lattice parameter change was much smaller for the P1.70 sample processed in air after the same treatment, which is attributed to the lower Pr^{4+} content in the as–prepared sample. The same treatment applied to P2.24 samples did not change the colour nor the lattice parameter, within error, which is attributed to the high stability of Pr^{4+} ions at the *B* site of Pr–rich pyrochlores, required to maintain charge neutrality without the need of oxygen vacancies. Finally, as noted before, many samples showed a colour gradient, from greenish at the centre to increasingly brownish near the edge. This trend was especially visible for samples processed in non–oxidising atmospheres. The segregation of Pr and O rich grain boundaries in PZO samples grown in reducing atmosphere was also evident (Fig. 2). We note that the Pr^{4+} percentages derived from magnetic susceptibility measurements are average values so that the presence of even small amounts of more oxidised Pr–rich regions results in higher than expected relative Pr^{4+} contents.

Table 3
Effective magnetic moment, temperature independent χ_0 term and Pr^{4+} content for $Pr_{2\pm x}Zr_{2\mp x}O_{7\pm\delta}$ samples. H_2 stands for 5%H_2(Ar) atmosphere.

	Atmosphere	PMR	$\chi_0 \cdot 10^{-4}$ (emu/mol)	μ_{eff} (μ_B)	%Pr^{4+}
P1.70	O_2	0.420	1.25	3.43	16.52
	Air	0.424	1.2	3.4	19.74
	N_2	0.428	1.3	3.46	13.27
	H_2	0.446	1.45	3.49	10.00
PZO	O_2	0.495	1.35	3.39	20.35
	Air	0.498	1.15	3.25	35.41
	N_2	0.511	1.6	3.48	10.72
	H_2	0.512	1.4	3.36	23.99
PZO 100 mm/h	H_2	0.510	1.8	3.58	–
P2.24	O_2	0.557	1.5	3.36	23.99
	Air	0.559	1.6	3.39	20.81
	N_2	0.568	1.7	3.42	17.60
	H_2	0.581	1.75	3.46	13.27

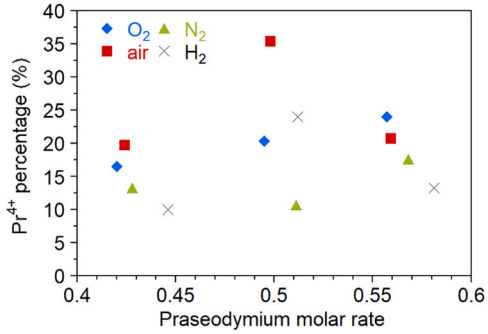

Fig. 5. Pr^{4+} percentage as a function of praseodymium molar rate for $Pr_{2\pm x}Zr_{2\mp x}O_{7\pm x}$ samples processed at different atmospheres (O_2, air, N_2, 5%H_2(Ar)).

3.4. XPS

In view of the rather high Pr^{4+} content yielded by magnetic susceptibility data in some samples, XPS spectra were recorded to validate the magnetic measurements results. Fig. 6 shows the Pr 3*d* spectra of the PZO sample processed in air at 300 mm/h. To highlight spatial variations of the oxidation state, separate measurements were taken at the rod centre and at the edge. Spectra before and after Ar sputtering were also recorded, because O 1*s* spectra (Fig. S11) evidenced the presence of additional bands around 932 eV in

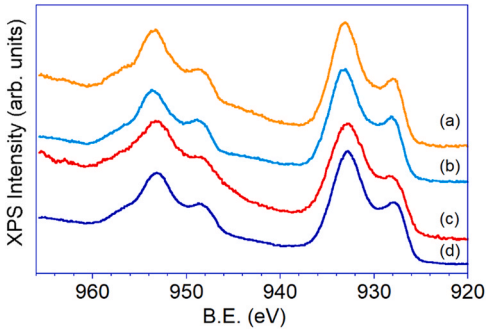

Fig. 6. XPS Pr3d spectra of PZO samples processed in air at 300 mm/h at the rod centre (a, b) and at the edge (c, d), before (a, c) and after (b, d) Ar sputtering. Spectra have been scaled for presentation purposes.

the as-prepared samples, elsewhere assigned to surface OH^- entities [17]. Binding energies (BE) were corrected according to the position of the C 1 *s* band.

Spectra in the Pr 3*d* region display the usual $3d_{3/2}$ and $3d_{5/2}$ spin-orbit-split groups of bands around 950 and 930 eV, respectively. Each group, in turn, is split into components arising from quasi-degenerate final states [16,17]. Two such components ($3\underline{d}4f^2$ and $3\underline{d}4f^3\underline{L}$) are observed for Pr^{3+} and three ($3\underline{d}4f^1$, $3\underline{d}4f^2\underline{L}$ and $3\underline{d}4f^3\underline{L}^2$) for Pr^{4+}, where $\underline{d}$ and $\underline{L}$ represent a hole in a 3*d* electronic state or in the ligand oxygen 2*p* band, respectively. Detecting Pr^{4+} relies on the weak $3\underline{d}4f^1$ components at ~946 and 966 eV [8,16,17]. Identifying those bands is difficult, however, because they overlap with other more intense bands, and depends to a great extent on the details of background subtraction, so that this procedure is only reliable for samples with a relatively high Pr^{4+} content.

To quantify the oxidation degree, data were analysed following the indications of Ref. 17, where the percentage of Pr^{4+} ions is related to the integrated intensity ratio between the band at ~946 eV and the main $3d_{5/2}$ band around 933 eV through the expression $[Pr^{4+}]/[Pr] = 3.57\ ^*I(946)/I(933)$. The intensity of the component at ~930 eV was included in the denominator, together with the main band at ~933 eV. Spectra were fitted with the help of CASA-XPS software; a Shirley-type background was subtracted and some constraints on band positions and linewidths were imposed. Examples of the fitting are given in Fig. S12. As expected, the Pr^{4+} content is lower at the sample centre (~20%) than at the rod edge (41%). Upon sputtering with Ar the OH^-–like band lowered remarkably (Fig. S11) and the Pr^{4+} decreased to 13 ± 1%, which may be ascribed to surface cleaning and to a reductive effect of Ar sputtering, respectively [17]. In summary, XPS measurements confirm the magnetic susceptibility results as regards the oxidation degree, at least for the most oxidised PZO sample.

3.5. Raman spectroscopy and oxygen stoichiometry

Raman scattering is a powerful technique for the analysis of structural anomalies in defective oxides. Compared to XRD and magnetic susceptibility, it has the advantage of providing compositional and structural information at a length scale of a few microns. Raman spectroscopy is particularly suitable to study pyrochlore–like compounds, which are prone to features such as oxygen non–-stoichiometry, cation–antisite defects and short–range–ordered domains [18]. $Pr_{2\pm x}Zr_{2\mp x}O_{7\pm y}$ compounds present the peculiarity that they may also present Pr mixed–valence effects.

The cubic pyrochlore structure of $A_2B_2O_7$ compounds (space group $Fd\bar{3}m$) can be considered a superstructure of the fluorite one with ordered cation and anion sites [19]. In a pyrochlore, cation *A* is 8–coordinated and occupies the 16*d* Wyckoff site (origin taken at *B*) while cation *B* is 6–coordinated and lays at the 16*c* site. Oxygen atoms occupy two different sites, 48*f* (O(1)) and 8*b* (O(2)), which are tetrahedrally coordinated by two *B* and two *A* cations and by four *A* cations, respectively. There is a third, unoccupied anion site, (8*a*), which is tetrahedrally coordinated to four *B* cations. The 8*a* site may be partially occupied in defect pyrochlores, either because of cation disorder or nonstoichiometry. The O(1) coordinates are (x, 1/8, 1/8), x being an indicator of how much the structure departures from the fluorite one and of the distortion at the *B* site; for $x = 0.375$ the O(1) oxygen ions occupy the fluorite–like sites, forming, together with the two 8*a* vacancies, a cube around and the *B* cation. At the other end, for $x = 0.3125$ the six O(1) around the *B* cation form a regular octahedron.

Six Raman active modes (A_{1g}, E_g, $4T_{2g}$) are expected in $A_2B_2O_7$ pyrochlores, with contribution of oxygen ions at both 48*f* ($A_{1g} + E_g + 3T_{2g}$) and 8*b* (T_{2g}) sites. *A* and *B* cations do not participate in Raman active modes, because they occupy centrosymmetric sites. Other bands are usually found in the Raman spectra of pyrochlore compounds, arising from second–order excitations, disorder effects or crystal–field transitions (see Ref. 18 and references therein).

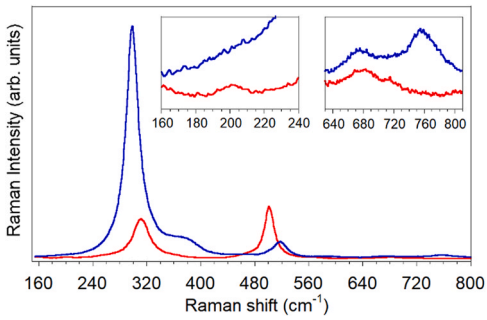

Fig. 7. Raman spectrum of $Pr_2Zr_2O_7$ single crystals at RT in *xx* (red) and *xy* (blue) configurations, where *x*, *y* stand for two perpendicular < 100 > cubic axes. The right inset displays magnified spectra to highlight a weak T_{2g} component at ~756 cm^{-1} and the left inset evidences a weak band at 200 cm^{-1} tentatively assigned to Pr^{3+} off–-centre displacements. The unpolarised band around 680 cm^{-1} is assigned to a Pr^{3+} crystal field transition.

To ease the discussion of the Raman spectra of $Pr_{2\pm x}Zr_{2\mp x}O_{7\pm y}$ compounds, we first analyse the spectrum of the stoichiometric $Pr_2Zr_2O_7$ pyrochlore. EBSD measurements (Fig. S13) show that solidification takes place along a < 100 > –like direction so that the transverse section presents a {001} plane. In such a plane, and taking *x* and *y* along two orthogonal < 100 > directions, we expect to see $A_{1g} + E_g$ modes in *xx* and T_{2g} modes in *xy* configurations. Experimental spectra (Fig. 7) yield A_{1g} and E_g modes at 501 and 312 cm^{-1}, respectively. Regarding the T_{2g} modes, three of them are clearly identified at 298, 375 and 518 cm^{-1}. The fourth T_{2g} mode of pyrochlores is controversial and has usually been ascribed either to low frequency bands around 180 cm^{-1}, as in titanates, or to a band developing at ~600 cm^{-1} in disordered pyrochlores, as in zirconates and hafnates of heavy rare earths. None of these attributions, however, agrees with recent ab–initio lattice dynamic calculations [20,21,22], which find the fourth T_{2g} at high wavenumbers (> 700 cm^{-1}), depending steeply on the *B* cation. For Zr pyrochlores it is expected around 750 cm^{-1} (Ref. 21) and in fact a close–up look at the *xy* spectrum (right inset in Fig. 7) unveils a band at 756 cm^{-1} with the correct polarisation and wavenumber that we ascribe to the fourth T_{2g} mode. We note that the band appearing at 600 cm^{-1} in disordered pyrochlores has been recently attributed to the vibration of interstitial oxygen ions occupying the 8*a* vacancy site [23,18].

Another interesting finding is the presence of a weak band around 200 cm^{-1} (left inset of Fig. 7), which cannot be attributed to an allowed mode and is neither coincident with crystal field transitions within the Pr^{3+} electronic states [24]. We propose as a likely origin of that band the presence of local Pr disorder, which would activate formally forbidden modes. Distortions in the rare–earth sublattice, either in the form of *A* atom off–centring or O(2)A_4 tetrahedra tilts, have been proposed to explain a series of X–ray, electron and neutron diffraction data of $La_2Zr_2O_7$ and $Pr_2Zr_2O_7$, and would be a means of relieving the too–short rare–earth–O(2) bond distances [12,25,26] The observation of similar bands in titanate pyrochlores has also been attributed to nominally forbidden T_{1u} modes activated by displacive disorder of the rare earth and O(2) sites [20]. Other weak features can be assigned either to second–order excitations or to crystal field transitions (CFT) between the electronic states of the $^3H_4$ ground–state multiplet of Pr^{3+} ions, in agreement with the recent identification of CFT at 77, 444, 662, 761 and 879 cm^{-1} in the Raman spectrum of PZO at 14 K (see for instance the band around 680 cm^{-1} in Fig. 7) [24]. It is interesting that off–site displacements have also been proposed in Ref. 24 to explain the split aspect of the CFT to the first excited A_{1g} state below ~150 K.

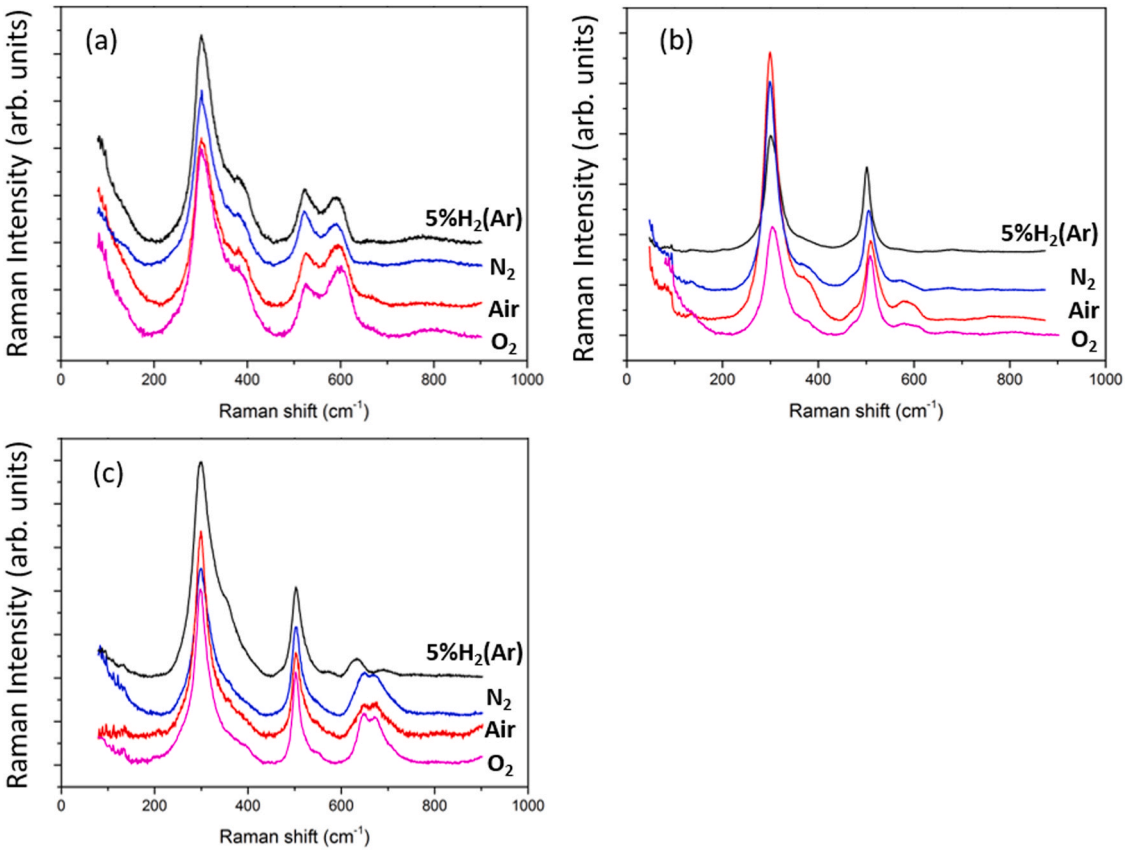

Fig. 8. Raman spectra of P1.70 (a), PZO (b), and P2.24 (c) samples processed in different atmospheres.

The two intense bands around 300 and 500 cm^{-1} are the fingerprints of the pyrochlore spectrum. The former includes contributions from the E_g mode and the first T_{2g} mode, both attributed to O(1)–*B*–O(1) bond bending [20]. The latter is assigned to the A_{1g} mode, and involves the modulation of the x_{48f} coordinate through the vibration of O(1) along the < 100 > cubic axes. The A_{1g} mode is thus sensitive to disorder effects through their influence on the environment of the *B* cation and variations of the x_{48f} parameter.

Fig. 8 shows the spectra of $Pr_{2\pm x}Zr_{2\mp x}O_{7\pm y}$ compounds as a function of composition and processing atmosphere, measured in parallel configuration along an arbitrary direction. Table 4 collects the Raman shifts of the allowed modes as a function of the composition and processing atmosphere, obtained from spectra decomposition as a sum of pseudo–Voigt profiles. Depending on the composition, additional features are observed that can be related to differences in the cation/anion stoichiometry or Pr oxidation state.

Table 4
Wavenumbers (cm^{-1}) of Raman active modes of P1.70, PZO and P2.24 samples. The experimental error is ± 1 cm^{-1}. H_2 stands for 5%H_2(Ar) atmosphere.

Sample	Atmosphere	T_{2g} (1)	E_g	T_{2g} (2)	A_{1g}	T_{2g} (3)	T_{2g} (4)
P1.70	H_2	300	323	383	523	543	
	N_2	300	320	386	522	542	
	Air	300	326	387	524	547	
	O_2	300	322	387	524	547	
PZO	H_2	299	312	375	501	518	757
	N_2	299	312	373	504	518	756
	Air	299	322	374	507	520	755
	O_2	299	317	377	505	520	
P2.24	H_2	298	324	353	503	518	755
	N_2	297	315	346	502	518	760
	Air	299	318	350	502	515	
	O_2	297	317	352	502	520	

The most noticeable feature of the spectra of P1.70 samples is the high intensity of the band at 600 cm^{-1}, regardless of the processing atmosphere. The activation of a band at that wavenumber in zirconate pyrochlores has been consistently attributed to the vibration of oxygen ions occupying the 8*a* vacant site [18,23] owing to disorder effects or non–stoichiometry. In the present case the population of the 8*a* site is required to balance out the positive charge excess arising both from the Zr^{4+} enrichment as from the presence of Pr^{4+} ions. The enhancement of the band in samples processed in oxidising atmospheres indicates a higher vacancy population, which might be attributed either to a higher Pr^{4+} proportion, in agreement with magnetic susceptibility results, or to an increase of Zr^{4+} content, because of the stronger Pr volatilisation in oxidising atmosphere. To work out the relative relevance of each of these factors we can make some numbers using the PMR derived from EDX analysis and the Pr^{4+} content deduced from magnetic susceptibility. Then, for the P1.70 sample processed in O_2, with PMR ~0.420, the stoichiometry would be $Pr_{1.68}Zr_{2.32}O_{7.16}$ in the absence of Pr oxidation, and the presence of a 16.5% of Pr^{4+} ions (0.28 per formula unit (pfu)) would imply additional 0.14 oxygen ions pfu, resulting in 0.16 + 0.14 = 0.30 total oxygen excess pfu. For the sample processed in 5%H_2(Ar) the PMR of 0.446 would give $Pr_{1.78}Zr_{2.22}O_{7.11}$ stoichiometry to which a 10% of Pr^{4+} ions (0.18 pfu) would add 0.09 oxygen atoms pfu, resulting in 0.11 + 0.09 = 0.20 total oxygen excess. Then, the ratio of expected oxygen excess (occupancy of the 8a site) between the samples processed in O_2 and in 5%H_2(Ar) is of about 1.5, which is quite close to the intensity ratio of the 600 cm^{-1} band in the corresponding Raman spectra. We thus see that i) both Pr volatilisation and Pr oxidation give comparable contributions to oxygen stoichiometry, and ii) vacancy population at the 8a site is the most likely compensation factor for Pr–poor compositions.

In PZO samples processed at 300 mm/h, the 600 cm^{-1} band is present but with weak intensity. The band appears highest for the sample processed in air. As that sample had PMR very close to 0.5, we attribute the band mainly to its high Pr^{4+} content (Fig. 8b). It is however striking that the band is very weak in the sample processed in 5%H_2(Ar), despite magnetic susceptibility yields an appreciable 24% proportion of Pr^{4+} ions. We note that the average PMR of that sample is ~0.51 and EDX showed the presence of grains with bright grain–boundaries presenting high Pr and O content. The latter are considered to be the origin of the high Pr^{4+} average content. Their inhomogeneous composition and probably bad crystallization impede to detect their Raman spectra, as occurred in X–ray diffraction. Then, the Raman spectrum shown in Fig. 8 has to be considered as representative of the more reduced, nearly stoichiometric regions.

The 600 cm^{-1} band is absent in Pr–rich P2.24 samples, suggesting that the vacancies are not or scarcely populated. This agrees with our hypothesis that in Pr–rich pyrochlores most of the Pr^{4+} ions just substitute for Zr^{4+} with no need of extra oxygen for charge compensation. However, other high–frequency bands appear in these spectra. For samples processed in air, O_2 or N_2, the high–frequency band extends from 600 to 700 cm^{-1}, and is clearly composed of at least two sub–bands at ~650 and ~670 cm^{-1}. We propose that this band is related to the large size of the Pr^{4+} ions at the octahedral sites, which induces an outward oxygen shift from the central Pr^{4+} ion resulting in shorter Zr–O bonds for nearby Zr ions.

The case of the P2.24 sample processed in 5%H_2(Ar) is interesting. At the rod centre (Fig. 8c) the spectrum displays two high frequency bands at ~630 and ~700 cm^{-1}, whereas at the rod edge the spectrum is similar to that of samples processed in the other atmospheres (Fig. S14 of supporting information). We note that according to magnetic measurements the Pr^{4+} content of that sample is ~13%, but this is an average over the central, reduced region with green colour and the brown, oxidised outer edge, and includes also the contribution from the grain boundaries. For charge neutrality and $Pr_{2.24}Zr_{1.76}O_7$ stoichiometry the Pr^{4+} content should amount to 0.24 ions pfu, i.e. 10.7% with respect to the total Pr content, whereas total Pr reduction implies an oxygen–defective $Pr_{2.24}Zr_{1.76}O_{6.88}$ pyrochlore with ~0.24 Pr^{3+} ions at the B site. We note that oxygen vacancies are proposed as the charge–balance factor of Pr–rich compositions in Ref. [9]. Then, the reduced central region of P2.24 samples processed in 5%H_2(Ar) is expected to present oxygen vacancies additional to the 8*a* ones. Since it is highly unlikely that Pr^{3+} or Zr^{4+} ions at the *B* site adopt a CN lower than 6, charge compensating vacancies may be created at the 8*b* sites. We would then find three types of Pr^{3+} environments: a majority at *A* sites with the usual 2 O(2) + 6 O(1) coordination, a small amount at *A* sites but with O(2) + 6 O(1) coordination, and those at the *B* site, coordinated with 6 O(1). The different oxygen rearrangement in these disordered configurations would explain the different high frequency bands observed in reduced P2.24 samples compared to the oxidised ones.

Fig. 9 displays Raman shifts of the allowed modes as a function of the lattice parameter. Although the A_{1g} wavenumber decreases with increasing lattice parameter (increasing Pr content), the relation is far from linear. Irrespective of the processing atmosphere, a strong decrease of the A_{1g} wavenumber is observed between P1.70 and PZO compositions, remaining approximately constant for PMR > 0.5. A similar trend is observed for the $T_{2g}(3)$ mode. All other modes present a smooth quasi–linear dependence. The evolution of the A_{1g} and $T_{2g}(3)$ modes is somewhat surprising, because the BO_6 octahedron is expected to remain more or less invariant as far as the *B* cation is Zr^{4+} (for PMR ≤ 0.5) and become expanded, on the average, for Pr rich compositions. The clue resides in the nature of the A_{1g} and $T_{2g}(3)$ modes themselves. We remind that, by symmetry, the A_{1g} mode consists of the vibration of the O(1) ions along the < 100 > directions toward the 8*a* vacancies and involves mainly O–O force constants, thus being very sensitive to the occupancy of the vacancy

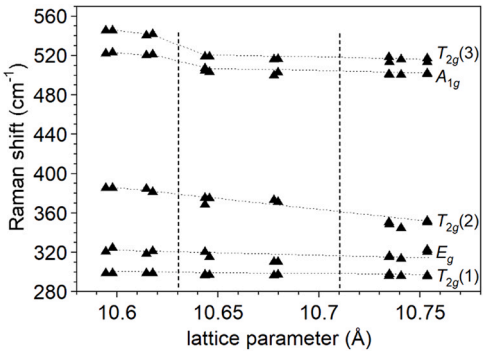

Fig. 9. Evolution of the Raman shifts of the allowed modes in the 300–550 cm^{-1} region as a function of the lattice parameter. The fourth T_{2g} mode is observed between 750 and 760 cm^{-1}. Dashed vertical lines separate data from P1.70, PZO and P2.24 samples.

sites [20]. To compensate for Zr excess, vacancies are partially populated in P1.70 compositions, which results in stronger O–O force constants and harder A_{1g} modes. Thus, the decrease of the A_{1g} wavenumber with increasing Pr content is assigned not only to lattice expansion but also to the progressive reduction of the 8*a* occupancy. Once the charge excess producing that occupancy disappears the mode frequency remains more or less constant. A similar argument explains the evolution of the $T_{2g}(3)$ modes [20–22].

Paying attention to the processing atmosphere, we can realize that for the same nominal composition samples processed in oxidising atmospheres (O_2 and air) exhibit higher Raman shifts than samples processed in N_2 or H_2, which may be attributed to the stronger volatilisation of Pr oxides in oxidising atmospheres and the resulting decrease of lattice parameter.

4. Discussion

We have performed a systematic analysis of the phases formed in the ZrO_2–PrO_x system upon melting and resolidification for compositions nominally within the pyrochlore solid–solution field, according to the published PD [10,11]. The LFZ technique has been used so as to reach the high temperatures required to melt these oxides. Four different atmospheres have been used, varying the processing conditions from oxidising to reducing.

The present results show that a close correlation exists between composition and microstructure. Two different behaviours are found, as regards phase homogeneity and microstructure, depending on whether the oxide composition is Pr–poor (PMR < 0.5) or Pr–rich (PMR > 0.5). For P1.70 compounds, homogenous microstructure and phase content are found with only smooth fluctuations of Pr rate in different areas of the sample. Raman spectroscopy suggests that occupancy of the vacancy sites (8*a*) by oxide ions is the predominant charge compensation mechanism for the excess Zr^{4+} ions, as evidenced by the detection of a band 600 cm^{-1}, consistently attributed to the vacancy population [18,23]. Oxygen located at the 8*a* site results in local Zr–O_7 coordination, which is a very stable configuration for Zr^{4+} cations. A low but non negligible Pr^{4+} content is found in these samples, even for those processed in reducing conditions. All the Pr^{4+} ions, however, can be reduced to Pr^{3+} by post–preparation thermal treatment in a vacuum. Small variations of the Pr oxidation state have little effect in the Raman spectra, except for changes in the relative amount of the 600 cm^{-1} band. A similar behaviour, as regards phase homogeneity and microstructural aspect, is observed around PMR = 0.5 (PZO samples) when there is a small Pr deficiency.

On the contrary, for PMR > 0.5 (both for P2.24 compositions as for PZO with slight Pr excess) the sample breaks into quasi–hexagonal grains composed of a pyrochlore–like phase at the grain

centre, with PMR ≤ 0.56, and a very defective and oxidised Pr–rich phase at the grain boundaries. Such a behaviour can be explained by the characteristics of the PD at the high solidification temperatures present in these experiments [10,11]. Despite pyrochlore phase admits some Pr excess, with limiting PMR = 0.56 below ~1600 °C, at high temperatures the pyrochlore solid–solution field narrows and no pyrochlore phase is stable with such composition [10,11]. Instead, separation between a Pr–poor pyrochlore phase and a Pr–rich liquid occurs, resulting in the solidification of quasi–hexagonal grains with Pr–rich grain boundaries arising from the segregated liquid. Raman scattering has provided useful information about oxygen content and location in Pr–rich samples. Two types of spectra are found, depending on the processing atmosphere: in samples processed in O_2, air or N_2 the Raman spectrum presents additional high frequency bands (but not the one at 600 cm^{-1}), which are attributed to oxygen shifts away from the Pr^{4+} ions occupying the B site, because of the larger size of this cation compared to Zr^{4+}, thus resulting in shorter Zr–O bonds with nearby Zr^{4+} ions. In contrast, the P2.24 sample processed in 5%H_2(Ar) displays a noticeable difference between spectra recorded at the rod centre (green colour, fully reduced) and at the outer region (brown colour, partially oxidised). Extra high frequency bands are observed in both cases, but at different wavenumbers. In the outer regions the spectrum is similar to that found in samples processed in oxidising atmospheres, whereas the bands found in the reduced regions are attributed to vacancies created at the 8*b* sites, to preserve at least a six–fold coordination around the Pr^{3+} ions located at the octahedral site. The radial distribution of oxygen content with enrichment toward the rod edge is attributed to incomplete outward oxygen diffusion.

As regards the variation of the Pr oxidation state, it is interesting to see that a small range of valence fluctuation is found for P1.70 and P2.24 compositions when comparing samples processed in different atmospheres, which suggests that oxygen diffusion is fast enough to release most of the oxygen excess present in the feedstock. We note that the remanence of some Pr^{4+} ions is favoured in the P2.24 compositions to avoid the creation of oxygen vacancies, but the obtained proportion of Pr^{4+} is in general higher than required for charge neutrality. Taking into account that, according to Raman spectra, no population of 8*a* sites occurs in P2.24 samples, we conclude that the excess Pr^{4+} ions are not located in pyrochlore phases but in the Pr–rich oxidised grain boundaries. The high Pr^{4+} content of the PZO composition processed in H_2 can also be understood on the same grounds, as illustrated by the difference between the samples processed at 300 and 100 mm/h: the former, presenting a Pr^{4+} relative content > 20%, had a small Pr excess and broke into grains with oxidised grain boundaries holding the Pr^{4+} ions. On the contrary, the green sample grown at 100 mm/h, with no Pr^{4+} at all, was almost exactly stoichiometric and had a very homogenous aspect with no grain segregation.

We have seen that for PMR = 0.5 and slow solidification in reducing atmosphere a stoichiometric $Pr_2Zr_2O_7$ pyrochlore is obtained. Completely reduced phases can be also obtained from P1.70 and other PZO samples by a post–synthesis annealing in reducing atmosphere or a vacuum. On the contrary, no reduction took place in Pr–rich P2.24 compositions previously containing Pr^{4+} ions, which is attributed to the high stability of the excess Pr ions at the *B* pyrochlore site in the Pr^{4+} state and the difficulty of extracting oxygen.

The present results evidence that the solidified phases depend on several factors, besides the nominal stoichiometry and processing atmosphere. First of all, it is clear that the initial oxidation state of the Pr_6O_{11} reagent is relevant for the final oxygen stoichiometry: despite the tendency of Pr to become reduced at high temperatures, kinetic factors preclude total evolution of oxygen excess and most samples remain, on the average, more oxidised than expected from nominal stoichiometry. This is especially noticeable for Pr–rich samples, whose microstructure consists of juxtaposed quasi–hexagonal grains. The physical separation between grains hampers oxygen evolution out of the grains, thus resulting in a high Pr oxidation state in the grain boundaries. A second aspect is that Pr volatilisation reduces the Pr content, especially for oxidising atmospheres, this being a function of the solidification rate: the faster the growth, the lower the volatilisation. Kinetic factors also explain the Pr content fluctuations for a given sample detected by EDX in otherwise homogenous samples and the presence of broad XRD peaks denoting a distribution of lattice parameters.

The oxygen and Pr^{4+} content pfu as well as their radial distribution are directly related to oxygen diffusivity, which is expected to vary as a function of temperature and composition. No clear conclusion has been obtained concerning this point, except for the optical evidence of darker regions (Pr^{4+}–rich) close to the edge in samples processed in reducing atmosphere and a more uniform colouration for samples processed in oxidising atmosphere, for the same solidification rate of 300 mm/h, suggesting that oxygen diffusion and release are competitive and of similar time scales. It has been reported that faster oxygen uptakes are achieved as the Pr content increases in fluorite–like ZrO_2–PrO_x mixed oxides [8]. For pyrochlore–like compositions, the oxide ion conductivity in air has been reported to vary non–monotonically as a function of Pr content, with a minimum for the 50/50 composition [9,27]. A double mechanism of oxygen diffusion in non–stoichiometric pyrochlores has been proposed, by oxygen interstitials and by vacancies, according to whether there is Pr deficiency or Pr excess, respectively [27]. In contrast, very high conductivity is found for the fluorite compound Pr_3ZrO_{7+x}, which includes a relevant proportion of electronic contribution [9,27]. In fact, differences between fluorite–like and pyrochlore–like compounds are to be expected, as regards oxygen ion conductivity. In the first case, oxygen vacancies are created in the fluorite lattice to compensate for the presence of Pr^{3+} ions. The random vacancy distribution favours oxygen conductivity, the effect increasing for intermediate Pr valence. On the contrary, in the pyrochlore lattice the ordered stoichiometric vacancies are not a source of high conductivity, which rather resides in the 48*f* sublattice [28]. Appreciable conductivity in pyrochlore compounds appears only in the case of deep cation and anion disorder (as in $Gd_2Zr_2O_7$) or if there is cation non–stoichiometry, with either rare–earth excess or deficiency, as reported in Ref. [27]. We have seen that the occupancy of the 8*a* site is the mechanism for charge compensation in our Pr–poor compounds, in which case the conduction through oxygen interstitials would apply. On the other hand, except for the sample grown in 5%H_2(Ar), our P2.24 samples contain an appreciable amount of Pr^{4+} ions, presumably at the B site, so that the lattice contains no additional vacancies other than the 8*a* ones. However, in those cases Raman measurements suggested that remarkable oxygen displacements occur around the large Pr^{4+} at *B* site, which might also enable disorder–enhanced oxygen diffusion. Pr–rich compositions belong to the "stuffed–pyrochlore" compounds where local anion disorder around the excess cations are proposed to explain their high conductivity [29]. It is clear that both Pr–rich and Pr–poor compounds have a greater cation and anion disorder than stoichiometric PZO pyrochlores, which probably explains their higher ability to release oxygen excess at high temperatures.

Finally, we would like to comment on the differences between the phases formed in the ZrO_2–CeO_x and ZrO_2–PrO_x systems processed by the LFZ technique for intermediate compositions. In the ZrO_2–CeO_x system no stable intermediate phase exists except in the fully reduced case, when the $Ce_2Zr_2O_7$ pyrochlore forms. When processing in air, a defect fluorite with cation disorder and high Ce^{4+} content is formed, yielding the well–known *t'* phase upon moderate–temperature oxidation [23,30]. When processing in reducing conditions the ordered pyrochlore $Ce_2Zr_2O_7$ is obtained, which may also be oxidised at moderate temperatures to successive metastable $Ce_2Zr_2O_{7+\delta}$ forms up to the known 2–2–8 kappa–phase, without

changing the ordered cation distribution [23,31,32]. As the trivalent oxidation state is much more stable for Pr than for Ce, no equivalent of the defect–fluorite or *t'*–phase exists in the ZrO_2–PrO_x system for intermediate compositions and a pyrochlore is always formed, even in air. For the same reason, no remarkable oxidation of the $Pr_2Zr_2O_7$ pyrochlore is feasible so that no equivalent of the kappa phase exists. The higher stability against oxidation of $Pr_2Zr_2O_7$ and its lower oxygen conductivity explain that the ZrO_2–PrO_x compositions presenting the best OSC properties are not around 50 mol% of the phase diagram, contrary to the ZrO_2–CeO_x case.

5. Summary and conclusions

We have produced crystalline samples of composition $Pr_{2\pm x}Zr_{2\mp x}O_{7\pm y}$ by laser–assisted solidification in O_2, air, N_2 and 5% H_2(Ar) atmospheres. Sample colouration changed from bright green to dark brown, owing to varying Pr^{4+} content. The most relevant result is that a close correlation exists between the phase homogeneity, the microstructure and the Pr content. For Pr molar rate (PMR) < 0.5 the samples present a homogeneous aspect, whereas Pr–rich compositions (PMR > 0.5) always break into 10–20 μm–sized grains with pyrochlore phases at the grain centre and ill–crystallised, Pr–rich oxidised phases at the grain–boundaries, coming from the segregation of Pr–rich liquid prior to solidification. Small compositional fluctuations of the pyrochlore phases are evidenced in EDX and XRD measurements, arising both from some inhomogeneity of the Pr content as of its oxidation state. An almost linear relation between lattice parameter and Pr content is found, as expected, with variations for fixed composition being attributed to differences in the Pr oxidation state.

All samples are mainly pyrochlore–like but present different types of oxygen disorder depending on composition and processing atmosphere: in Pr–poor the 8*a* vacancy is partially populated, resulting in local ZrO_7 coordination, whereas in Pr–rich samples oxygen disorder occurs around the Pr^{3+} or Pr^{4+} ions substituting for Zr^{4+}, because of size–mismatch. Magnetic measurements and XPS showed a higher–than expected Pr^{4+} content, which has been attributed to several factors: the highly oxidised state of the feedstock material, the segregation of Pr and O–rich grain boundaries in compositions with PMR > 0.5, and the lower oxide ion conductivity for PZO compositions, compared to either Pr–poor or Pr–rich compositions.

Varying the processing atmosphere affects both the cation and anion stoichiometries. Cation composition is altered because of Pr volatilisation at high temperatures, which is enhanced in oxidising atmosphere. Anion non-stoichiometry in the form of oxygen excess results from Pr oxidation, which is also favoured in oxidising atmospheres.

Credit authorship contribution statement

All the authors contributed equally to performing experimental work, data interpretation and discussion.

Data Availability

Data will be made available on request.

Declaration of Competing Interest

The authors declare that they have no known competing financial interests or personal relationships that could have appeared to influence the work reported in this paper.

Acknowledgments

We acknowledge financial support from the Spanish Government and Feder Funds (European Union) through projects MAT2016-77769R and PID2019-107106RB-C32. LG acknowledges the grant BES-2017-079683. We acknowledge the General Research Support Service of the University of Zaragoza for technical assistance in the X–ray diffraction, magnetic susceptibility and electron–microscopy measurements, and the Laboratorio de Microscopías Avanzadas (LMA) of the University of Zaragoza for technical assistance in XPS measurements.

Appendix A. Supporting information

Supplementary data associated with this article can be found in the online version at doi:10.1016/j.jallcom.2022.166449.

References

[1] Catalysis by Ceria and Related Materials, 2nd Edition, Catalytic Science Series, vol. 12, edited by Alessandro Trovarelli and Paolo Fornasiero, London: Imperial College Press, 2013.
[2] E.S. Putna, J.M. Vohs, R.J. Gorte, G.W. Graham, An examination of praseodymia as an oxygen–storage component in three–way catalysts, Catal. Lett. 54 (1998) 17–21.
[3] A.D. Logan, M. Shelef, Oxygen availability in mixed cerium/ praseodymium oxides and the effect of noble metals, J. Mater. Res. 9 (1994) 468–475.
[4] C.K. Narula, L.P. Haack, W. Chun, H.–W. Jen, G.W. Graham, Single–phase PrO_y–ZrO_2 materials and their oxygen storage capacity: a comparison with single–phase CeO_2–ZrO_2, PrO_y–CeO_2, and PrO_y–CeO_2–ZrO_2, Mater. J. Phys. Chem. B 103 (1999) 3634–3639.
[5] H. He, H.X. Dai, C.T. Au, Defective structure, oxygen mobility, oxygen storage capacity, and redox properties of RE–based (RE = Ce, Pr) solid solutions, Catal. Today 90 (2004) 245–254.
[6] J. Abel, M. Lamirand–Majimel, J. Majimel, V. Bellière–Baca, V. Harlé, G. André, C. Prestipino, S. Figueroa, E. Durand, A. Demourges, Oxygen non–stoichiometry phenomena in $Pr_{1-x}Zr_xO_{2-y}$ compounds ($0.02 < x < 0.5$), Dalton Trans. 43 (2014) 15183–15191.
[7] M.B. Bellakki, C. Shivakumara, T. Baidya, A.S. Prakash, N.Y. Vasanthacharya, M.S. Hegde, Synthesis, structure and oxygen–storage capacity of $Pr_{1-x}Zr_xO_{2-\delta}$ and $Pr_{1-x-y}Pd_yZr_xO_{2-\delta}$, Mater. Res. Bull. 43 (2008) 2658–2667.
[8] M.Y. Sinev, G.W. Graham, L.P. Haack, M. Shelef, Kinetic and structural studies of oxygen availability of the mixed oxides $Pr_{1-x}M_xO_y$ (M = Ce, Zr), J. Mater. Res. 11 (1996) 1960–1971.
[9] A.V. Shlyakhtina, J.C.C. Abrantes, E. Gomes, A.N. Shchegolikhin, G.A. Vorobieva, K.I. Maslakov, A.V. Knotko, L.G. Shcherbakova, Effect of Pr^{3+}/Pr^{4+} ratio on the oxygen ion transport and thermomechanical properties of the pyrochlore and fluorite phases in the ZrO_2–Pr_2O_3 system, Int. J. Hydrog. Energ. 41 (2016) 9982–9992.
[10] M.D. Krasil'nikov, I.V. Vinokurov, S.D. Nikitina, Physicochemical properties of solid solutions in the zirconium dioxide–praseodymium oxide system in air; in Fiz. Khim. Elektrokhim. Rasplavl. Tverd. Elektrolitov, Tezisy Dokl. Vses. Konf. Fiz. Khim. Ionnykh Rasplavov Tverd. Elektrolitov, 7th, Sverdlovsk, USSR, September 18–20, 1979, Vol. 3, pp. 123–125. Akademiya Nauk SSSR, Ural'skii Nauchnyi Tsentr, Ekaterinburg, USSR, 1979.
[11] A. Rouanet, Contribution à l'etude des systèmes zirconia—oxydes des lanthanides au voisinage de la fusion: Memoire de thèse, Rev. Intern. Hautes Temper. Refract. 8 (1971) 161–180.
[12] S.M. Koohpayeh, J.-J. Wen, B.A. Trump, C.L. Broholm, T.M. McQueen, Synthesis, floating zone crystal growth and characterization of the quantum spin ice $Pr_2Zr_2O_7$ pyrochlore, J. Cryst. Growth 402 (2014) 291–298.
[13] M.C. Hatnean, C. Decorse, M.R. Lees, O.A. Petrenko, G. Balakrishnan, Zirconate pyrochlore frustrated magnets: crystal growth by the floating zone technique, Crystals 6 (2016) 79.
[14] J. Rodriguez-Carvajal, FULLPROF: A Program for Rietveld Refinement and Pattern Matching Analysis, Abstracts of the Satellite Meeting on Powder Diffraction of the XV Congress of the IUCr, p. 127, Toulouse, France (1990).
[15] J.H. Van Vleck, A. Frank, The effect of second order Zeeman terms on magnetic susceptibilities in the rare earth and iron groups, Phys. Rev. 34 (1929) 1494–1496.
[16] A. Bianconi, A. Kotani, K. Okada, R. Giorgi, A. Gargano, A. Marcelli, T. Miyahara, Many-body effects in praseodymium core-level spectroscopies of PrO_2, Phys. Rev. B 38 (1988) 3433–3437.
[17] H. Borchert, Y.V. Frolova, V.V. Kaichev, I.P. Prosvirin, G.M. Alikina, A.I. Lukashevich, V.I. Zaikovskii, E.M. Moroz, S.N. Trukhan, V.P. Ivanov, E.A. Paukshtis, V.I. Bukhtiyarov, V.A. Sadykov, Electronic and chemical properties of nanostructured cerium dioxide doped with praseodymium, J. Phys. Chem. B 109 (2005) 5728–5738.
[18] M.L. Sanjuán, Raman spectroscopy study of disorder phenomena and size effects in pyrochlores, in Pyrochlore Ceramics: Properties, Processing and Applications,

edited by Anirban Chowdhury, Elsevier Series on Advanced Ceramic Materials, Elsevier, 2022, ISBN 9780323904834.
[19] M.A. Subramanian, G. Aravamudan, G.V. Subba Rao, Oxide pyrochlores – a review, Prog. Solid State Chem. 15 (1983) 55–143.
[20] S. Kumar, H.C. Gupta, First principles study of zone centre phonons in rare–earth pyrochlore titanates, $RE_2Ti_2O_7$ (RE = Gd, Dy, Ho, Er, Lu; Y), Vib. Spectrosc. 62 (2012) 180–187.
[21] V.A. Chernyshev, Phonon spectrum of $La_2Zr_2O_7$: ab initio calculation, Opt. Spectrosc. 127 (2019) 825–831.
[22] M. Ruminy, M. Núñez Valdez, B. Wehinger, A. Bosak, D.T. Adroja, U. Stuhr, K. Iida, K. Kamazawa, E. Pomjakushina, D. Prabakharan, M.K. Haas, L. Bovo, D. Sheptyakov, A. Cervellino, R.J. Cava, M. Kenzelmann, N.A. Spaldin, T. Fennell, First–principles calculation and experimental investigation of lattice dynamics in the rare–earth pyrochlores $R_2Ti_2O_7$ (R = Tb, Dy, Ho), Phys. Rev. B 93 (2016) 214308.
[23] P.B. Oliete, A. Orera, M.L. Sanjuán, Spectroscopic insight into the interplay between structural disorder and oxidation degree in melt–grown $Ce_{0.5}Zr_{0.5}O_{2-y}$ compounds, J. Raman Spectrosc. 51 (2020) 514–527.
[24] Yuanyuan Xu, Huiyuan Man, Nan Tang, Santu Baidya, Hongbing Zhang, Satoru Nakatsuji, David Vanderbilt, Natalia Drichko, Importance of dynamic lattice effects for crystal field excitations in the quantum spin ice candidate $Pr_2Zr_2O_7$, Phys. Rev. B 104 (2021) 075125.
[25] Y. Tabira, R.L. Withers, T. Yamada, N. Ishizawa, Annular dynamical disorder of the rare earth ions in a $La_2Zr_2O_7$ pyrochlore via single crystal synchrotron X–ray diffraction, Z. Krist. 216 (2001) 92–98.
[26] B.A. Trump, S.M. Koohpayeh, K.J.T. Livi, J.-J. Wen, K.E. Arpino, Q.M. Ramasse, R. Brydson, M. Feygenson, H. Takeda, M. Takigawa, K. Kimura, S. Nakatsuji, C.L. Broholm, T.M. McQueen, Universal geometric frustration in pyrochlores, Nat. Commun. 9 (2018) 2619.
[27] D.A. Belov, A.V. Shlyakhtina, J.C.C. Abrantes, S.A. Chernyak, G.A. Gasymova, O.K. Karyagina, L.G. Shcherbakova, Electrochemical behavior of the pyrochlore– and fluorite–like solid solutions in the Pr_2O_3–ZrO_2 system. Part I, Solid State Ion. 271 (2015) 79–85.
[28] P.J. Wilde, C.R.A. Catlow, Defects and diffusion in pyrochlore structured oxides, Solid State Ion. 112 (1998) 173–183.
[29] B.G. Mullens, Z. Zhang, M. Avdeev, H.E.A. Brand, B.C.C. Cowie, M. Saura Múzquiz, B.J. Kennedy, Effect of long– and short–range disorder on the oxygen ionic conductivity of $Tm_2(Ti_{2-x}Tm_x)O_{7-x/2}$ "Stuffed" pyrochlores, Inorg. Chem. 60 (2021) 4517–4530.
[30] M. Yashima, K. Morimoto, N. Ishizawa, M. Yoshimura, Diffusionless tetragonal–cubic transformation temperature in zirconia–ceria solid solutions, J. Am. Ceram. Soc. 76 (1993) 2865–2868.
[31] T. Omata, H. Kishimoto, S. Otsuka-Yao-Matsuo, N. Ohtori, N. Umesaki, Vibrational Spectroscopic and X–Ray Diffraction Studies of Cerium Zirconium Oxides with Ce/Zr Composition Ratio=1 Prepared by Reduction and Successive Oxidation of t'–$(Ce_{0.5}Zr_{0.5})O_2$ Phase, J. Solid State Chem. 147 (1999) 573–583.
[32] S.N. Achary, S.K. Sali, N.K. Kulkarni, P.S.R. Krishna, A.B. Shinde, A.K. Tyagi, Intercalation/deintercalation of oxygen: a sequential evolution of phases in Ce_2O_3/CeO_2–ZrO_2 pyrochlores, Chem. Mater. 21 (2009) 5848–5859.

Received: 27 February 2023 | Revised: 25 May 2023 | Accepted: 9 June 2023

DOI: 10.1111/jace.19305

Journal of the American Ceramic Society

RESEARCH ARTICLE

Ceramics with eutectic microstructure in the ZrO_2–PrO_x system

Lorena Grima | **José Ignacio Peña** | **María Luisa Sanjuán**

Instituto de Nanociencia y Materiales de Aragón, Facultad de Ciencias, Universidad de Zaragoza-CSIC, Zaragoza, Spain

Correspondence
María L. Sanjuán, Instituto de Nanociencia y Materiales de Aragón (Universidad de Zaragoza-CSIC), Facultad de Ciencias, Universidad de Zaragoza, 50009 Zaragoza, Spain.
Email: sanjuan@unizar.es

Funding information
Spanish Government, Grant/Award Numbers: PID2019-107106RB-C32, PID2021-124863OB-I00, BES-2017-079683; European Union; The financial support from Gobierno de Aragón, Grant/Award Number: T02-20R group

Abstract

Praseodymium oxides present redox properties analogous to those of Ce-based systems and have been proposed for catalytic applications in combination with CeO_2, ZrO_2, or both. However, uncertainties remain concerning the nature and redox behavior of Pr-rich mixtures, especially with ZrO_2. Here we study the eutectic composites of the ZrO_2–PrO_x system, focusing on the sensitivity of their microstructure, phase symmetry, and composition to variations of the processing atmosphere from oxidizing to reducing. Mixed oxides have been produced by a laser-assisted directional solidification technique in O_2, air, N_2, or 5%H_2(Ar) environment, and the resulting materials have been analyzed by scanning electron microscopy/energy-dispersive X-ray spectroscopy, X-ray diffraction, Raman spectroscopy, and magnetic susceptibility. In air, N_2, or 5%H_2(Ar) atmosphere, a lamellar, eutectic-like microstructure forms, the major phase being the one with less Pr content. Both the Pr concentration in each phase as the PrO_x molar percentage of the eutectic composites decrease as the atmosphere becomes more reducing. Both eutectic phases are fluorite-like when processing in air, whereas in N_2 or 5%H_2(Ar), the phase with high Pr content is of the A-R_2O_3 type, and the phase with low Pr content can be described as a fluorite phase containing C-R_2O_3-like short-range-ordered regions. The results obtained for samples processed in O_2 suggest that for high enough pO_2 no eutectic forms, in analogy with the ZrO_2–CeO_2 system. The evolution of the phase composition and symmetry is discussed in terms of the limited stability of the phases found in the ZrO_2–Pr_2O_3 system, namely, A- or C-R_2O_3-like, beyond a certain Pr oxidation degree and oxygen content.

KEYWORDS
eutectic materials, laser processing, microstructure, oxidation, phase diagrams, praseodymium oxide, ZrO_2

1 | INTRODUCTION

Praseodymium oxides are receiving interest in recent times because of their redox properties, analogous to those of Ce-based systems, which make them promising for catalytic applications. Several studies have addressed the properties of PrO_x combined with CeO_2 and/or ZrO_2.[1–5] In the ZrO_2–PrO_x system, in particular, higher reducibility and lower temperatures of reduction are obtained for Pr-rich compositions (Pr/Zr > 1).[2,4,5] Despite the technological interest, the high Pr content/high-temperature region of the phase diagram is still quite uncertain, an aspect that may be related to the mixed-valence properties of Pr.[6–8] According to the early studies in the 70′s and 80′s, all ZrO_2–R_2O_3 systems (R = La to Yb) present a eutectic point in the R-rich side of the phase diagram at a molar proportion of R_2O_3 between 65 and 85 mol%.[7–9] For the ZrO_2–Pr_2O_3 system, the eutectic is found at 70 mol% Pr_2O_3 and is composed of a low Pr content phase of bixbyite C-R_2O_3 type ($Ia\bar{3}$ space group [SG]), with 62 mol% Pr_2O_3, and a high Pr content cubic phase, labeled as X phase, with 78 mol% Pr_2O_3, which is stable only near the melting point.[7] Converting molar percentages from Pr_2O_3 to $PrO_{1.5}$, the eutectic would be at 82.4 mol% $PrO_{1.5}$, with low and high Pr content phases at 76.5 and 87.6 mol% $PrO_{1.5}$, respectively. The X phase was later analyzed (in the ZrO_2–La_2O_3 and ZrO_2–Nd_2O_3 systems) by neutron diffraction and found to have $Im\bar{3}m$ SG.[10] There exists, however, discrepancy among the two reported phase diagrams[6,7] (see Figure S1a,b). Among other differences, in Ref. [6], the low Pr content phase of the eutectic is said to be a "tetragonally deformed" fluorite. We note that the PD of Ref. [6] presents a lot of undefined regions; the details of the proposed phases, beyond their symmetry, are not given, neither the oxygen partial pressure in which data were collected. The text accompanying that PD in the PD database says that "the oxygen activity is not fixed experimentally."

In any case, in the ZrO_2–PrO_x system, the mixed-valence character of praseodymium anticipates a dependence of the eutectic characteristics on the oxygen partial pressure (pO_2) of the synthesis or processing atmosphere. In fact, in the closely related ZrO_2–CeO_x system, where Ce also presents mixed-valence properties, a eutectic point exists for total Ce reduction (at ~87 mol% $CeO_{1.5}$[11]) but not in the oxidized ZrO_2–CeO_2 system.[12] In Ref. [7], Rouanet studied the effect of quenching ZrO_2–PrO_x mixtures from the melt to room temperature (RT) in air, but eutectic properties such as phase composition and lattice parameters were not analyzed. Moreover, eutectic microstructures were not described either in reducing or in oxidizing conditions. In this work, we analyze the composition, symmetry, and dependence on the processing atmosphere of the ZrO_2–PrO_x eutectic composites.

Mixed oxides have been produced by the laser-assisted directional solidification technique, also known as laser-floating zone (LFZ), which allows reaching the high melting point of these oxides and controlling the growth atmosphere during melting and cooling. The resulting materials have been characterized by scanning electron microscopy (SEM) and energy-dispersive X-ray spectroscopy (EDX) to determine the phase composition and ZrO_2–PrO_x proportion as a function of the processing atmosphere (O_2, air, N_2, or 5%H_2(Ar)), and by X-ray diffraction (XRD) and Raman spectroscopy to identify the phase symmetry. Magnetic susceptibility has been used to investigate the oxidation state of one of the samples. We find good agreement with early works for samples produced in 5%H_2(Ar) but different phases are found in oxidizing atmosphere, as expected.

The main idea behind this work is that advancing in the knowledge of the chemical and structural properties of Pr-rich ZrO_2–PrO_x composites in environmental conditions varying from reducing to oxidizing may help in the design of catalysts based on mixed-valence elements, particularly in those containing Pr.

2 | EXPERIMENTAL METHODS

Ceramic rods of $Zr_{1-x}Pr_xO_y$ with different Pr content were prepared by solid-state reaction. Powders of Pr_6O_{11} (99.9%, Merck) and ZrO_2 (99%, Merck) previously heated at 1200°C were mixed in the adequate proportion so as to get the desired nominal compositions. Rodlike precursors were isostatically pressed at 200 MPa and then sintered at 1500°C in air during 12 h. The sintered rods presented a diameter between 3 and 4 mm and were roughly 7 cm in length. Crystalline samples with a diameter of approximately 2 mm were grown, from the sintered rods, by the LFZ technique using a CO_2 laser ($\lambda = 10.6\ \mu m$) as a heating source (Blade-600, Electronic Engineering) at a growth rate of 300 or 100 mm/h. To study the influence of the processing atmosphere on the eutectic microstructure and phase composition, samples were grown in different atmospheres (O_2, air, N_2, and 5%H_2 in Ar), thus varying the conditions from oxidizing to reducing. The growth chamber was kept at a slight overpressure of 0.1–0.25 bar with respect to ambient pressure.

Compositional analysis and morphology were characterized by field emission SEM (FESEM) using a Carl Zeiss MERLIN microscope with an EDX detector incorporated.

X-ray diffraction patterns were collected with a D-Max Rigaku, RU300 diffractometer, using the Cu K_α radiation.

TABLE 1 Pr contents (PrO_x mol%) derived from energy-dispersive X-ray spectroscopy (EDX) analyses, lattice parameters (Å), and unit cell volume per $Zr_{1-x}Pr_xO_y$ formula (V_f, in $Å^3$) of phases forming the eutectic-like composites of the ZrO_2–PrO_x system processed in different atmospheres.

Processing atmosphere	Average PrO_x mol%	Light (high-Pr) phase			Dark (low-Pr) phase			% vol. dark phase	Δ PrO_x mol%
		PrO_x mol%	Latt. param.	V_f	PrO_x mol%	Latt. param.	V_f		
O_2, oxidized ring	87.15	93.3	$a_F = 5.432$ ($Pr^{3.87+}$, $O_{1.94}$)	80.1	86.6	$a_F = 5.421$ ($Pr^{3.84+}$, $O_{1.93}$)	79.6	>90	6.7
O_2, reduced core	86.5	92.6	$a_F = 5.478$ ($Pr^{3.74+}$, $O_{1.88}$) $a_A = 3.838$, $c_A = 6.072$	82.2 77.5	84.2	$a_F = 5.460$ ($Pr^{3.69+}$, $O_{1.87}$)	81.4	73–82	8.4
Air	85.9	91.7	$a_F = 5.440$ ($Pr^{3.84+}$, $O_{1.93}$)	80.5	83.3	$a_F = 5.427$ ($Pr^{3.78+}$, $O_{1.91}$)	79.9	70	8.4
N_2	82.2	88.3	$a_A = 3.837$, $c_A = 6.071$	77.4	76.2	$a_C = 10.909$	81.1	61	12.1
5%H_2(Ar)	82.3	87.3	$a_A = 3.835$, $c_A = 6.071$	77.3	76.4	$a_C = 10.902$ ($Pr^{3.07+}$, $O_{1.64}$)	81.0	47.4	10.9

Note: F, A, and C subindices stand for fluorite-, A-R2O3-, and C-R2O3-like phases, respectively. The Pr oxidation states derived either from the relation between the lattice parameter and ionic radii (in fluorite phases) or from the magnetic susceptibility (in the C-phase of the eutectic processed in 5%H2(Ar)) are given in brackets, as well as the resulting O stoichiometry). The relative volume of the dark (low-Pr) phase and the compositional separation between the high- and low-Pr phases (Δ) are also given.
Abbreviation: Latt. param., Lattice parameter.

Patterns were measured from 5° to 80° with $\Delta 2\theta = 0.03°$ and 1 or 3 s/step. Lattice parameters were determined with the help of the FullProf software.[13]

Raman measurements were performed using a DILOR XY spectrometer equipped with a liquid nitrogen–cooled CCD detector. Spectra were taken at RT with a ×50 microscope objective lens, using the 514.5 or 496.5 nm lines of an Ar^+ laser (model Coherent INNOVA 305).

Magnetic susceptibility was derived from magnetization measurements, under a magnetic field of 1000 Oe, performed on a SQUID detector magnetometer Quantum Design MPMS5.

3 | EXPERIMENTAL RESULTS

3.1 | Sample growth

Ceramic rods of mixed ZrO_2–PrO_x oxides were processed following the procedure described above. The PrO_x content of the mixtures was varied around 85% until eutectic microstructures were found. The compositions yielding eutectic microstructures in the four atmospheres used are listed in Table 1. The sample color varied from dark green (in reducing atmosphere) to almost black (in oxidizing atmosphere), indicating differences in the Pr oxidation state (see Figure S2). Transverse sections were cut and polished for electron microscopy and Raman experiments.

3.2 | Electron microscopy

The sample microstructure and elemental composition were analyzed by SEM and EDX, respectively. Figure 1A–D shows images of the transverse sections of samples processed in O_2, air, N_2, and 5%H_2(Ar) at either 300 or 100 mm/h. Eutectic-like lamellar microstructures are found in all four atmospheres, consisting of alternating dark-contrast (low Pr content) and light-contrast (high Pr content) phases, although in samples processed in O_2 at 300 mm/h only a central region of the processed rod displayed this eutectic-like aspect. For short, the low and high Pr content phases will be just called low-Pr and high-Pr phases, respectively. The lamellae interspacing is between 1.5 and 2.5 μm, and imperfect alignment is attributed to the high solidification rates used to prevent Pr volatilization. All parameters describing the lamellar microstructure and chemical composition vary with the processing atmosphere, as collected in Table 1. As the atmosphere evolves from more oxidizing (O_2) to more reducing (5%H_2(Ar)), the following trends are observed: (i) The volume proportion of the dark phase decreases from ~78% to ~50%. (ii) The Pr content of both phases decreases, from 84.2 to 76.4 PrO_x mol% for the dark phase and from 92.6 to 87.3 PrO_x mol% for the light phase, implying that the compositional difference between high- and low-Pr phases (Δ) increases from ~8 to ~11 mol% PrO_x. (iii) The simultaneous variation of the phase composition and of the phase proportion with the atmosphere results in a much smoother variation of the average composition, from 87 to 82 mol% PrO_x.

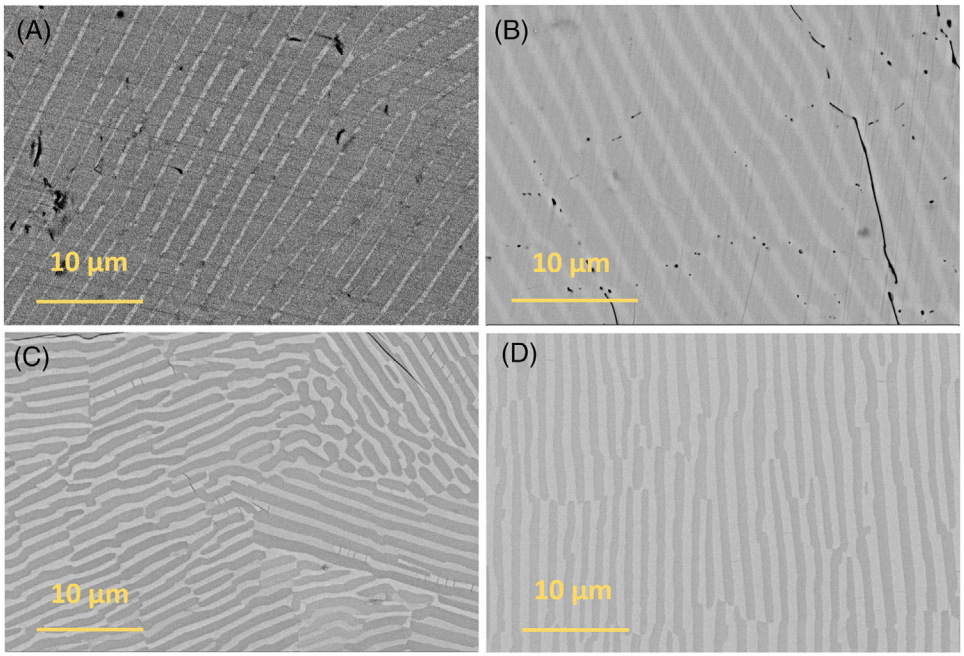

FIGURE 1 Transverse section images of ZrO_2–PrO_x samples solidified by laser-floating zone (LFZ) in (A) O_2, (B) air, (C) N_2, and (D) 5%H_2(Ar) atmospheres. Sample (B) was processed at 100 mm/h, all the others at 300 mm/h. Part (A) belongs to the central part of the rod processed in O_2.

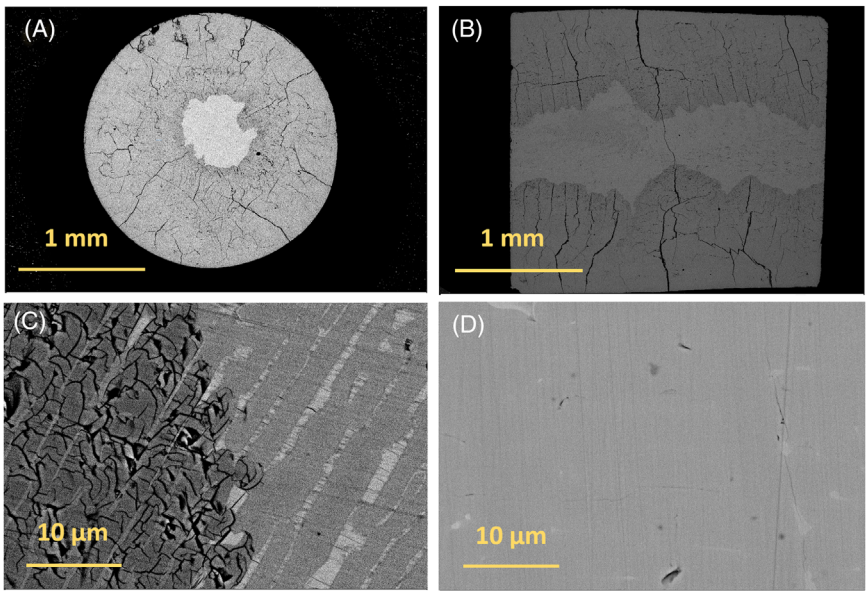

FIGURE 2 Transverse (A) and longitudinal (B) sections of the sample processed in O_2 at 300 mm/h, displaying separation between a light-contrast (reduced) inner core and a dark-contrast (oxidized) outer ring. Part (C) shows the border between the inner and outer regions of the same sample. Part (D) displays a section of a sample with the same average composition as that in parts (A–C) processed in O_2 at 100 mm/h, to highlight the disappearance of a eutectic microstructure.

The phase compositions (76.4 and 87.3 mol% PrO_x for the low and high-Pr phases, respectively) of the eutectic processed in 5%H_2(Ar) are similar to those found at high temperatures in Ref. [7] also in reducing conditions (76.5 and 87.6 mol% $PrO_{1.5}$, respectively).

It has to be noted that the sample processed in O_2 at 300 mm/h presented a core–shell aspect (Figure 2A,B) with a light-contrast core surrounded by a dark-contrast outer ring. A magnification of the border between both regions (Figure 2C) evidenced the presence of many cracks in the outer ring, suggesting the occurrence of thermo-mechanical stresses during solidification. Figure 2 also shows that the lamellar microstructure seems to faint in the outer region, to the point that any phase separation is hard to distinguish (Figure 1A belongs to the central region). EDX analyses showed that the central core had a slightly lower average Pr content than the outer region. The Pr content of each phase forming the composite was also different, as collected in Table 1. The core–shell aspect is attributed to incomplete oxygen uptake, resulting in an

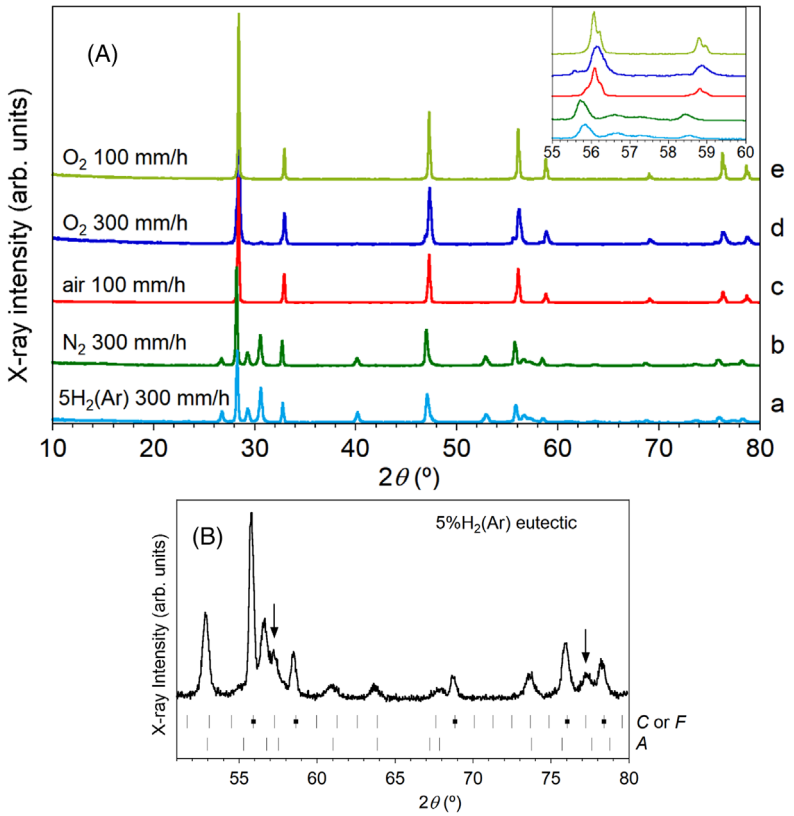

FIGURE 3 (A) X-ray diffraction (XRD) patterns of ZrO_2–PrO_x eutectics processed in 5%H_2(Ar) (A), N_2 (B), air (C), and O_2 (D), at the indicated rates. Pattern (E) belongs to a sample processed in O_2 at 100 mm/h, not displaying a eutectic microstructure (see Figure 2D). The inset shows a magnification of the 55°–60° region to highlight the presence of more than one phase in all cases except for the sample processed in O_2 at 100 mm/h, which evidences a single fluorite pattern. (B) The 50°–80° region of the pattern of the eutectic processed in 5%H_2(Ar) is magnified, to highlight the regions where the fit requires cell-doubling (marked with arrows). Tics marked with a square denote the fluorite-substructure reflections, which are common to C and F phases.

oxidized outer region surrounding a more reduced core. The above observations lead us to conclude that the outer region has lost the eutectic character. In fact, also the aspect of the inner core is anomalous, compared with proper eutectic composites obtained in air, N_2, or 5%H_2(Ar) (Figure 1B–D). The volume proportion of the dark phase, for instance, is quite below the limit (29%) that usually implies a change from lamellar to fibrilar–like eutectic microstructure.[14]

The preceding results suggest that no eutectic would form in the totally oxidized case. To verify this hypothesis, a sample with the same average Pr content was processed at a lower rate of 100 mm/h. As Figure 2D shows, the slowly processed sample displays a homogenous microstructure with no eutectic separation. We interpret that the slow growth enables oxygen diffusion throughout the whole sample so as to reach a homogeneous, single-oxidized phase. We will comment on these facts in Section 4.

3.3 | X-ray diffraction

The XRD patterns of ZrO_2–PrO_x eutectic or quasi-eutectic samples processed in 5%H_2(Ar), N_2, air, and O_2 are shown in Figure 3A (patterns a–d, respectively). Phase content and lattice parameters were analyzed with the help of the FullProf software.[13] The lattice parameters obtained from the profile fits are collected in Table 1. Although the most intense peaks are characteristic of a fluorite-like phase, an accurate fit requires at least a second minor phase. For comparison, we show in Figure 3A-E the pattern of the sample processed in O_2 at 100 mm/h, which can be explained by a single fluorite phase, with $a = 5.4334$ Å. A clear difference exists between eutectic samples processed in oxidizing atmospheres (see Figure S3), where both phases are of the fluorite (F) type (SG $Fm\bar{3}m$), and those processed in neutral or reducing atmospheres (Figure S4), where the main phase is fluorite-like and the minor phase is a trigonal phase of the A-R_2O_3 type (SG $P\bar{3}m_1$).

Looking in more detail at the diffraction patterns of the eutectics processed in N_2 and 5%H_2(Ar), we find peaks (specifically at ~57.2° and 77.2°, see Figure 3B) that are not explained by either the fluorite or the A phase of the F + A model. The phase attribution made in Ref. [7], where C + A phases were found in a reducing atmosphere, and the similarity between the chemical compositions of the eutectic phases reported in Ref. [7] with those of our eutectic processed in 5%H_2(Ar) led us to suspect that the low-Pr phase of the samples processed in N_2 or 5%H_2(Ar) might be a bixbyite phase instead of a fluorite one. In fact, the peaks around 57.2° and 77.2° are nicely explained as the (3 6 1) and (7 5 2) peaks, respectively, of a C-like phase with $Ia\bar{3}$ SG and $a_C \approx 2a_F$.

Although the C + A model clearly improves the F + A fit (see Figures S4b,d), an intriguing question arises as to why

the low angle superstructure peaks related to cell doubling, in particular the (211) peak at ~20°, are not observed in patterns (a) and (b) of Figure 3. An intense peak at that angle, for instance, was found in Ref. [5] for a 98 mol% PrO_x-rich sample, initially with F structure, which transformed to C-phase after a 15 h reducing treatment at 900°C. We speculate that the absence of clear superstructure peaks at low angle may be related to the disordered character of the C-like phases found in our samples. Disorder occurs both in the cation sublattice, because of the presence of ~24% Zr^{4+} cations per formula unit (pfu), as in the oxygen sublattice, with oxygen excess coming from charge compensation for Zr^{4+} as well as for some degree of Pr oxidation. Disordered fluorites are prone to order–disorder phenomena such as domain formation with short-range ordering at a few unit cell scale, resulting in the appearance of superstructure peaks related to the ordered regions. This is typically observed in systems undergoing order–disorder phase transitions with cell-doubling, such as the F to pyrochlore or F-to-C transitions. Depending on the domain size, peak broadening may affect to a greater degree the superstructure peaks and, from those, the low-angle ones, as in our case.[15] Thus, the low-Pr phase of the eutectic processed in 5%H_2(Ar) may be described as a fluorite phase containing vacancy-ordered C–like regions. The C + A model is further supported by Raman scattering results (section 3.4), where bands attributable to C and A-like phases are observed, and by arguments based on the relation between the stability of fluorite-like lattices and the concentration of anionic vacancies, as discussed in Section 4.

The case of the sample processed in O_2 is particular, because its pattern cannot be explained with only two phases. Both the detection of weak additional peaks as the asymmetric shape of the main reflections suggest the presence of at least four phases: two very close fluorite phases with $a_1 \sim 5.42$ Å and $a_2 \sim 5.43$ Å for the intense reflections, and another pair of fluorite phases with larger parameters, $a_3 \sim 5.46$ Å and $a_4 \sim 5.48$ Å, for the minor reflections at the low angle side of the most intense ones. A low amount of trigonal A-R_2O_3-like phase is also required to explain the weak reflections at 29.4°, 30.7°, and 40.2°, detectable only at high magnification scale. The explanation for the presence of four fluorite-like phases is clear when we see the images of the transverse and longitudinal sections of that sample (Figure 2). We have attributed the core–shell aspect to incomplete oxygen uptake. At the high melting temperatures, Pr ions would be highly reduced, even in O_2; upon cooling and solidification, oxygen uptake progresses radially but, because of the fast cooling rates, diffusion becomes progressively slower and does not reach the rod center. Thus, the final state of the sample consists of a reduced center and a more oxidized outer region. The

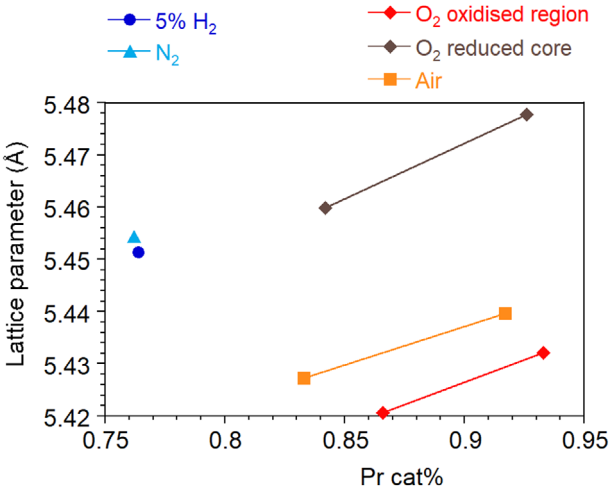

FIGURE 4 Lattice parameters of the fluorite-type phases found in the eutectic-like composites of the ZrO_2–PrO_x system processed in different atmospheres, as a function of the Pr cation content. The lattice parameters of C-R_2O_3 phases have been divided by two to normalize to the fluorite unit cell.

cracks in the outer region are attributed to the contraction produced upon oxidation. According to Figure 2, the volume proportion of the reduced core is ≲10%.

The two fluorite-like phases with smaller lattice parameters (a_1, a_2) are assigned to the oxidized ring whereas the two fluorite phases with larger lattice parameters (a_3, a_4) and low intensity are assigned to the partially reduced eutectic-like core. The appearance of a weak amount of A-like phase is attributed to the incomplete transformation of the high-Pr phase of the reduced region to a fluorite phase. Note that the lattice parameters of the reduced-core phases are considerably larger than those of the oxidized ring, despite the Pr contents being close, which is attributed to the larger ionic radius of Pr^{3+} compared to Pr^{4+}. With this assignment, the relation between chemical composition and lattice parameters is as shown in Figure 4. Two trends of increasing lattice parameters are observed: the first one goes from left to right and is due to increasing Pr content, as expected. The second one goes from bottom to top and is related to increasing reduction for fixed Pr content.

Some X-ray measurements were repeated several months after the first data collection. They evidenced the presence of $Pr(OH)_3$ in samples containing A-like phases but not in samples where the Pr-rich phase was fluorite-like. We attribute the presence of $Pr(OH)_3$ to the hydration of A-Pr_2O_3, which is known to react with ambient humidity.[16]

The diffraction results can be further exploited to get information about the Pr oxidation state in fluorite-like phases, taking benefit of the relation $R_C + R_O = a\sqrt{3}/4$ between the lattice parameter (a) and the ionic radii of its constituting elements, R_C and R_O being the

cation and oxygen ionic radii in eight- and fourfold coordination,[17] respectively. Using the lattice parameters collected in Table 1 and R_O = 1.38 Å, we derive the average cation radius of each phase, R_C, and write it as $R_C = \alpha R_{Pr} + (1-\alpha)R_{Zr}$, α being determined by EDX analyses. Taking R_{Zr} = 0.84 Å,[17] we extract the effective Pr radius, R_{Pr}, which is, in turn, an average over Pr^{3+} and Pr^{4+} radii, $R_{Pr} = \beta R_{Pr3+} + (1-\beta)R_{Pr4+}$, with R_{Pr3+} = 1.126 Å and R_{Pr4+} = 0.96 Å.[17] This yields the relative Pr^{3+}/Pr^{4+} content. XRD is advantageous in that the patterns of all phases present in the sample are superposed but not averaged, so that the oxidation states of the low and high Pr phases can be obtained separately. Applying this procedure to the fluorite-like phases found in samples processed in air or O_2, we find Pr oxidation states ranging from $Pr^{3.7+}$ to $Pr^{3.9+}$. The values obtained are collected in Table 1.

We note that the expression $R_C + R_O = a\sqrt{3}/4$ assumes eightfold cation coordination, whereas the average cation coordination would be smaller than eight in a defective fluorite. However, we have considered that in samples processed under oxidizing atmospheres, the vacancy concentration would be low and assumed the expression to be valid, at least in a qualitative way. The high oxidation states obtained support our assumption. For C-like phases, where the cation coordination is sixfold, the relation is no longer valid and cannot be used to derive the Pr oxidation state. Magnetic measurements are performed instead (see Section 3.5).

3.4 | Raman spectroscopy

Raman spectroscopy was used to support the phase assignment. With its short coherence length, this technique is ideally suited to detect short-range ordering effects as those expected in our materials.[18] Figure 5 shows representative spectra of samples processed in O_2 and 5%H_2(Ar). The sample processed in 5%H_2(Ar) presents narrow peaks at 108, 190, and 416 cm^{-1}, very close to those of A-Pr_2O_3,[19] which we assign to the Pr-rich component of the eutectic. Three more peaks at 143, 295, and 356 cm^{-1} arise from $Pr(OH)_3$ developed upon exposure to air.[20,21] The identification of $Pr(OH)_3$ is supported by the detection of the OH^- stretching band at 3605 cm^{-1}. The narrow peaks are superposed to broad bands centered around 340, 580, 670, and 800 cm^{-1}, assigned to the low-Pr phase with perhaps some admixture of Pr^{3+} crystal-field transitions.

To clarify the band assignment, we processed in 5%H_2(Ar) a sample of $Pr_{0.75}Zr_{0.25}O_x$ stoichiometry, close to that of the low-Pr phase of the eutectic processed in 5%H_2(Ar). Its spectrum (Figure 5) presents a broad intense band centered at 330 cm^{-1} and a weaker one at 660 cm^{-1},

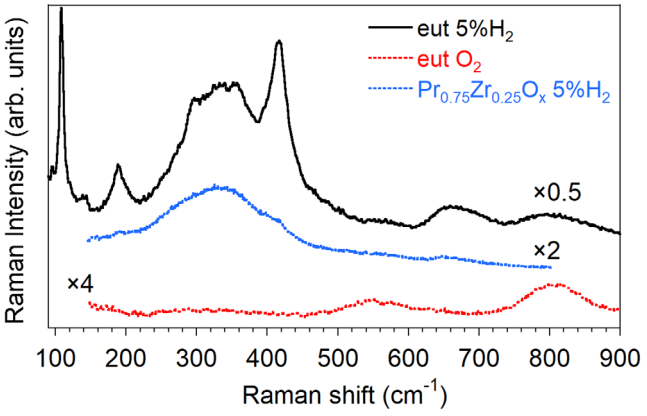

FIGURE 5 The Raman spectra of the ZrO_2–PrO_x eutectic composite processed in 5%H_2(Ar) (top spectrum, in black) is compared with that of the sample processed in O_2 (bottom spectrum, in red) and with that of the $Pr_{0.75}Zr_{0.25}O_x$ compound processed in 5%H_2(Ar) (in blue).

thus supporting the attribution of these two bands to the low-Pr phase. It is interesting that the wavenumber of the main band is similar to that of the related C-R_2O_3 compounds (312 cm^{-1} for metastable C-La_2O_3,[22] and 335 cm^{-1} for metastable C-Nd_2O_3[23]).

The broad aspect of the bands assigned to the low-Pr phase is not surprising, owing to the presence of cation chemical disorder and partially-filled anion vacancies. The spectrum, however, supports our attribution of the low-Pr phase to a bixbyite phase and not to a fluorite one. In fluorite-like stabilized cubic zirconia (YSZ), for instance, the Raman spectrum resembles more a density of states than the single mode expected for a well-ordered fluorite and extends up to 600 cm^{-1}, although in nanometric c-ZrO_2, a single broad band ascribed to the fluorite T_{2g} mode is found at 490 cm^{-1}.[24] On the other hand, the main band in PrO_2 appears at 430 cm^{-1} and is also attributed to the fluorite T_{2g} mode.[25] In our case, the spectrum of the low-Pr phase found in reducing atmosphere differs considerably both from the density-of-states-aspect of stabilized zirconia but also from that of well-ordered fluorites and, as we have seen, agrees with the trend expected for a C-type phase. In samples processed in O_2 or in air, the spectrum is even more featureless because both phases are disordered fluorites.

3.5 | Magnetic susceptibility

The oxidation state of the low-Pr phase of the eutectic processed in 5%H_2(Ar) was derived from magnetic susceptibility measurements (Figure 6). The data analysis in eutectic systems is hindered by the presence of two magnetic phases with different compositions where, moreover,

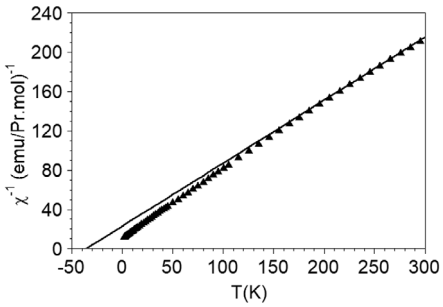

FIGURE 6 Inverse magnetic susceptibility per Pr ion of the low Pr phase of the eutectic processed in 5%H_2(Ar). The data have been derived from the total susceptibility, which includes the contributions of the low and high Pr phases, by the procedure outlined in the text. Triangles are the experimental points, and the line is the fit to a Curie–Weiss law in the 195–295 K range.

the Pr oxidation state may differ. To extract the Pr oxidation state, we have proceeded as follows:

We assume that the sample is composed of two phases L and H, with low and high Pr contents, and molar contents n_L and n_H, respectively. We also assume that the Pr content pfu of each phase is given by $[Pr]_L$ and $[Pr]_H$, respectively. Knowing the sample mass and average composition, both $n_{L,H}$ and $[Pr]_{L,H}$ are determined from an EDX analysis of each phase and of the average sample (see Table 1).

The total magnetic susceptibility $\chi = \chi_L + \chi_H$ can be written in terms of the molar and Pr content of each phase as $\chi = n_L[Pr]_L\chi_{mL} + n_H[Pr]_H\chi_{mH}$, where $\chi_{mL} = \chi_L/n_L[Pr]_L$ and $\chi_{mH} = \chi_H/n_H[Pr]_H$ are the susceptibilities per Pr ion in the L and H phases, respectively. To separate the contribution of both phases, we assume that the Pr-rich A-like phase is completely reduced. The assumption is justified by the small tolerance of the A phase to cation oxidation. Assuming for the H phase a Curie–Weiss (CW) dependence in the 200–300 K range, χ_{mH} is written as $\chi_{mH} = [C/(T - \theta)]$, where the Curie constant C fulfills $8C = \mu_{eff}^2$, and we take $\mu_{eff,H} = \mu(Pr^{3+}) = 3.58\ \mu_B$ and $\theta = -73$ K, the value reported for A-Pr_2O_3.[26]

Then, we subtract $\chi_H = n_H[Pr]_H\chi_{mH}$ from the total susceptibility, to get χ_L. Knowing n_L and $[Pr]_L$ from EDX, we work out χ_{mL} and fit it to another CW law at high temperature, which gives $\mu_{eff,L} = 3.52\ \mu_B$. Finally, writing $\mu_{eff,L}{}^2 = \varepsilon\mu_{Pr3+}{}^2 + (1 - \varepsilon)\ \mu_{Pr4+}{}^2$ and taking the reference values $\mu_{Pr3+} = 3.58\mu_B$ and $\mu_{Pr4+} = 2.54\mu_B$ for Pr^{3+} and Pr^{4+} in their ground-state multiplets, respectively, we find $\varepsilon = 0.93$, that is, a very low oxidation state $Pr^{3.07+}$ for Pr ions in the low-Pr phase of the 5%H_2(Ar) eutectic. The result is in agreement with the greenish color of the sample (Figure S2).

4 | DISCUSSION

The preceding results evidence that eutectic-like lamellar microstructures are formed in directionally solidified ZrO_2–PrO_x mixed oxides at compositions around 82–87 mol% PrO_x when the processing atmosphere is either reducing (5%H_2(Ar)), neutral (N_2) or partially oxidizing (air). However, the sample processed in O_2 behaves in a clearly different way and provides a hint of the system behavior under extremely oxidizing conditions. The two-region aspect of that sample, with a reduced inner core surrounded by an oxidized outer ring, suggests incomplete oxidation during cooling. Both the microstructure and the elemental analysis indicate that no eutectic is produced in the outer region and, if at all, in an anomalous way in the inner core. The homogeneous microstructure of a sample with the same average Pr content, processed in O_2 at a lower rate of 100 mm/h, and the single-fluorite character of its XRD pattern, confirm that no eutectic exists in the limit of total oxidation.

The evolution of the eutectic composition and phase symmetry in the ZrO_2–PrO_x system upon changing the processing atmosphere, as well as the likely absence of a eutectic point in the O_2 case, can be understood in relation with the trend observed in the eutectics of the ZrO_2–R_2O_3 series and would be, as most structural properties of rare-earth compounds, dictated by the relation between phase stability, average cation size, and vacancy concentration.[7,9] According to Ref. [7], the average rare-earth content in the eutectic increases as the rare-earth size decreases, from 62.5 mol% R_2O_3 for R = La to 82 mol% for R = Ho, Er, and Y. The composition of the high-R phase, in turn, increases from 70 to 95 mol% of R_2O_3 along the series. This evolution can be attributed to the limited stability of the A-R_2O_3 structure: As the rare-earth size decreases, the stable phase of the R_2O_3 compounds evolves from A-type first to B (a monoclinic structure closely related to A-phase) and then to C-type.[27] The increasing rare-earth content at the high-R phase warrants the eutectic occurrence as a C + A or C + C′ combination of phases, depending on the effective ionic radii. As regards the low-R phase, with R content increasing from 55 to 70 mol% R_2O_3 along the series, its C-like structure can be ascribed to the higher tolerance of the bixbyite lattice to anion vacancies, compared with the fluorite one, and to small cations like Zr^{4+}, compared with the A-phase.

The same ideas can be applied to the ZrO_2–PrO_x system upon changing the processing atmosphere or the temperature, allowing for the effective cation size dependence on both the (Pr, Zr) stoichiometry as on the Pr oxidation state. First, we note that the ionic radius of Pr^{4+} in eightfold coordination is 0.96 Å, just slightly smaller than Yb^{3+} in

the same coordination (0.985 Å),[17] for which the occurrence of a eutectic point is doubtful.[7] This suggests that the fully oxidized Pr^{4+} ion is too small to form a eutectic, which supports our proposal that the microstructure of the sample processed in O^2 should be rather ascribed to phase evolution upon cooling (see below). For less severe oxidation, the symmetry and composition of the eutectic phases will depend mainly on the effective ionic radius in the high-Pr phase, allowing for the decrease of the Pr size from 1.126 Å for Pr^{3+} to 0.96 Å for Pr^{4+}.[17] In analogy with the eutectics of the ZrO_2–R_2O_3 series, combinations going from C + A to C + C phases might be expected for increasing oxidation degree if only the variation of the ionic radii were considered. The ZrO_2–PrO_x system has, however, the added ingredient of increasing oxygen content to compensate for higher Pr oxidation states, so that in the presence of high enough O_2 concentration, C phases are expected to evolve toward F phases and A phases into C or F phases. This explains, in general terms, the C + A phases obtained in N_2 and 5%H_2(Ar) atmospheres, and the F + F phases found in air.

The relation among Pr oxidation state, vacancy content, and the formation of F-, C-, or A-like phases is clearly exemplified in our eutectics. In preceding sections, we have shown that two ranges of oxidation states are found: between $Pr^{3.7+}$ and $Pr^{3.9+}$ for samples processed in oxidizing atmosphere, which achieve fluorite-type phases, and $Pr^{3.07+}$ for the C-phase of the eutectic processed in 5%H_2(Ar) (Pr ions are assumed to be fully reduced in A-like phases). Translating these oxidation states to oxygen stoichiometry, allowing for the cation composition of each phase, we find that the number of oxygen vacancies pfu varies between 0.06 and 0.13 in the fluorite phases of samples processed in air or O_2 and ∼0.35 in the C-phase of the eutectic processed in 5%H_2(Ar). These values agree with the assumption that for high enough vacancy concentration (typically 0.25 pfu), the fluorite lattice is no longer stable so that, in the absence of cation ordering, an evolution to a vacancy-ordered C-like phase takes place. Interestingly, the vacancy concentration determined for the low-Pr phase of the eutectic processed in 5%H_2(Ar) is just in the range of the C-phase stability at high temperature according to Rouanet's PD. Because of the fast cooling involved in LFZ, the high-temperature C phase is preserved metastably at RT instead of segregating into pyrochlore + A-phase. In contrast, in oxidizing atmospheres, this high-temperature C-phase evolves to a fluorite phase upon oxidation during cooling.

The particular behavior of the sample processed in O_2 can be understood as follows: Just after crystallization, even in O_2 atmosphere, a C + A eutectic with highly reduced Pr ions is expected to develop. As the temperature decreases, both phases become increasingly oxidized. The low-Pr C-phase can easily accommodate Pr^{4+} ions and oxygen excess, eventually transforming to a fluorite phase, but the high-Pr A-phase cannot stand neither the reduced size of Pr^{4+} nor the higher O content. We may now recall that in the $PrO_{1.5+\delta}$ system, different stable and/or metastable phases form depending on the oxygen partial pressure and thermal history.[28,29] At the high temperatures where phase evolution takes place in LFZ-processed samples (≫1000°C), the stable phases are as follows: A-Pr_2O_3, in highly reducing conditions; a C-like $PrO_{1.5+\delta}$ phase, for moderate oxygen excess, and a defective fluorite PrO_{2-z} phase for high oxygen content (θ, σ, and α phases in Eyring's notation, respectively). Interestingly, the transition from A to C-like phases as the oxygen content increases seems to occur through a phase separation region of A + C type above 900°C.[28]

Transferring these ideas to the high-Pr phase of the eutectic, we propose that in O_2 phase, segregation occurs *within the A–phase lamellae* into a Pr-rich reduced A-like phase at the center and a Pr-poor oxidized C-like region (which oxidizes to fluorite on cooling) toward the interfaces with the low-Pr phase, resulting in a narrowing of the Pr rich lamellae, as observed. Although the appearance is still that of a lamellar eutectic, it should be considered more an intermediate between the initial (partially reduced) state, with eutectic microstructure, and the final (fully oxidized) state, consisting probably of a single, defective fluorite phase. The decrease of the compositional separation between Pr-rich and Pr-poor phases (Δ) as the atmosphere becomes more oxidizing supports our hypothesis. With this interpretation, the ZrO_2–PrO_x system would behave the same as the related ZrO_2–CeO_x system, where a eutectic point exists in the fully reduced ZrO_2–Ce_2O_3 system,[11] but not in the oxidized ZrO_2–CeO_2 case.[12]

At this point, we note that both XRD and Raman results of the present work support the assignment of the low Pr phase in neutral or reducing atmosphere to a C-like phase. We have found no evidence of the "tetragonally-distorted fluorite" phase proposed in Ref. [6].

More interesting is the finding in air atmosphere of a eutectic with two fluorite phases of close composition. Michel et al.[8] studied the growth relations between the phases of ZrO_2–R_2O_3 eutectics (R = Nd, Sm, Dy) produced by the skull-melting technique in air and found two C-type phases with close lattice parameters for R = Dy. The relative crystallographic orientation is termed *syntaxy*, that is, the intergrowth of both phases with the parallelism of equivalent planes and directions. For the mixed-valence Pr case, we have proposed that in oxidizing atmosphere both C phases evolve toward fluorite phases. Although the syntaxy conformation may occur, we speculate that there may

be a different local ordering at the microscopic level in both fluorite phases, reminiscent of the initially reduced state, but elucidating this point is out of the scope of this work.

Our results imply a difference between LFZ-processed samples and those quenched from the melt in air,[7] as regards the symmetry of the high-Pr phase in oxidizing atmosphere. Although LFZ involves fast cooling, it is not as fast as a quenching, and oxygen uptake can occur during cooling, resulting in two fluorite phases instead of the C + A combination found in samples quenched from the melt in air.[7]

A considerable difference is expected also between samples produced by LFZ and those synthesized by low-temperature techniques, such as sol–gel processing methods[2] or coprecitipitation.[5] In LFZ-processed samples, Pr is highly reduced in any atmosphere at high temperature, and the final oxidation state will depend on the kinetics of oxygen diffusion relative to cooling rate. For fast cooling rates, the obtained phases may not be those predicted by the PD in equilibrium and closer to the high temperature ones. In samples produced at low temperatures, on the other hand, size effects *metastabilise* high symmetry phases, and the final structures and oxidation states will depend both on cation and anion diffusivities, probably leading also to nonequilibrium phases. This may explain, for instance, why only F-like phases are obtained in Ref. [2] for 1:3, 1:1, and 3:1 Zr:Pr ratios after calcining at 900°C in air. It may also explain why the F-like $Pr_{0.98}Zr_{0.02}O_x$ compound, previously annealed in air at 900°C, transforms to a C-phase after a reducing treatment at 900°C in Ref. [5], instead of to the expected A-like phase.

We may also comment on the composition of the A-like phases obtained in neutral or reducing atmosphere. EDX analyses evidence a low but non-negligible 12%–13%ZrO_2 content in those phases, which is larger than the ~3%ZrO_2 solubility predicted by the equilibrium PD. The anomaly may arise from two sources: First, the fast cooling involved in LFZ processing may yield at RT a metastable phase with much higher Zr content, similar to the one forming the eutectic at the crystallization temperature. Second, it might occur that the Zr content is overestimated in EDX analyses because of the narrow width (<1 μm) of the light-contrast phases. In fact, the cell volumes obtained for the A-like phases from XRD data (77.3–77.4 Å^3) are marginally lower than that of A-Pr_2O_3 ($V_f \approx 77.5$ Å^3).[30] The Raman shifts of the modes attributable to the high-Pr phase are also very close to those of Pr_2O_3, which suggests a low Zr content.[19]

As regards the potential applicability of these mixed oxides, the more homogeneous, almost single-phase composites obtained in oxidizing conditions are likely to provide better catalytic properties. Composites obtained under neutral or reducing conditions, where one of the phases is of the A-R_2O_3 type, are not expected to present the high oxygen conductivity required for fast redox processes to take place, because of their low tolerance to oxygen stoichiometry variations.

5 | SUMMARY AND CONCLUSIONS

We have processed by the laser-assisted directional solidification technique eutectic composites of the ZrO_2–PrO_x system in O_2, air, N_2, and 5%H_2(Ar) atmospheres. The composition and symmetry changes found in the different atmospheres are compared with results from the literature for the same or related systems, notably ZrO_2–R_2O_3 eutectics or single-phase compounds.

The phase content is C + A in neutral or reducing atmosphere, but two fluorites of close composition are found in air atmosphere with the present processing technique, which implies fast cooling rates. Our results suggest that in the limit of total oxidation, no eutectic would form, in analogy with the ZrO_2–CeO_2 case. The present results agree with previously reported ones in reducing atmosphere but provide evidence of different crystallochemistry in oxidizing atmosphere. Both C- and A-like phases formed under reducing atmosphere at high temperature transform to F-type upon exposure to an oxygen-rich environment.

Differences between LFZ-processed samples and quenched ones are highlighted and attributed to the different cooling rates inherent to both techniques. Cooling kinetics is as important as pO_2 in establishing the final oxidation degree and phase symmetry. Composites processed in highly oxidizing conditions are likely to perform better as catalyst materials. Our work also evidences the relevance of the synthesis method and of the initial state of the sample previous to any thermal treatment.

ACKNOWLEDGMENTS

The authors acknowledge financial support from the Spanish Government through grants PID2019-107106RB-C32, PID2021-124863OB-I00, and BES-2017-079683, funded by MCIN/AEI/10.13039/501100011033 and the European Union through "ERDF A way of making Europe." The Gobierno de Aragón is acknowledged for the financial support to the research group T02-20R. We thank the Servicio General de Apoyo a la Investigación (Universidad de Zaragoza) for technical support in X-ray diffraction, magnetic susceptibility and electron microscopy experiments.

ORCID

María Luisa Sanjuán https://orcid.org/0000-0002-5793-2058

REFERENCES

1. Putna ES, Vohs JM, Gorte RJ, Graham GW. An examination of praseodymia as an oxygen-storage component in three-way catalysts. Catal Lett. 1998;54:17–21.
2. Narula CK, Haack LP, Chun W, Jen H-W, Graham GW. Single-phase PrO_y-ZrO_2 materials and their oxygen storage capacity: a comparison with single-phase CeO_2-ZrO_2, PrO_y-CeO_2, and PrO_y-CeO_2-ZrO_2 materials. J Phys Chem B. 1999;103:3634–9.
3. Logan AD, Shelef M. Oxygen availability in mixed cerium/praseodymium oxides and the effect of noble metals. J Mater Res. 1994;9:468–75.
4. Yu Sinev M, Graham GW, Haack LP, Shelef M. Kinetic and structural studies of oxygen availability of the mixed oxides $Pr_{1-x}M_xO_y$ (M = Ce, Zr). J Mater Res. 1996;11:1960–71.
5. Abel J, Lamirand-Majimel M, Majimel J, Bellière-Baca V, Harlé V, André G, et al. Oxygen non-stoichiometry phenomena in $Pr_{1-x}Zr_xO_{2-y}$ compounds ($0.02 < x < 0.5$). Dalton Trans. 2014;43:15183–91.
6. Krasil'nikov MD, Vinokurov IV, Nikitina SD. Physicochemical properties of solid solutions in the zirconium dioxide–praseodymium oxide system in air; in Fiz. Khim. Elektrokhim. Rasplavl. Tverd. Elektrolitov, Tezisy Dokl. Vses. Konf. Fiz. Khim. Ionnykh Rasplavov Tverd. Elektrolitov, 7th, Sverdlovsk, USSR, September 18–20, 1979, Vol. 3, pp. 123–125. Akademiya Nauk SSSR, Ural'skii Nauchnyi Tsentr, Ekaterinburg, USSR. 1979.
7. Rouanet A. Contribution a l'étude des systèmes zirconia—oxydes des lanthanides au voisinage de la fusion: mémoire de thèse. Rev Intern Hautes Temper Refract. 1971;8:161–80.
8. Michel D, Rouaux Y, Perez y Jorba M. Ceramic eutectics in the systems ZrO_2-Ln_2O_3 (Ln = Lanthanide): unidirectional solidification, microstructural and crystallographic characterization. J Mater Sci. 1980;15:61–6.
9. Andrievskaya ER. Phase equilibria in the refractory oxide systems of zirconia, hafnia and yttria with rare-earth oxides. J Eur Ceram Soc. 2008;28:2363–88.
10. Aldebert P, Traverse JP. Étude par diffraction neutronique des structures de haute témperature de La_2O_3 et Nd_2O_3. Mat Res Bull. 1979;14:303–23.
11. Negas T, Roth RS, McDaniel CL, Parker HS, Olson CD. Influence of K_2O on the cerium oxide-ZrO_2 system. In: Lundin CE, editor. Proceedings of the 12th rare earth research conference. Vol. II. Vail, Colorado, USA: University of Denver; 1976. p. 605–14.
12. Yashima M, Morimoto K, Ishizawa N, Yoshimura M. Diffusionless tetragonal–cubic transformation temperature in zirconia–ceria solid solutions. J Am Ceram Soc. 1993;76:2865–8.
13. Rodriguez-Carvajal J. FULLPROF: a program for Rietveld refinement and pattern matching analysis, abstracts of the satellite meeting on powder diffraction of the XV Congress of the IUCr, p. 127. Toulouse, France; 1990.
14. Llorca J, Orera VM. Directionally solidified eutectic ceramic oxides. Prog Mater Sci. 2006;51:711–809.
15. Heremans C, Wuensch BJ, Stalick JK, Prince E. Fast-ion conducting $Y_2(Zr_yTi_{1-y})_2O_7$ pyrochlores: neutron Rietveld analysis of disorder induced by Zr substitution. J Solid State Chem. 1995;117:108–21.
16. Adachi G-y, Imanaka N. The binary rare earth oxides. Chem Rev. 1998;98:1479–514.
17. Shannon RD. Revised effective ionic radii and systematic studies of interatomic distances in halides and chalcogenides. Acta Crystallogr, Sect A. 1976;A32:751–67.
18. Sanjuán ML. Raman spectroscopy study of disorder phenomena and size effects in pyrochlores. In: Chowdhury A, editor. Pyrochlore ceramics: properties, processing, and applications. Elsevier series on advanced ceramic materials. Amsterdam: Elsevier; 2022. p. 95–159.
19. Zarembowitch J, Gouteron J, Lejus AM. Raman spectra of lanthanide sesquioxide single crystals with A-type structure. Phys Status Solidi B. 1979;94:249.
20. Swanson BI, Machell C, Beall GW, Milligan WO. Vibrational-spectra and assignments for lanthanide trihydroxides. J Inorg Nucl Chem. 1978;40:694–6.
21. Sanivarapu SR, Lawrence JB, Sreedhar G. Role of surface oxygen vacancies and lanthanide contraction phenomenon of $Ln(OH)_3$ (Ln = La, Pr, and Nd) in sulfide-mediated photoelectrochemical water splitting. ACS Omega. 2018;3:6267–78.
22. Orera A, Larraz G, Sanjuán ML. Spectroscopic study of the competition between dehydration and carbonation effects in La_2O_3-based materials. J Eur Ceram Soc. 2013;33:2103–10.
23. Ubaldini A, Carnasciali MM. Raman characterisation of powder of cubic RE_2O_3 (RE = Nd, Gd, Dy, Tm, and Lu), Sc_2O_3 and Y_2O_3. J Alloys Compd. 2008;454:374–8.
24. Phillippi CM, Mazdiyasni KS. Infrared and Raman spectra of zirconia polymorphs. J Am Ceram Soc. 1971;54:254.
25. Dogra S, Singh J, Sharma ND, Samanta K, Poswal HK, Sharma SM, et al. Phase progression via phonon modes in lanthanide dioxides under pressure. Vib Spectrosc. 2014;70:193–9.
26. Kern S. Magnetic susceptibility of praseodymium oxides. J Chem Phys. 1964;40:208–12.
27. Foex M, Traverse J-P. Étude du polymorphisme des sesquioxydes de terres rares à haute température. Bull Soc franç Minér Crist. 1966;89:184–205.
28. Hyde BG, Bevan DJM, Eyring L. On the praseodymium + oxygen system. Philos Trans R Soc London, Ser A. 1966;259:583–614.
29. Burnham DA, Eyring L. Phase transformations in the praseodymium oxide-oxygen system: high-temperature X-ray diffraction studies. J Phys Chem. 1968;72:4415–24.
30. Greis O, Ziel R, Breidenstein B, Haase A, Petzel T. The crystal structure of the low-temperature A-type modification of Pr_2O_3 from X-ray powder and electron single crystal diffraction. J Alloys Compd. 1994;216:255–8.

SUPPORTING INFORMATION

Additional supporting information can be found online in the Supporting Information section at the end of this article.

How to cite this article: Grima L, Peña JI, Sanjuán ML. Ceramics with eutectic microstructure in the ZrO_2–PrO_x system. J Am Ceram Soc. 2023;106:7098–7108. https://doi.org/10.1111/jace.19305

Journal of Membrane Science 630 (2021) 119057

Contents lists available at ScienceDirect

Journal of Membrane Science

journal homepage: http://www.elsevier.com/locate/memsci

High CO_2 permeability in supported molten-salt membranes with highly dense and aligned pores produced by directional solidification

L. Grima [a], G.A. Mutch [b], P.B. Oliete [a], W. Bucheli [a], R.I. Merino [a], E.I. Papaioannou [b], J. J. Bailey [c,d], M.D. Kok [c,d], D.J.L. Brett [c,d], P.R. Shearing [c,d], I.S. Metcalfe [b], M.L. Sanjuán [a,*]

[a] Instituto de Nanociencia y Materiales de Aragón (INMA), CSIC-Universidad de Zaragoza, Facultad de Ciencias, Universidad de Zaragoza, 50009, Zaragoza, Spain
[b] Materials, Concepts and Reaction Engineering (MatCoRE) Research Group, School of Engineering, Newcastle University, Newcastle-upon-Tyne, NE1 7RU, UK
[c] The Electrochemical Innovation Lab, Department of Chemical Engineering, University College London, London, WC1E 7JE, UK
[d] The Faraday Institution, Quad One, Becquerel Ave, Harwell Campus, Didcot, OX11 0RA, UK

ARTICLE INFO

Keywords:
CO_2 separation membranes
Dual-phase membranes
Permeation
MgSZ-MgO eutectic
Directional solidification

ABSTRACT

Composite molten salt-ceramic membranes are promising devices for high-temperature CO_2 separation. Intensive material properties impact on separation performance as do membrane geometry (thickness) and microstructure (pore volume fraction, size, connectivity, and tortuosity factor). Although controlling pore size is considered somewhat routine, achieving pore alignment and connectivity is still challenging. Here we report the production of the first gas separation membrane using a porous ceramic matrix obtained from a directionally-solidified magnesium-stabilised zirconia (MgSZ) – MgO fibrilar eutectic as the membrane support. MgO was removed from the parent material by acid-etching to create a porous matrix with highly aligned pores with diameters of ~1 μm. X-ray nano-computed tomography of a central portion (~32,000 μm^3) of the support identified ~21% porosity, with all pores aligned within 10° and ~76% percolating along the longest sampled length. Employing the matrix as a support for a carbonate molten salt, a high CO_2 permeability of $1.41x10^{-10}$ mol $m^{-1}.s^{-1}.Pa^{-1}$ at 815 °C was achieved, among the highest reported for supported molten-carbonate membranes (typically 10^{-12} to 10^{-10} mol $m^{-1}.s^{-1}.Pa^{-1}$ at similar temperatures). We suggest that the high permeability is attributable to the excellent pore characteristics resulting from directional solidification, namely a dense array of parallel, micron-scale pores connecting the feed and permeate sides of the membrane.

1. Introduction

High-performance membranes have short transport pathways of low tortuosity. If such a structure can be achieved, high-permeability membranes may provide transformative solutions for energy-intensive separations such as CO_2 capture. Supported molten-salt membranes are emerging as promising candidates for CO_2 separation due to their unrivalled and desirable combination of high selectivity and high permeability [1]. Furthermore, they are operable at the high-temperature conditions found in important applications including enhanced water-gas-shift or flue gas separation. Typically, they are composed of molten carbonate salts supported in the pore space of an inorganic solid [2,3]. Supports have included oxygen-ion and/or electron-conducting porous inorganic solids, however, to date their pore structures have been typically tortuous and unrefined. To further improve separation performance, promising intensive material properties (*e.g.* high ionic conductivity in the molten salt) should be paired with a membrane structure likely to provide high performance.

A conventional understanding of supported molten-salt membranes [4–9] tells us that CO_2 permeation starts with the formation of CO_3^{2-} anions at the feed-side membrane surface, where gas, melt and solid support meet. The precise surface reactions depend on the nature of the support; for a purely ionic oxygen conductor it is postulated that CO_2 in the feed gas reacts with oxide ions from the ceramic support to form CO_3^{2-} ions that diffuse through the molten carbonate phase (Equation (1)).

$$CO_{2\,(g)} + O^{2-}{}_{(s)} \rightleftarrows CO_3^{2-}{}_{(l)} \quad (1)$$

Within this approach the permeate flux is given by Equation (2) [4,5,9].

* Corresponding author.
E-mail address: sanjuan@unizar.es (M.L. Sanjuán).

https://doi.org/10.1016/j.memsci.2021.119057
Received 6 October 2020; Received in revised form 5 January 2021; Accepted 5 January 2021
Available online 12 January 2021
0376-7388/

$$J_{CO_2} = \frac{RT}{4LF^2}\sigma_{eff} ln\left(\frac{p_{CO_2}(\text{permeate})}{p_{CO_2}(\text{feed})}\right), \quad (2)$$

where L is the membrane thickness, p_{CO2}(feed) and p_{CO2}(permeate) are the CO_2 partial pressures at the feed and permeate sides, respectively, and σ_{eff} is the effective ambipolar conductivity that results from the simultaneous but separate transport of ionic species in the molten carbonate and solid oxide phases. Assuming a negligible electronic transport number in the support, the effective ambipolar conductivity is given by Equation (3).

$$\sigma_{\text{eff}} = \frac{\left[(\phi/\tau)_c\sigma_c\right]\left[(\phi/\tau)_{so}\sigma_{so}\right]}{\left[(\phi/\tau)_c\sigma_c\right] + \left[(\phi/\tau)_{so}\sigma_{so}\right]}, \quad (3)$$

where σ_c, $(\phi/\tau)_c$ and σ_{so}, $(\phi/\tau)_{so}$ are the conductivity and volume-fraction-to-tortuosity-factor ratio of carbonate and solid oxide phases, respectively [9]. In the case of complete pore filling by carbonates, ϕ_c equals the support porosity, usually denoted by ε.

According to Equations (2) and (3), membrane performance depends on intensive material properties, such as molten carbonate and solid oxide conductivities, and on geometric and microstructural characteristics, with the latter influenced by the support preparation method. Laboratory-scale investigations have mainly focussed on membranes with supports prepared by isostatic pressing or tape-casting, due to the simplicity of preparation [4,10]. More recently, tubular supports have been investigated in an effort to move closer to membranes with an inherent affinity to scale-up [11–14]. However, in most cases, porosity control in the support relies upon the use of sacrificial materials, such as pore formers, where the quantity, size and shape of the pore former dictates the final porosity and pore structure of the support.

Although the model based on Equations (1)–(3) does not contain a full description of how the components of pore structure (pore volume, size, connectivity and tortuosity factor) impact on gas permeation, a relationship between permeation and properties, such as support particle interconnectivity, molten salt-support interfacial area, molten salt-gas interfacial area and total membrane conductivity, can be anticipated [2,3,9]. In a samarium-doped ceria (SDC)-carbonate system, for instance, the conductivity increased linearly with the SDC-carbonate interfacial area but was inversely proportional to the tortuosity factor [15]. In a lanthanum strontium cobalt ferrite (LSCF)-carbonate system, permeability could be increased (assuming the conductivity of the carbonate and oxygen-ion conducting support is fixed) by increasing the porosity-to-tortuosity-factor ratio (for the carbonate phase) and solid-fraction-to-tortuosity-factor ratio (for the ceramic phase) [9]. In an SDC-supported membrane, in which pore formers were employed to fabricate a highly-interconnected structure, a permeability above 10^{-10} mol $m^{-1}.s^{-1}.Pa^{-1}$ was reported, suggesting that pore connectivity is important in achieving high permeability [16]. Recently, it was shown (using a nominally inert membrane support), that permeation rate is limited by molten salt-gas interfacial area at the permeate side [17], indicating that other mechanisms beyond Equation (1) at the triple-phase boundary (TPB) are involved, probably based on different interfacial reactions [3]. Taken together, it is clear that there is a need for support preparation methods that allow exquisite control of e.g. interfacial area, triple-phase boundary, and tortuosity factor in order to go beyond the conventional understanding of Equations (1)–(3) which struggle to explain much of the observed membrane behaviour.

Although progress has been made in achieving pore-size control [18–21], and in fabricating thin membranes [11,12,22], in general these methods lack directional control, *i.e.* the alignment of the pore structure with the direction of desired gas transport. Methods that generate ceramics with aligned porosity include freeze casting, impregnation with a ceramic slurry of an aligned sacrificial template, phase inversion and co-extrusion of ceramic and sacrificial pore-former [23–26]. Recently, micro-fabrication was used to produce supported molten-salt membranes with pores of ~10^2 μm diameter aligned with the direction of desired gas transport (by laser-drilling arrays of parallel pores into the closed end of a ceramic tube). In one example where the self-assembly of electronically-conductive Ag dendrites within the parallel pores was stimulated by gas permeation, an exceptionally high CO_2 flux (~1.25 ml $min^{-1}.cm^{-2}$ at 650 °C) was achieved [27]. By comparison with a membrane having a sinuous pore network in the same work, the directionally-aligned pores were considered to be advantageous for performance. However, it is very challenging to generate dense arrays of micron-scale pores in ceramics with 3D micro-fabrication techniques, due to *e.g.* the limited spatial resolution of additive manufacturing or laser-drilling approaches. Directional-solidification methods provide an alternative means to prepare ceramics with aligned microstructures (*viz.* certain families of eutectics), giving rise to samples with 1–10^4 mm^2 cross-section areas and characteristic phase sizes from 0.1 to 10 μm in a direction transverse to the growth axis [28,29]. In the case of fibrilar eutectics, the technique provides a quasi-hexagonal array of highly aligned fibres of the minority phase, parallel to the growth direction, embedded into a single crystal of the majority phase. In principle, such a structure provides pores with a nominal tortuosity of unity (after removal of the fibre phase). Additionally, the structure should also afford a high interfacial area between the support and the molten salt, which may be important depending on the permeation mechanism.

The quality of the alignment, and the finesse and homogeneity of the microstructure afforded by directional solidification of eutectics far surpass what is observed in membranes produced by other pore-aligning methods, such as freeze-casting or phase-inversion. In hollow fibres produced by phase inversion, for instance, a bimodal radial distribution of pore size is usually found, with finger-like pores in a relatively large diameter range (≥4 μm, up to several tens) presenting a quite irregular shape and small pores (diameter below 1 μm) forming sponge-like regions [14,25].

Thus, here we show how fibrilar eutectics can be used to produce a molten-salt membrane support with geometrical and microstructural properties difficult to achieve by other methods. We employed the laser floating zone (LFZ) technique of directional solidification [29], through which the high-melting-point oxides employed in supported molten-salt membranes may be melted and solidified with no need of a crucible, yielding mechanically strong, rod-shaped eutectic bi-crystals with no porosity. The minority phase (fibres) was removed by acid etching to produce a matrix with a highly dense array of aligned pores on a length scale difficult to achieve by other methods (<10^1 μm). The porous matrix was then employed as a support for molten carbonate infiltration; CO_2 permeation experiments provided an exceptionally high CO_2 permeability above 700 °C, a result that can be attributed to the optimisation of the pore microstructural properties, namely low tortuosity factor, high pore density and high specific interfacial area.

2. The ZrO_2–MgO phase diagram and materials properties

The desirable characteristics of a membrane support impose restrictive conditions on materials selection for directional solidification. First, fibrilar eutectic growth requires that the proportion of the minority phase does not exceed ~29 vol% [29]. Otherwise, lamellar growth will in general occur. Second, coupled growth must take place in order to achieve an ordered, colony-free, microstructure. Third, the minor phase (fibres) must be easily etched without affecting the matrix that will become the membrane support and said matrix should be an oxygen-ion conductor. Finally, thermal expansion compatibility is required between the materials forming the matrix and the fibres, to *e.g.* avoid cracks on cooling during solidification.

After exploring different systems, we found the ZrO_2–MgO system to be a suitable combination of oxides as it fulfils the requirements listed above. According to the ZrO_2–MgO phase diagram (PD) (Fig. S1, ESI) [30], a eutectic point exists around 50:50 mol% ZrO_2:MgO with $T_e \approx$ 2170 °C. A more precise determination of the eutectic composition yielded 47:53 mol% ZrO_2:MgO [31]. At the eutectic temperature, the

liquid crystallizes in the form of a quasi-hexagonal lattice of micron-sized MgO fibres embedded within a magnesium-stabilised zirconia (MgSZ) cubic phase with ~20% Mg^{2+} content [31,32]. The incorporation of Mg^{2+} ions within the initially monoclinic ZrO_2 phase introduces a corresponding number of oxygen vacancies that stabilise MgSZ in its cubic form and provide ion-conducting behaviour. The volume proportion of the MgO fibres in the eutectic predicted by the PD is 28.7%, close to the limit between fibrilar and lamellar growth. The linear thermal expansion coefficients (TEC) of MgO and MgSZ match relatively well: the TEC of MgO varies from 11 to 14 x 10^{-6} K^{-1} between 300 and 1000 K [33], which is close to the TEC of cubic zirconia-related materials, 10.5–11 x 10^{-6} K^{-1} for YSZ (8 mol% Y_2O_3 doped ZrO_2) in the same temperature range and of the order of 11.2 x 10^{-6} K^{-1} for (3 mol% YSZ)$_{0.8}$-$MgO_{0.2}$ [34]. Directionally solidified MgO-MgSZ also shows suitable flexural strength, with values ranging from 150 to 450 MPa [35,36]. This hints towards the possibility of safely producing crack-free bicrystals during cooling after laser-assisted solidification. Moreover, although lower than YSZ ($\sigma \gtrsim 10^{-2}$ S cm^{-1} at 1020 K) [37], which is routinely employed in supported molten-salt membranes, MgSZ still has a good ionic conductivity of 2.3 x 10^{-3} S cm^{-1} at 1000 K [38]. Finally, MgO is highly soluble in hydrochloric acid whereas MgSZ is not, so that the fibres can be eliminated by acid-etching without significantly affecting the matrix.

Other material combinations might be suitable, provided that they fulfil the requirements listed above. Preliminary work is being carried out with the YSZ-MgO and $Zr_{1-x}Ce_xO_2$-MgO eutectics, although in the latter case, thermo-mechanical stability may be an issue.

3. Materials and methods

Rods of 47:53 mol% ZrO_2:MgO were directionally solidified using the LFZ method, where a drop of a sample is melted by focussing a high-power CO_2 laser on a small volume of the feedstock material as it moves vertically [29]. To prepare the feedstock rods, commercial powders of ZrO_2 (Aldrich, 99%) and MgO (Alfa Aesar, 99.99%) were mixed in the appropriate amount, isostatically pressed for 3 min at 200 MPa and sintered at 1500 °C for 12 h in an open furnace. Rods of ~80 mm length were melted and solidified in air using 80–100 W of a CO_2 laser (λ = 10.6 μm) as a heating source at rates varying between 10 and 300 mm h^{-1}. The final diameters of the rods were between 1.2 and 1.5 mm.

Transverse and longitudinal cross-sections of the processed rods were cut and polished for scanning electron microscopy (SEM) and electron dispersive X-ray spectroscopy (EDS) in a Field Emission SEM microscope (MERLIN, Carl Zeiss). The volumetric phase proportion of the fibres and the matrix in the eutectics was calculated by greyscale analysis of transverse-section micrographs, performed by means of Digital Micrograph, Gatan Inc. software.

Crushed portions of the rods were used for X-ray diffraction (XRD) experiments, which were carried out on a Rigaku D/max 2500 diffractometer with Cu K_α radiation working at 40 kV and 100 mA. Data were collected in a step mode ($\Delta 2\theta = 0.03°$) and a counting time of 3 s per step.

Sections of the rods were acid-etched by immersion in a 1 M solution of HCl in distilled water at 60 °C. The sample weight was measured to check the degree of etching, which was determined from the weight loss relative to the weight proportion (21%) of the MgO fibres in the MgSZ-MgO eutectic. Achieving mass losses above 80% of the MgO phase required treatments lasting ≥20 days.

An as-etched eutectic sample was prepared for X-ray nano-CT by use of an A Series/Compact Laser Micromachining System (Oxford Lasers) with an embedded Class 4 laser with 532 nm wavelength. A small eutectic sample (~1.5 mm dimensions) was epoxy-glued to the end of a stainless-steel dowel which was laser-lathed to a fine cylinder with a diameter of approximately 40–50 μm. This procedure is detailed in Ref. [39].

X-ray nano CT was performed using a Zeiss Xradia 810 Ultra (Carl Zeiss), which has a micro-focus rotating Cr anode set at 35 kV and 25 mA. A pseudo-parallel X-ray beam was quasi-monochromatized at Cr K_α (5.4 keV) by a reflective capillary condenser, before impinging on the sample and subsequently being re-focused by a Fresnel zone plate onto a CCD detector. Scans were performed in absorption-contrast mode with a field-of-view of 65 × 65 μm, operated with a binning of 2, yielding a voxel dimension of ~126 nm. X-ray nano-CT projections were taken from -90 to +90° at 1101 regular angular increments, each with an exposure time of 64 s, the resultant projections of which were reconstructed in XMReconstructor (Carl Zeiss) using a traditional filtered back-projection algorithm.

The X-ray tomogram was imported into Avizo (Thermo Fisher Scientific) and first underwent a transform to align the pore direction with the *z*-direction of the tomogram. Subsequently, this transformed volume underwent a shading correction to compensate for grayscale gradients across the entire 3D volume. A sub-sample was removed from within this corrected, transformed volume with dimensions of ~25.2 × 25.2 × 50.5 μm, giving an overall sampled volume of ~32,100 μm^3. The sub-volume underwent a second shading correction before an Unsharp Masking filter (3D, edge size 5 pixels and edge contrast set to 0.5) and a Gaussian filter (3D, kernel size 5 pixels and standard deviation set to 1) was applied, to better highlight the pore-solid boundaries. The resultant sub-volume was then segmented using machine-learning-based freeware, Ilastik [40], with user training provided on one central slice. Subsequently, user interaction with several other slices was used to give an updated binary segmentation that was deemed to match the processed volume well by eye. Note that the MgO and MgSZ phases were not distinguishable at 5.4 keV and at this pillar width, such that the binary segmentation represents a delineation between porosity and a composite phase made up of both residual MgO and the MgSZ matrix.

Volume calculations for the two phases were made using simple voxel counting from the binarised dataset. All surface areas were calculated by generating a surface mesh (constrained smoothing) and summing the areas of the resulting mesh elements. Volume-specific surface areas were calculated by dividing by the pore volume in question. This analysis was carried out for the entire dataset, as well as for datasets including only the isolated, non-isolated, *x*-connected, *y*-connected and *z*-connected porous components. The isolated (and thus by subtraction, non-isolated) components were accessed by a simple 3D 'Border Kill' algorithm which removed all objects that had an interface with the external boundary. The *x*-, *y*- and *z*-components of the porous phase were accessed using the 'Axis Connectivity' module in the *x*-, *y*- and *z*-directions, respectively.

To assess the pore parallelism, linear regression was performed in Python. To separate any adjoined pores, two successive binary opening processes were performed. Binary opening consists of an erosion step (removal of outermost pixels), followed by a dilation step (the converse process). The purpose was to maintain quite closely the shape of the original structures, but also to break any small connections between larger bodies. Due to either small irregularities in the segmentation, or small connections in the true structure, individual fibrils may begin this process with several small connections between them, making them appear numerically as one feature. After binary opening the large structures should no longer be connected. Indeed, after two successive operations, 140 separate pores were identified. Before regression, each pore was made smaller with two more erosions. As before, this maintained the shape but reduced the overall size of the data set. Two linear regressions were performed on each pore, one for the *x*-component versus the *z*-component and the other for the *y*-component versus the *z*-component.

The total electrical conductivity of the samples was calculated from resistance measured by impedance spectroscopy (SI 126.0 Schlumberger Instruments). The spectra were recorded by exciting the samples with amplitude voltages of 100 or 50 mV, from 1 to 10^6 Hz and sampling 10 frequency points per decade. Nyquist plots were used to extract the total resistance of the respective samples, excluding the electrode

contribution [41]. For the MgSZ-MgO eutectic samples, the electrodes were made with Pt paste and cured at 900 °C for 0.5 h. The conductivity of the carbonate mixture was measured in a small Al_2O_3 crucible (capacity ~3 mm^3) with Pt sheets as electrodes. The Al_2O_3 crucible was filled with the carbonate mixture, heated above the eutectic temperature to eliminate bubbles in the mixture and then cooled to room temperature with the Pt-sheet electrodes in place. For the MgSZ samples infiltrated with carbonates, Au-paste electrodes were painted and cured at a temperature below the melting temperature of the carbonates. Infiltration of the carbonates into the porous MgSZ for conductivity measurements was made in ambient air. For that purpose, a mixture of Li_2CO_3, Na_2CO_3 and K_2CO_3 carbonates in the ternary eutectic proportion (42.5/32.5/25 mol%, respectively) was deposited in compacted powder form on top of the MgSZ sample and heated above the eutectic temperature (397 °C) to allow the carbonates to melt and infiltrate the pores by capillarity. All prepared samples were held against spring-loaded Pt sheets welded to Pt wires with the entire arrangement located in a cylindrical furnace for measurements. All measurements were made in stagnant air with temperature monitored with a K-type thermocouple located near the sample.

Supports for permeation experiments were infiltrated with the ternary eutectic mixture of alkaline carbonates following a similar procedure as for conductivity measurements. High-temperature carbon dioxide permeation experiments were carried out in a custom-made membrane reactor, operated at atmospheric pressure. The permeation apparatus comprises two chambers, an internal feed-side chamber and an external permeate-side chamber, enclosed by the membrane and a quartz tube, respectively. The details can be found elsewhere [42]. For an accurate temperature determination, a thermocouple was placed as close as possible to the membrane, with the membranes pasted to a YSZ tube using Au paste. The feed gas was 50 mol% CO_2/25 mol% N_2/25 mol % O_2 (feed-side inlet) and the sweep gas was high-purity Ar (permeate-side inlet). Different inert gases (N_2 on the feed side and Ar on the permeate side) were used to detect transmembrane leaks, *i.e.* if N_2 was detected significantly above background levels the experiments were stopped as a leak was apparent. All gases were provided and certified by BOC. The flows on both the feed and permeate sides were maintained at a total gas flow rate of 30 ml min^{-1} (NTP). Residence time distribution experiments (not shown) for both the feed- and permeate-side chambers indicated that the membrane was exposed to the outlet conditions as there was good gas mixing on both sides. The outlet permeate-side gases (*e.g.* CO_2, N_2 or O_2) were analysed using a mass spectrometer (HIDEN, HALO 100-RC). The superposition of the CO and N_2 signals in the m/z= 28 channel was accounted for and the N_2 flow was corrected accordingly. The CO_2 concentration in the permeate-side outlet stream was also analysed using IR (XTREAM-Enhanced General-Purpose Process Gas (XEGP) Analyser, Emerson Process Management Limited) in series with and after the mass spectrometer. Both the IR analyser and the mass spectrometer were calibrated before each experiment to account for systematic errors and instrument drift, by flowing N_2 and CO_2 gases of certified mole fraction. The mole fraction of the calibration gases was chosen to be as close as possible to the expected permeate-side mole fraction during the permeation experiments. Argon was used for background calibration for all instruments. The flow of gases to the permeation apparatus was controlled by mass flow controllers (Brooks Smart II). Flow rates were confirmed at the permeate-side outlet using a Varian digital flow meter (1000 series). From the measured permeation rate y ($ml.min^{-1}$) of each gas, the flux J ($ml.min^{-1}.cm^{-2}$) is defined as $J = y/A$, where A is the membrane area.

Raman spectroscopy of the matrix before and after etching as well as after permeation experiments (as a molten carbonate support) was performed in a DILOR XY spectrometer equipped with a liquid-nitrogen cooled CCD detector. The 496.5 nm line of an Ar^+-ion laser, model Coherent Innova 305, was used as excitation source. A 50X microscope objective lens of an Olympus BH-2 microscope was used both for excitation and dispersed light collection. The same microscope was used to record optical images of the samples.

4. Microstructure and conductivity of the supporting oxide

MgSZ-MgO eutectic rods were directionally solidified at different processing rates to test the influence of the solidification rate on phase microstructure. Rates above 50 mm h^{-1} resulted in colony-like microstructures (Fig. S2, ESI), such that we limited our study to 25 mm h^{-1} processing rates (Fig. 1).

The as-grown rods consist of a quasi-hexagonal eutectic pattern of MgO fibres embedded in an MgSZ matrix (EDS analysis confirmed the fibres are 100% MgO whereas the composition of the matrix suggests that it is an MgSZ phase (Fig. S3, ESI)). The fibre spacing λ of fibrilar eutectics depends on the growth rate v as per the Hunt-Jackson law $\lambda^2 v = C$ [43], where C is a constant for each system, which depends essentially on the phase diagram and the diffusion coefficient of the ions in the melt. For the MgSZ-MgO system with $v = 25$ mm h^{-1}, the fibre diameter was ~1 μm and the spacing was ~2 μm [32,36]. The phase proportion was determined from image analysis to be 29 ± 1 vol% of MgO phase, in good agreement with the PD. The volume percentage of the fibre phase determines the maximum porosity of the matrix after etching, the actual porosity being diminished with respect to the maximum value by the degree of unsuccessful etching. In our case, MgO weight losses between 80 and 90% were achieved, resulting in a support porosity in the 22.4–27% range. A digital image of the transverse section of a rod after etching is shown in Fig. 2, confirming a tightly packed array of fine diameter (~1–1.5 μm) pores.

To avoid the influence of nearby MgO fibres in the determination of the matrix composition, EDS analyses were also performed in etched samples and yielded a Mg cation content of about 16–17% in the matrix, which is below the prediction from the PD (~20%) (Fig. S3, ESI). This difference can be attributed to the prolonged acid treatment of 2–3 weeks, an effect also observed by Sato et al. in bulk MgSZ samples [44]. Crushed portions of the samples were also analysed by XRD (no attempt was made to analyse the phase composition, as preferential orientation is expected in crushed single-crystals). XRD patterns were fitted with two phases (Fig. S4, ESI), a fluorite phase belonging to the MgSZ matrix, with a(MgSZ) = 5.058(1) Å, and a rock-salt phase, accounting for the MgO fibres, with a(MgO) = 4.213(1) Å. Both values agree, within error, with those reported in the literature for this system and with the matrix composition determined by EDS [45].

4.1. X-ray nano-CT of the porous matrix

As the MgSZ matrices obtained by etching the MgSZ-MgO eutectics are to be used as supports for molten carbonate, the 3D microstructure of the matrices was studied by X-ray nano-CT to characterise the porosity in terms of phase fraction, isolation, connectivity and alignment. Fig. 3 shows 3D reconstructions of the X-ray nano-CT data from the thinned pillar of an etched rod, depicting the solid phase (Fig. 3a) and the pores of the matrix (Fig. 3b) prior to carbonate infiltration. In Fig. 3c, 'families' of interconnected pores are shown, with 'families' uniquely coloured.

Table 1 shows the analysis of the full set of pores, the closed and open pores, and the pores percolating between each set of opposite faces (x-, y- and z-direction). A porosity of ~20.7% was identified from the entire analysed volume (~32,100 μm^3), with a volume-specific internal surface area of ~0.9 μm^{-1} (~0.8 μm^{-1} for z-percolating pores). The 20.7% porosity is slightly below the range determined from weight loss after acid treatment in these samples (22.4–27%), a discrepancy that can be attributed to the different nature of the techniques used for each determination. Weight loss is a macroscopic measurement that averages composition or microstructural inhomogeneity across the sample, whereas X-ray nano-CT gives the porosity of a small sample volume and depends on the segmentation used to define the limit between pore and solid phases. Most of the pores were connected to at least one plane of

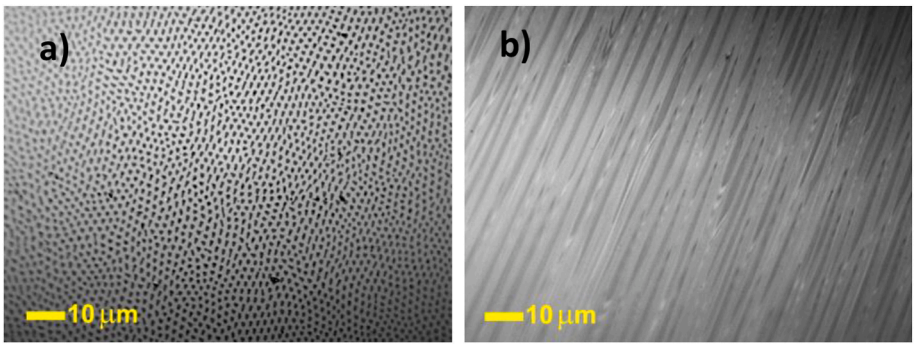

Fig. 1. Optical micrographs of the: **a)** transverse and **b)** longitudinal sections of an MgSZ-MgO eutectic rod processed at 25 mm h^{-1}. In this context, transverse and longitudinal mean perpendicular to, and containing the growth axis, respectively. The latter coincides with the fibre direction.

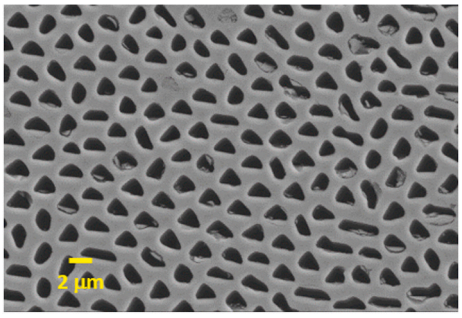

Fig. 2. Electron micrograph of the transverse section (perpendicular to the growth axis) of an MgSZ-MgO eutectic solidified at 25 mm h^{-1} after etching, depicting an array of micrometric pores (dark grayscale) embedded into the MgSZ matrix (light grayscale). Note that some of the fibres are occluded by polishing material due to polishing after etching.

the analysed volume, leaving a negligible proportion of closed pores (0.24% of entire volume), consistent with the etching procedure. Although no pores percolated in the '*x*-direction', just over a third percolated in the '*y*-direction' and importantly for our aims, ~76% percolated in the '*z*-direction' (growth direction), across the ~50 μm section of the etched sample.

As can be seen in Fig. 3c, most of the pores in the analysed volume are isolated from each other, a majority of them percolated between the top and bottom faces of the analysed volume. However, it can also be seen that there are some 'families' of connected pores, which arise from fibre coalescence in a transverse direction. This is not unusual in fibrilar eutectics; pores with irregular shape in a transverse direction can be seen in the electron micrographs depicted in Fig. 2, although in that case only occasional fibre coalescence can be observed.

The results of the pore alignment calculations can be seen in Fig. 4. As can be clearly seen, the fact that both the *x* and *y*-components of all the fibrils are very internally similar for each pore is testament to their parallelism. The small degree of scatter is a representation of their minor deviations from being fully parallel with one another, which constitutes a variation between -9.9 and 0.2°, and -5.1 and 4.7°, in the *x*- and *y*-direction, respectively. The fact that the scatter is not centred about zero in the *x*-direction is simply an artefact of the initial, imperfect transformation used to align the pores to the *z*-direction. Since the range of deviations is 9.7 and 9.8°, in the *x*- and *y*-direction, respectively, there is no evidence of anisotropy in the measured deviation from parallelism.

The slight pore misalignment is attributed to the curvature of the solidification front during melting and is inherent to the LFZ technique. The macroscopic solid-liquid interface is frequently concave towards the melt [29], and the alignment of the eutectic grains proceeds perpendicular to this interface so that some deviation of the fibre direction from

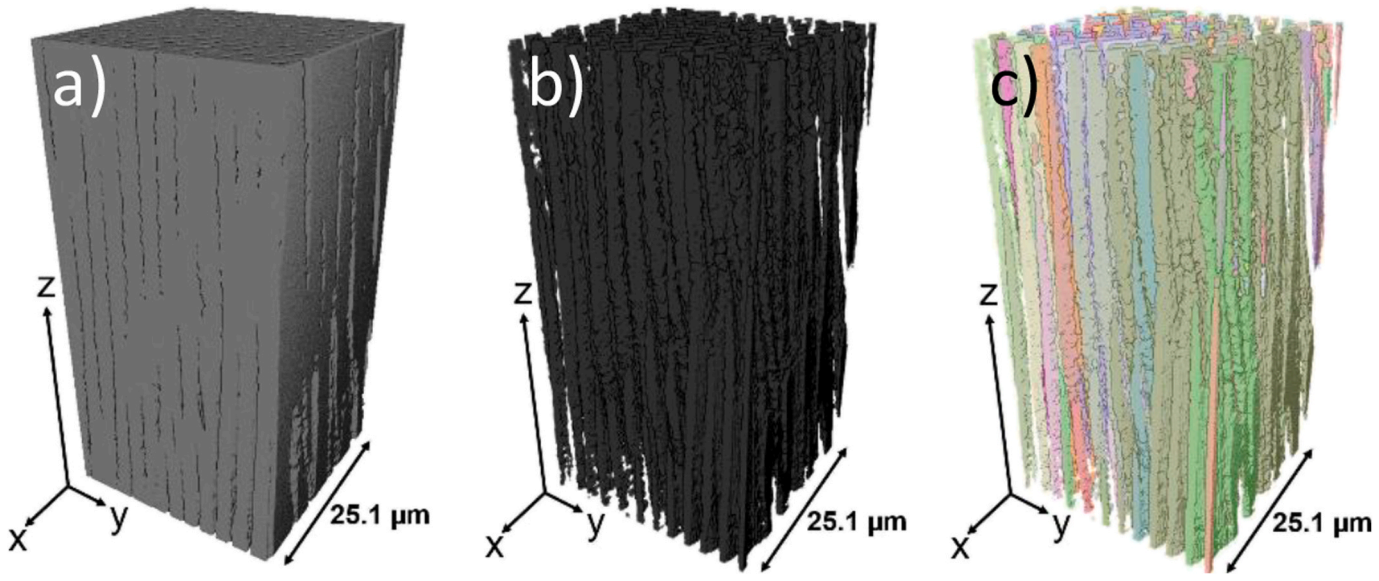

Fig. 3. X-ray nano-CT volume renderings of the sample prior to carbonate infiltration. **a)** Image of solids, in which porosity in the MgSZ matrix is transparent. **b)** Image of all pores, in which the solids are removed, and the alignment of pores can be clearly observed; **c)** Image of individual pore 'families' (pores that have coalesced) uniquely coloured.

Table 1
Extracted metrics from X-ray nano-CT tomogram of thin MgSZ pillar of ~32,100 μm^3 total volume.

Porosity type	Absolute pore Volume (μm^3)	Fraction of total volume	Fraction of pore volume	Absolute Surface Area (μm^2)	Volume-specific Surface Area (μm^{-1})
All	6662	20.7%	100.0%	31356	4.7
Closed	76	0.2%	1.1%	632	8.3
Open	6586	20.5%	98.9%	30722	4.7
x-percolating	0	0%	0%	0	0
y-percolating	2467	7.7%	37.0%	11104	4.5
z-percolating	5077	15.8%	76.2%	23706	4.7

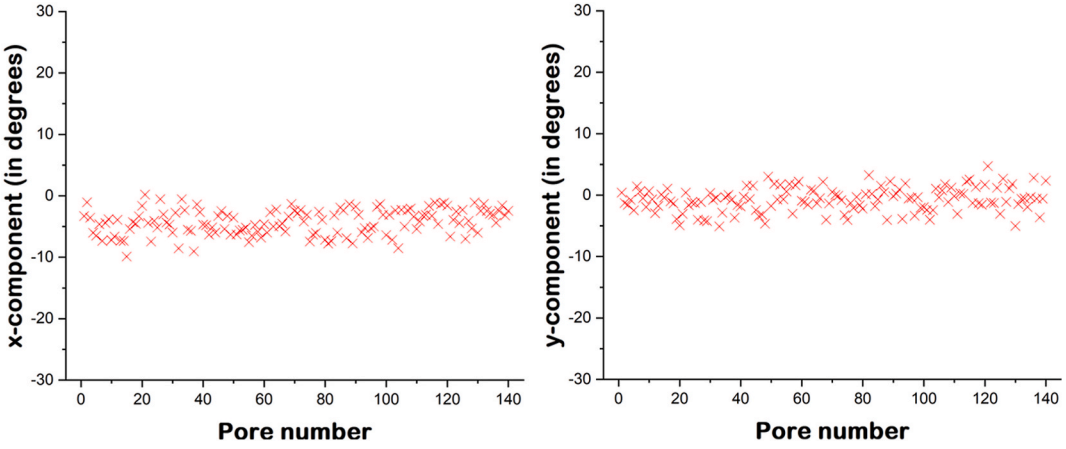

Fig. 4. Regression analysis of the directions of all processed pores from the X-ray CT tomogram, **a)** showing the variation in the *x*-component **b)** showing the variation in the *y*-component. All values are in degrees and relative to the *z*-axis after initial coarse alignment of the volume.

the axis of the solidified rod is commonly encountered. For typical support diameters and thicknesses above ~1 mm, misalignment may result in a significant reduction of the proportion of pores percolating between both sides of the membrane. Therefore, supports that are as thin as possible are desirable.

4.2. Total electrical conductivity of an infiltrated rod

According to Equation (3), conductivity of both the solid and molten carbonate phases impact performance. Therefore, Fig. 5 shows the total electrical conductivity of the ternary eutectic carbonate mixture (in an Al_2O_3 support) (red circles), carbonate-infiltrated MgSZ rod (blue triangles) and MgSZ-MgO eutectic sample (green squares), obtained from impedance spectroscopy measurements up to 460 °C (for the carbonate mixture), 600 °C (for carbonate infiltrated MgSZ) or 850 °C (for MgSZ-MgO eutectic).

The conductivity observed for the MgSZ-MgO eutectic is identical to the one reported in Ref. [38]. The activation energy for σT in the high temperature end (fit using data between 580 °C and 850 °C) was 1.73 ± 0.01 eV. Regarding the samples infiltrated with carbonates, in both cases the conductivity increased at the carbonate melting temperature (~400 °C), as expected [46], but the conductivity above this temperature is 65 times larger for the molten carbonates than for the MgSZ-carbonate infiltrated sample. This may be due to the combined effect of several factors: the most evident one is that the pore proportion is at most 29% vol, according to the ZrO_2–MgO PD, further limited to ~22.4–27% because of incomplete etching. Other factors come from pores not percolating between both sides of the support, either because they are half-closed or because they end at the rod side surfaces instead of at its bases where the electrodes are attached. The latter aspect arises from pore misalignment, as found by X-ray nano-CT, and may be significant at the ≥2 mm length of the sample used in conductivity experiment. As explained above, some misalignment is unavoidable in LFZ processed materials, owing to the curvature of the solidification front. In any case, from Fig. 5, the total electrical conductivity *via* the molten carbonate

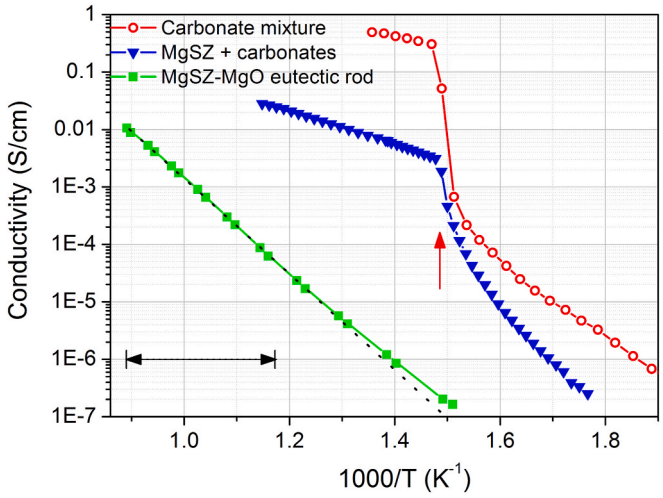

Fig. 5. Total electrical conductivity of the eutectic mixture of carbonates (red circles), MgSZ porous matrix infiltrated with carbonates (blue triangles) and MgSZ-MgO as-grown eutectic (green squares). The dotted line is calculated with the parameters obtained from the fit of the expression $\sigma T = A\exp(-E_a/kT)$ to the experimental data of the MgSZ-MgO sample in the temperature range 580 °C–850 °C (indicated with black arrowed-segment). The melting temperature of the carbonates (~400 °C) is marked with a red arrow. (For interpretation of the references to colour in this figure legend, the reader is referred to the Web version of this article.)

path is still much larger than the conductivity of oxide ions *via* the MgSZ oxide phase in the temperature range of interest, as expected for the combination of a solid oxide and a molten salt typical of supported molten-salt membranes.

5. Membrane assembly and permeation experiments

As-grown rods were ~1.5 mm diameter and ~80 mm long. Each rod was cut into ~2 mm-long slices that were acid-etched for ≥20 days to dissolve the MgO fibres. To increase the effective membrane surface area, seven MgSZ porous slices were inserted into circular holes (~1.6 mm diameter) which were laser-drilled in a 500 μm-thick YSZ ceramic plate. Ceramabond 885 was used to secure the rods within the plate (Fig. 6).

The membrane formed by the seven etched rods was pasted to a 11-mm-diameter, 250-mm-long YSZ tube. A pellet of pressed carbonate powders containing the quantity required to fully infiltrate the pores, was deposited on top of the support, then the tube was inserted into the membrane reactor, which was placed inside the furnace. The temperature was first increased from room temperature to 495 °C at 1 °C.min^{-1} under 30 ml min^{-1} flow of composition 50%CO_2/25%N_2/25%O_2, both at the feed and permeate side inlets (this procedure ensures that the carbonates do not decompose during heating). The membrane was held for several hours at 495 °C to allow the carbonates to fully infiltrate the pores by capillarity. Then, the sweep gas was switched to 30 ml min^{-1} of high-purity Ar (to generate a driving force for CO_2 permeation) and the temperature was increased first to 565 °C and then from 565 to 815 °C in steps of 50 °C, with 7 or 10 h of holding time at each temperature step and 1 °C.min^{-1} ramp between steps.

Fig. 7 shows the temperature dependence of the CO_2 and O_2 fluxes, taking the sum of the seven rod sections (including solid plus molten phase) as the effective membrane area, $A = 12$ mm^2. Average flux values are determined after 7 or 10 h of dwell time at each temperature, except at 815 °C, as CO_2 permeation showed a steep decrease after only 1 h at that temperature (see Fig. S5 in the ESI). This behaviour is discussed below. Since there is no obvious transport mechanism to enable significant N_2 permeation, the detection of a significant N_2 flux at the permeate-side outlet can be attributed to a leak. The N_2 flux in the present measurements was always around the background level of N_2 in the analytical instrumentation, so that we may safely consider that leaks are negligible in our membrane. Therefore, the CO_2 to N_2 selectivity across all temperatures was very high, as expected for supported molten-salt membranes [47]. The O_2 flux, on the contrary, is above the background level beyond 700 °C, implying that there is O_2 permeation through the membrane, discussed below.

Fig. 8 shows the CO_2 (P_{CO2}) and O_2 (P_{O2}) permeabilities (in mol.m^{-1}.s^{-1}.Pa^{-1}) obtained from the corresponding flux through the expression $P = J.t/(p_i\text{-}p_o)$, where t is the membrane thickness (here, approximated by the length of the rods) and p_i, p_o are the CO_2 or O_2 partial pressures at the feed and permeate sides, respectively. The CO_2 permeability is 0.83x10^{-10} mol m^{-1}.s^{-1}.Pa^{-1} at 765 °C and 1.41 x 10^{-10} mol m^{-1}.s^{-1}.Pa^{-1} at 815 °C, much higher than in ceramic membranes based on YSZ as ionic conducting phase (10^{-11} mol m^{-1}.s^{-1}.Pa^{-1} at 850 °C in Ref. [4] and 7.69 x 10^{-13} mol m^{-1}.s^{-1}.Pa^{-1} at 650 °C in Ref. [48], despite the lower conductivity of MgSZ compared to YSZ, and of the same order as the best performing membranes reported to date using SDC supports and different types of pore-formers [14,16].

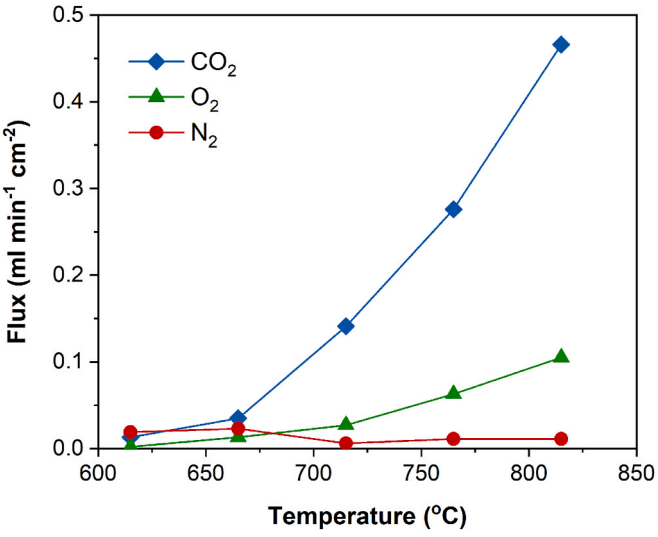

Fig. 7. CO_2, O_2 and N_2 fluxes obtained in the permeation experiment of the carbonate-infiltrated MgSZ membrane.

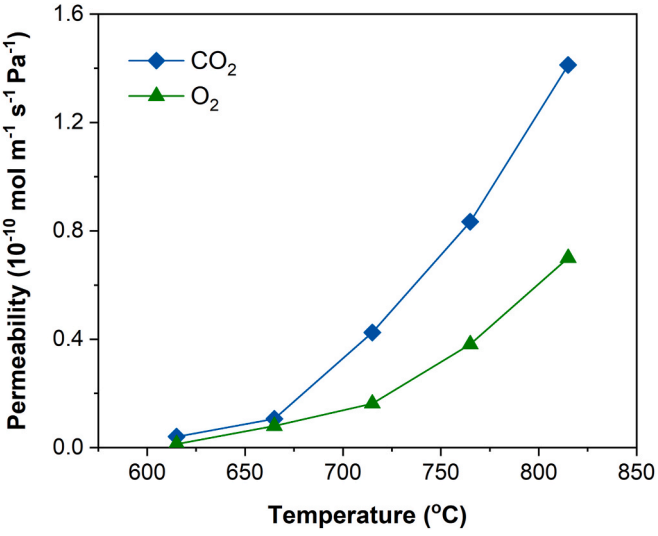

Fig. 8. CO_2 and O_2 permeabilities of the carbonate-infiltrated MgSZ membrane.

Figs. 7 and 8 suggest that the permeation of both CO_2 and O_2 responds to a thermally activated mechanism. An Arrhenius fit of the permeability data yields activation energies of 1.5(2) and 1.3(1) eV for CO_2 and O_2, respectively, which are in reasonable agreement with the activation energy for the oxygen ion conduction of the MgSZ matrix

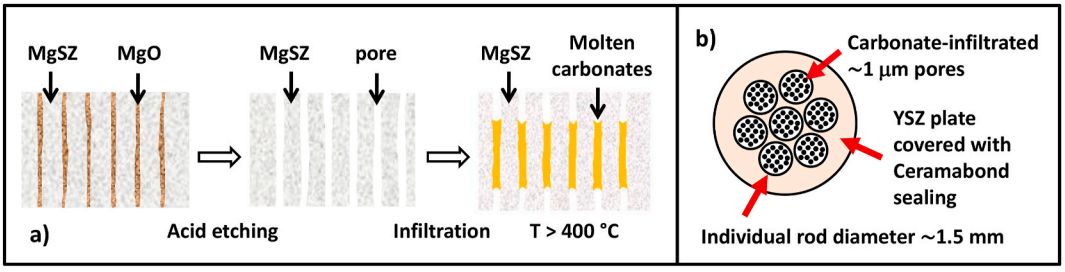

Fig. 6. Schematics showing **a)** etching and infiltration steps applied to the as-grown MgSZ-MgO eutectic rods, and **b)** the arrangement of seven infiltrated transverse rod portions forming the membrane to be used in the permeation experiment. For the permeation experiments, carbonates were infiltrated after the seven etched rods were pasted to the YSZ plate.

determined in Section 4 and in previous reports ($E_a(\sigma_{so}T)$= 1.73(1) eV) [34].

The steep decrease of the permeation flux after 1 h at 815 °C (Fig. S5, ESI) is intriguing. It cannot be attributed to a leak or breaking of the membrane, because that would likely result in an increase in CO_2 flux, contrary to observation. To understand that behaviour we analysed by Raman spectroscopy and XRD the evolution of an infiltrated sample submitted to a similar thermal treatment as the membrane (reaching 800 °C). The Raman spectra shown in Fig. S6 of the ESI shows that after the treatment the matrix has evolved from the initial cubic-fluorite phase to a superposition of cubic, tetragonal and monoclinic phases of ZrO_2, with undetermined Mg content, a behaviour that is attributed to phase segregation. In fact, as the PD of the ZrO_2–MgO shows (Fig. S1, ESI), the cubic phase of MgSZ is not stable below 1400 °C and segregation between tetragonal or monoclinic MgO-poor ZrO_2 and MgO phases is expected in that temperature range, as previously reported [49]. MgO is Raman-inactive, so that the presence of this phase cannot be detected by this technique. XRD of the same sample, shown in Fig. S7, further showed the presence of a fluorite-like phase with a lattice parameter suggesting a cation composition close to that of the metastable $Mg_2Zr_5O_{12}$ phase [50]. Segregation, however, requires annealing times of the order of 24 h at 1200 °C in bulk MgSZ (Fig. S8) [49], such that it is surprising that it occurs in just 1 h at 815 °C during the permeation experiment. We have found that the fast segregation is a consequence of the porous character of the sample used to fabricate the membrane: the same treatment in a non-etched sample did not affect the MgSZ structure whereas segregation was seen after just 1 h at 800 °C in an etched, non-infiltrated sample. The support instability above 800 °C limits its applicability at such high temperatures. On the other hand, the membrane was held for 10 h at 765 °C with no hint of failure or decreasing performance, so we can assume that 765 °C is still a safe operating temperature.

The behaviour of an infiltrated MgSZ support at high temperature was further investigated to elucidate the possible formation of alkali-metal zirconates through reactions such as $ZrO_2 + Li_2CO_3 \rightleftarrows Li_2ZrO_3 + CO_2$, as observed in Ref. [8]. Although no hint of either m- or t-Li_2ZrO_3 was found by Raman spectroscopy, a weak peak was detected at 23.3° in the XRD pattern shown in Fig. S7 that cannot be assigned to any of the already mentioned phases and is close to the main peak of t-Li_2ZrO_3, expected at 23.1°. The intensity of the peak at ~23° is close to the detection limit of X-ray diffraction but its likely attribution to Li_2ZrO_3 suggests that the appearance of this phase has to be considered when dealing with zirconia-derived phases.

6. Discussion

We note that the measured CO_2 permeability is much higher than those reported for YSZ-based supported molten-salt membranes [4,48], despite the conductivity of MgSZ being approximately one order of magnitude lower than that of YSZ. The high permeability therefore may be attributed to the improved pore characteristics: good connectivity, alignment along the permeation direction, very homogeneous pore size and high specific surface. The ordered pore distribution also reduces the ceramic support tortuosity factor.

To take advantage of the high permeability observed in the present material, bigger samples are needed. Other available solidification methods that allow larger ingots may be used [32,51]. Alternatively, a more cost-effective approach could be to coat the surface of an appropriately designed ceramic (either tube or plate) with the solidified eutectic coating [52,53].

The high CO_2 flux reported in Fig. 7 warrants some discussion. Experimental values can be compared with predicted ones by substituting in Equations (2) and (3) the appropriate values of CO_2 partial pressures, membrane thickness and carbonate and MgSZ conductivities. For the solid oxide phase [$(\phi/\tau)_{so}\sigma_{so}$], we use the conductivity of the MgSZ-MgO eutectic (see Fig. 5), since MgO is non-conducting and the eutectic presents, *a priori*, the same volume fraction and tortuosity factor as the matrix used for the membrane. For the carbonate phase, we take the conductivity of the molten carbonates reported in Fig. 5 and, to compare with the best possible situation, assume an optimal microstructure in which all the pores are perfectly aligned and contribute to permeation, i.e. $(\phi/\tau)_c$ = 0.29/1. The actual value will be lower, but this will not be relevant since the total conductivity will be limited by that of the solid oxide. With these assumptions the CO_2 flux expected at 800 °C would be ~1.8 x 10^{-2} ml $min^{-1}.cm^{-1}$, which is ~25 times lower than the observed value.

To explain this discrepancy, we first consider the possibility of σ_{so} being higher in the membrane than in the as-grown eutectic. As explained in Section 4, the Mg cation content of the MgSZ matrix found by EDS analysis (17%) is below that predicted by the ZrO_2–MgO PD (~20%), a difference that has been attributed to the leaching effect of the acid treatment. Since the conductivity of $Zr_{1-x}Mg_xO_{2-x}$ presents a maximum around x= 0.08–0.09 [54,55], the observed reduction of the Mg content after leaching might enhance the conductivity. The reduction in Mg content, however, is too low to account for the increase of σ_{eff} that would be required to explain the high flux.

We then must consider an enhancement of the CO_2 flux related to the presence of O_2 in the feed gas (pO_2= 0.25 atm), an experimental condition not typically investigated for nominally oxygen-ion conducting supports. According to Ref. [5], both the CO_2 flux through the molten carbonates and the O_2 flux through the solid oxide phase might be enhanced in the presence of O_2 if the solid oxide were a mixed ionic-electronic conductor. Although there are no reports in the literature about *p*-type conductivity of MgSZ at high oxygen activities, we may take data from Y_2O_3 doped ZrO_2 (YSZ or TZP) as a reference, where the hole conductivities at 1 atm and ~700 °C are between 5 x 10^{-7} and 3 x 10^{-6} S cm^{-1}. Looking at the expression for the CO_2 flux given in Ref. [5], we can say that with the likely very low hole conductivity of MgSZ, the expected increase of the CO_2 flux derived from the presence of O_2 would be very low. Similarly, the O_2 flux through the solid oxide would be much smaller than observed.

We must then conclude that the mechanism based on expressions (1) and (2) are insufficient to describe the CO_2 and O_2 flux results. As formulated, the model assumes bulk diffusion by carbonate and oxygen ions through the molten salt and solid support, respectively, but does not account for specific microstructural details such as the length of the triple-phase-boundaries (TPB) where Equation (1) takes place. Moreover, assuming Equation (1) is the only mechanism taking place omits the possible contribution of other mechanisms involving reactions at the support-salt interfaces. One example is CO_2 transport mediated by pyrocarbonate $C_2O_5^{2-}$ ions [56], formed through the surface Reaction 4:

$$CO_{2(g)} + CO_3^{2-}{}_{(l)} \rightleftarrows C_2O_5^{2-}{}_{(l)}, \quad (4)$$

together with the interfacial Reaction 5:

$$C_2O_5^{2-}{}_{(l)} + O^{2-}{}_{(so)} \rightarrow 2CO_3^{2-}{}_{(l)}. \quad (5)$$

A combination of reactions (1), (4) and (5) might explain the permeation and, at the same time, account for the likely involvement of the solid oxide ionic conduction. Although at this stage this conclusion is not more than a hypothesis, it is supported by the distinctive characteristics of the MgSZ support used here: besides the reduced tortuosity factor arising from almost parallel pore alignment, the high pore density and their micrometric size provides a high specific length of TPB at the membrane surfaces and also a high volume-specific interfacial area between the support and the molten phase for reactions (1) and (5) to take place. More experiments are foreseen to validate this hypothesis. Varying the growth rate during the directional solidification, for instance, would allow control of the pore diameter (and accordingly the internal surface area and TPB length) while maintaining the total pore fraction.

The detection of O_2 permeation does not have a simple explanation.

O_2 permeation through the solid oxide in the form of O^{2-} ions requires the presence of electronic conductivity in either the oxide itself [5] or in the molten-carbonate phase [57]. Both possibilities do not seem likely, however; the electronic conductivity in MgSZ is expected to be negligible and, with regards to electronic conduction in the carbonate phase, this is still a proposition that has not been verified. The alternative is that oxygen permeates through the molten-carbonate phase in the form of CO_4^{2-} or CO_5^{2-}. This possibility has been proposed to explain the anomalously high O_2 flux in a metal-carbonate membrane [18] and is supported by DFT studies of different permeation mechanisms [21]. However, the proximity of the CO_2 to O_2 permeability ratio to 2:1 strongly points to both fluxes being related. The use of O_2 together with CO_2 in the feed gas for purely ionic conducting supports is uncommon but has been studied in membranes employing a mixed ionic-electronic conductor as the supporting matrix [5]. In Ref. [58], it was shown that CO_2 and O_2 permeation were interlinked so that in the absence of CO_2 there was no measurable O_2 permeation. In another work [59], using an SDC support and 15% CO_2, 10% O_2 in the feed gas, both CO_2 and O_2 gases were found at the permeate side and the CO_2 flux was enhanced as pO_2 was increased, but the authors attributed the occurrence of O_2 permeation to the mixed ionic-electronic conducting character of SDC. More experimental work is clearly needed to elucidate the complex permeation mechanisms taking place in this type of membrane.

7. Summary and conclusions

We have successfully produced a supported molten-salt membrane using a porous matrix, obtained by acid-etching a fibrilar MgSZ-MgO eutectic, as a ceramic support. The parent material was obtained by a laser-assisted directional solidification, demonstrating a new method for the preparation of laboratory-scale membranes with highly aligned pores which percolate between feed and permeate sides. This preparation method is applicable to a range of oxide materials, which will be useful for probing geometrical and mechanistic aspects of membrane permeation in the future. Here we have demonstrated that the supports confer a high permeability value of 1.41 x 10^{-10} mol $m^{-1}.s^{-1}.Pa^{-1}$ at 815 °C, which was attributed to the excellent pore and solid-oxide microstructural characteristics: good pore connectivity and alignment, high pore specific density and homogeneous micrometric pore size. These properties are specific to the directional-solidification preparation process and add to the properties common to supported molten-salt membranes, such as suitability for high-temperature operation and very high CO_2/N_2 selectivity. The good performance of the membrane reported here supports future efforts, both in experimentation and modelling, to understand the mechanisms involved in this type of membrane.

Author statement

Authors from Zaragoza conceived the work; all authors participated in experiment design, data collection and interpretation. All authors contributed to writing or performed a critical reading of the manuscript.

Declaration of competing interest

The authors declare that they have no known competing financial interests or personal relationships that could have appeared to influence the work reported in this paper.

Acknowledgments

The authors acknowledge the financial support from the Spanish Ministerio de Economía y Competitividad and Feder Funds under project MAT2016-77769R. L. Grima acknowledges financial support through grant BES-2017-079683 associated to the aforementioned project. The research leading to these results has received funding from the European Research Council under the European Union's Seventh Framework Programme (FP/2007-2013)/ERC Grant Agreement Number 320725 and from the Engineering & Physical Sciences Research Council (EPSRC) via grants EP/M01486X/1, EP/P007767/1 and EP/P009050/1. PRS acknowledges the Royal Academy of Engineering (CiET1718/59). PRS, DJLB, JJB and MDK acknowledge the support of The Faraday Institution (faraday.ac.uk; EP/ S003053/1). G. Mutch was supported by the Royal Academy of Engineering under the Research Fellowship Scheme and would like to thank the EPSRC for his Doctoral Prize Fellowship (EP/M50791X/1) and Newcastle University for a Newcastle University Academic Track (NUAcT) Fellowship. X-Ray CT acquisition and analysis was supported by UCL and EPSRC under EP/N032888/1. We thank the Servicio General de Apoyo a la Investigación-SAI (Universidad de Zaragoza) for technical support in X-ray diffraction and electron microscopy experiments, Rubén Gotor for technical assistance in sample preparation and R. Lahoz for laser-drilling the YSZ plate that serves as the membrane base. Data supporting this publication is available under a Creative Commons Attribution 4.0 International license, see DOI: 10.25405/data.ncl.1301924.

Appendix A. Supplementary data

Supplementary data to this article can be found online at https://doi.org/10.1016/j.memsci.2021.119057.

References

[1] H.B. Park, J. Kamcev, L.M. Robeson, M. Elimelech, B.D. Freeman, Maximizing the right stuff: the trade-off between membrane permeability and selectivity, Science 356 (2017) 1138–1148.
[2] G.A. Mutch, L. Qu, G. Triantafyllou, W. Xing, M.-L. Fontaine, I.S. Metcalfe, Supported molten-salt membranes for carbon dioxide permeation, J. Mater. Chem. A7 (2019) 12951–12973.
[3] P. Zhang, J. Tong, K. Huang, X. Zhu, W. Yang, The current status of high temperature electrochemistry-based CO_2 transport membranes and reactors for direct CO_2 capture and conversion, Prog. Energy Combust. Sci. 82 (2021) 100888.
[4] J.L. Wade, K.S. Lackner, A.C. West, Transport model for a high temperature, mixed conducting CO_2 separation membrane, Solid State Ionics 178 (2007) 1530–1540.
[5] Z. Rui, M. Anderson, Y.S. Lin, Y. Li, Modeling and analysis of carbon dioxide permeation through ceramic-carbonate dual-phase membranes, J. Membr. Sci. 345 (2009) 110–118.
[6] Y. Li, Z. Rui, C. Xia, M. Anderson, Y.S. Lin, Performance of ionic-conducting ceramic/carbonate composite material as solid oxide fuel cell electrolyte and CO_2 permeation membrane, Catal. Today 148 (2009) 303–309.
[7] M. Anderson, Y.S. Lin, Carbonate–ceramic dual-phase membrane for carbon dioxide separation, J. Membr. Sci. 357 (2010) 122–129.
[8] J.L. Wade, C. Lee, A.C. West, K.S. Lackner, Composite electrolyte membranes for high temperature CO_2 separation, J. Membr. Sci. 369 (2011) 20–29.
[9] J. Ortiz-Landeros, T. Norton, Y.S. Lin, Effects of support pore structure on carbon dioxide permeation of ceramic-carbonate dual-phase membranes, Chem. Eng. Sci. 104 (2013) 891–898.
[10] T.T. Norton, Y.S. Lin, Ceramic-carbonate dual-phase membrane with improved chemical stability for carbon dioxide separation at high temperature, Solid State Ionics 263 (2014) 172–179.
[11] X. Dong, J. Ortiz Landeros, Y.S. Lin, An asymmetric tubular ceramic-carbonate dual phase membrane for high temperature CO_2 separation, Chem. Commun. 49 (2013) 9654–9656.
[12] X. Dong, H.C. Wu, Y.S. Lin, CO_2 permeation through asymmetric thin tubular ceramic-carbonate dual-phase membranes, J. Membr. Sci. 564 (2018) 73–81.
[13] M. Zuo, S.J. Zhuang, X.Y. Tan, B. Meng, N.T. Yang, S.M. Liu, Ionic conducting ceramic-carbonate dual phase hollow fibre membranes for high temperature carbon dioxide separation, J. Membr. Sci. 458 (2014) 58–65.
[14] T. Chen, Z. Wang, J. Hu, M.H. Wai, S. Kawi, Y.S. Lin, High CO_2 permeability of ceramic-carbonate dual-phase hollow fiber membrane at medium-high temperature, J. Membr. Sci. 597 (2020) artn 117770.
[15] Y. Shilong, Y. Zhupeng, L. Chuanming, C. Xiaowei, Z. Yanwei, Theoretical description on the interface-enhanced conductivity of SDC/LiNa-carbonate composite electrolytes, Mater. Lett. 92 (2013) 78–81.
[16] L. Zhang, N. Xu, X. Li, S. Wang, K. Huang, W.H. Harris, W.K.S. Chiu, High CO_2 permeation flux enabled by highly interconnected three dimensional ionic channels in selective CO_2 separation membranes, Energy Environ. Sci. 5 (2012) 8310–8317.
[17] M. Kazakli, G.A. Mutch, G. Triantafyllou, A.G. Gil, T. Li, B. Wang, J.J. Bailey, D.J. L. Brett, P.R. Shearing, K. Li, I. Metcalfe, Controlling molten carbonate distribution in dual-phase molten salt-ceramic membranes to increase carbon dioxide permeation rates, J. Membr. Sci. 617 (2021) 118640.
[18] J. Fang, J. Tong, K. Huang, A superior mixed electron and carbonate-ion conducting metal-carbonate composite membrane for advanced flue-gas carbon capture, J. Membr. Sci. 505 (2016) 225–230.

[19] J. Fang, N. Xu, T. Yang, P. Zhang, J. Tong, K. Huang, CO_2 capture performance of silver-carbonate membrane with electrochemically dealloyed porous silver matrix, J. Membr. Sci. 523 (2017) 439–445.
[20] L. Zhang, Y. Gong, K.S. Brinkman, T. Wei, S. Wang, K. Huang, Flux of silver-carbonate membranes for post-combustion CO_2 capture: the effects of membrane thickness, gas concentration and time, J. Membr. Sci. 455 (2014) 162–167.
[21] L. Zhang, J. Tong, Y. Gong, M. Han, S. Wang, K. Huang, Fast electrochemical CO_2 transport through a dense metal-carbonate membrane: a new mechanistic insight, J. Membr. Sci. 468 (2014) 373–379.
[22] H. Huang, S. Cheng, J. Gao, C. Chen, J. Yi, Phase-inversion tape-casting preparation and significant performance enhancement of $Ce_{0.9}Gd_{0.1}O_{1.95}$–$La_{0.6}Sr_{0.4}Co_{0.2}Fe_{0.8}O_{3-\delta}$ dual-phase asymmetric membrane for oxygen separation, Mater. Lett. 137 (2014) 245–248.
[23] C. Gaudillere, J.M. Serra, Freeze-casting: fabrication of highly porous and hierarchical ceramic supports for energy applications, Bol. Soc. Esp. Ceram. Vidr. 55 (2016) 45–55.
[24] A.R. Studart, U.T. Gonzenbach, E.L. Tervoort, J. Gauckler, Processing routes to macroporous ceramics: a review, J. Am. Ceram. Soc. 89 (2006) 1771–1789.
[25] B.F.K. Kingsbury, K. Li, A morphological study of ceramic hollow fibre membranes, J. Membr. Sci. 328 (2009) 134–140.
[26] W.Y. Choi, H.E. Kim, Y.W. Moon, K.H. Shin, Y.H. Koh, Production of porous calcium phosphate ceramics with aligned pores using ceramic/camphene-based co-extrusion, Biomater. Res. 19 (2015) 16 (7 pages).
[27] L.A. McNeil, G.A. Mutch, F. Iacoviello, J.J. Bailey, G. Triantafyllou, D. Neagu, T. S. Miller, E.I. Papaioannou, W. Hu, D.J.L. Brett, P.R. Shearing, I.S. Metcalfe, Dendritic silver self-assembly in molten-carbonate membranes for efficient carbon dioxide capture, Energy Environ. Sci. 13 (2020) 1766–1775.
[28] P. Rudolph, T. Fukuda, Fiber crystal growth from the melt, Cryst. Res. Technol. 34 (1999) 3–40.
[29] J. Llorca, V.M. Orera, Directionally solidified eutectic ceramic oxides, Prog. Mater. Sci. 51 (2006) 711–809.
[30] Phase Equilibria Diagrams Online Database (NIST Standard Reference Database 31), The American Ceramic Society and the National Institute of Standards and Technology, 2020. Figure Number Zr-076-A.
[31] J. Echigoya, H. Suto, S. Hayashi, Growth morphology and orientation relationships in directionally solidified MgO-ZrO_2 eutectic, Trans. Jpn. Instit. Metals 26 (1985) 895–900.
[32] F.L. Kennard, R.C. Bradt, V.S. Stubican, Directional solidification of ZrO_2-MgO eutectic, J. Am. Ceram. Soc. 57 (1974) 428–431.
[33] G. Fiquet, P. Richet, G. Montagnac, High-temperature thermal expansion of lime, periclase, corundum and spinel, PhysChem. Min. 27 (1999) 103–111.
[34] Y. Shiratori, F. Tietz, H.P. Buchkremer, D. Stöver, YSZ–MgO composite electrolyte with adjusted thermal expansion coefficient to other SOFC components, Solid State Ionics 164 (2003) 27–33.
[35] V.M. Orera, R.I. Merino, J.A. Pardo, A. Larrea, J.I. Peña, C. González, P. Poza, J. Y. Pastor, J. Llorca, Microstructure and physical properties of some oxide eutectic composites processed by directional solidification, Acta Mater. 48 (2000) 4683–4689.
[36] D. Sola, P.B. Oliete, R.I. Merino, J.I. Peña, Directionally solidified Ni doped MgO-MgSZ eutectic composites for thermophotovoltaic devices, J. Eur. Ceram. Soc. 39 (2019) 1206–1213.
[37] S.P.S. Badwal, Zirconia-based solid electrolytes: microstructure, stability and ionic conductivity, Solid State Ionics 52 (1992) 23–32.
[38] R.I. Merino, V.M. Orera, J.I. Peña, G.F. de la Fuente, Conductivity anisotropy in directionally solidified $CaZrO_3$-CaSZ and MgO-MgSZ eutectics, Solid State Ionics 100 (1997) 313–318.
[39] J.J. Bailey, T.M.M. Heenan, D.P. Finegan, X. Lu, S.R. Daemi, F. Iacoviello, N. R. Backeberg, O.O. Taiwo, D.J.L. Brett, A. Atkinson, P.R. Shearing, Laser-preparation of geometrically optimised samples for X-ray nano-CT, J. Microscopy 267 (2017) 384–396.
[40] C. Sommer, C. Straehle, U. Köthe, F.A. Hamprecht, Ilastik: interactive learning and segmentation toolkit, in: IEEE International Symposium on Biomedical Imaging: from Nano to Macro, Chicago, IL, 2011, pp. 230–233, https://doi.org/10.1109/ISBI.2011.5872394.
[41] E. Barsoukov, J.R. Macdonald (Eds.), Impedance Spectroscopy: Theory, Experiments and Applications, Wiley-Interscience, Hoboken, 2005.
[42] S.G. Patrício, E.I. Papaioannou, B.M. Ray, I.S. Metcalfe, F.M.B. Marques, Composite CO_2 separation membranes: insights on kinetics and stability, J. Membr. Sci. 541 (2017) 253–261.
[43] K.A. Jackson, J.D. Hunt, Lamellar and rod eutectic growth, Trans. Metall. Soc. AIME 236 (1966) 1129–1142.
[44] T. Sato, T. Endo, M. Shimada, T. Mitsudome, N. Otabe, Hydrothermal corrosion of Mg-partially stabilized zirconia, J. Mat. Sci. 26 (1991) 1346–1350.
[45] M. Yashima, N. Ishizawa, N.M. Yoshimura, Application of an ion-packing model based on defect clusters to zirconia solid solutions: II, applicability of Vegard's law, J. Am. Ceram. Soc. 75 (1992) 1550–1557.
[46] H. Näfe, Conductivity of alkali carbonates, carbonate-based composite electrolytes and IT-SOFC, ECS J. Solid State Sci. Technol. 3 (2014) N7–N14.
[47] M.R. Cerón, L.S. Lai, S. Amiri, M. Monte, S. Katta, J.C. Kelly, M.A. Worsley, M. D. Merrill, S. Kim, P.G. Campbell, Surpassing the conventional limitations of CO_2 separation membranes with hydroxide/ceramic dual-phase membranes, J. Membr. Sci. 567 (2018) 191–198.
[48] B. Lu, Y.S. Lin, Synthesis and characterization of thin ceramic-carbonate dual-phase membranes for carbon dioxide separation, J. Membr. Sci. 444 (2013) 402–411.
[49] J. Echigoya, K. Sasai, H. Suto, Decomposition of cubic ZrO_2 in MgO-ZrO_2 eutectic, Trans. Jpn. Instit. Metals 27 (1986) 247–253.
[50] S.C. Farmer, L.H. Schoenlein, A.H. Heuer, Precipitation of $Mg_2Zr_5O_{12}$ in MgO-Partially-Stabilized ZrO_2, J. Am. Ceram. Soc. 66 (1983) c-, 107–c-109.
[51] N. Nakagawa, H. Ohtsubo, A. Mitani, K. Shimizu, Y. Waku, High temperature strength and thermal stability for melt growth composite, J. Eur. Ceram. Soc. 25 (2005) 1251–1257.
[52] J. Gurauskis, V. Lennikov, G.F. de la Fuente, R.I. Merino, Laser-assisted, crack-free surface melting of large eutectic ceramic bodies, J. Eur. Ceram. Soc. 31 (2011) 1251–1256.
[53] R. Campana, A. Larrea, J.I. Peña, V.M. Orera, J. Eur. Ceram. Soc. 29 (2009) 85–90.
[54] T. Wen, L. Xiaofei, K. Chukun, W. Weppner, Conductivity of MgO-doped ZrO_2, Solid State Ionics 18&19 (1986) 715–719.
[55] W. Deng, Y. Li, High-temperature electrical properties of polycrystalline MgO-doped ZrO_2, Mater. Res. Bull. 113 (2019) 182–189.
[56] L. Zhang, X. Huang, C. Qin, K. Brinkman, Y. Gong, S. Wang, K. Huang, First spectroscopic identification of pyrocarbonate for high CO_2 flux membranes containing highly interconnected three dimensional ionic channels, Phys. Chem. Chem. Phys. 15 (2013) 13147–13152.
[57] H. Näfe, Electrochemical CO_2 separation through an alkali-carbonate-based membrane, ECS J. Solid State Sci. Technol. 3 (2014) N23–N29.
[58] E.I. Papaioannou, H. Qi, I.S. Metcalfe, 'Uphill' permeation of carbon dioxide across a composite molten salt-ceramic membrane, J. Membr. Sci. 485 (2015) 87–93.
[59] J. Tong, L. Zhang, M. Han, K. Huang, Electrochemical separation of CO_2 from a simulated flue gas with high-temperature ceramic–carbonate membrane: new observations, J. Membr. Sci. 477 (2015) 1–6.

applied sciences

MDPI

Article

Generation of a Porous Scaffold with a Starting Composition in the $CaO–SiO_2–MgO–P_2O_5$ System in a Simulated Physiological Environment

Lorena Grima [1], María Díaz-Pérez [1], Javier Gil [1], Daniel Sola [2,3] and José Ignacio Peña [1,*]

[1] Instituto de Ciencia de Materiales de Aragón, Dpto. Ciencia y Tecnología de Materiales y Fluidos, Universidad de Zaragoza-CSIC, 50 018 Zaragoza, Spain; lgrima@unizar.es (L.G.); mariadiaz@unizar.es (M.D.-P.); jagilcor92@hotmail.com (J.G.)

[2] Laboratorio de Óptica, Centro de Investigación en Óptica y Nanofísica, Campus 7 Espinardo, Universidad de Murcia, 30 100 Murcia, Spain; daniel.sola@um.es

[3] Institut für Fertigungstechnik, Technische Universität Dresden, 01062 Dresden, Germany

* Correspondence: jipena@unizar.es

Received: 4 December 2019; Accepted: 27 December 2019; Published: 31 December 2019

Featured Application: Porous scaffolds for bone-tissue growth.

Abstract: Magnesium-based ceramics are involved in orthopedic applications such as bone scaffolds or implant coatings. They provide structural support to cells for bone ingrowth, but highly porous matrices cannot resist severe mechanical stress during implantation. In this study, the laser floating zone (LFZ) technique is used to prepare a dense crystalline material with composition in the $CaO–SiO_2–MgO–P_2O_5$ system. This material, under physiological conditions, is able to generate a porous scaffold controlled by the dissolution of the MgO phase, meeting the mechanical advantages of a dense material and the biological features of a porous scaffold. FESEM (Field emission scanning electron microscopy), XRD（X-ray Diffraction), EDS (Energy Dispersive X-rays spectroscopy), and ICP ((Inductively Coupled Plasma) analysis were carried out in order to characterize the samples before and after immersion in simulated body fluid (SBF).

Keywords: bioceramic scaffolds; bone regeneration; laser floating zone; magnesium oxide

1. Introduction

The increase in the age of the population carries greater incidence of musculoskeletal pathologies such as fractures, osteoporosis, and bone infection and tumors. The most commonly used therapies consist of the use of autografts, allografts, and xenografts, which present limitations such as the limited sources of bone, graft rejection problems, and the transmission of diseases. Implants and biomedical devices have been used to replace bones and joints, but these solutions are subject to many limitations such as fatigue, fractures, toxicity, and wear. In addition, the behavior of these implants and devices do not completely meet the requirements to which bone tissue is subjected [1–3].

In many situations, the success depends on the development of porous matrices (scaffolds) that provide the structural and mechanical support to cells for their attachment and proliferation. The material chosen as a matrix must meet be non-toxic, biocompatible, osteoproductive, osteconductive, and bioabsorbable and have sufficient mechanical properties to provide structural support during bone growth and remodeling [4–6].

Surface active silicate-based bioceramics are a subject of research on candidates for hard tissue regeneration because of their bioactivity. It is well known that wollastonite ($CaSiO_3$), larnite (Ca_2SiO_4), diopside ($CaMgSiO_6$), akermanite ($Ca_2MgSi_2O_7$), bredigite ($Ca_7MgSi_4O_{16}$), forsterite (Mg_2SiO_4), enstatite ($MgSiO_3$), and their combinations are suitable for tissue engineering that favors implant attachment to bone tissue, as they have the ability to generate a hidroxyapatite (HAp) layer in contact with simulated body fluid (SBF) and to stimulate the proliferation and adhesion of osteoblast cells. Among the multiphasic ceramics, $Ca_3(PO_4)_2$–$CaSiO_3$ [7–9], $Ca_3(PO_4)_2$–$CaMg(SiO_3)_2$ [10], $CaSiO_3$–$CaMg(SiO_3)_2$ [11], and $Ca_3(PO_4)_2$–$CaSiO_3$–$CaMg(SiO_3)_2$ [12] eutectics, also suitable for tissue engineering, have been widely studied for their bioactivity. The SBF solution mimics human blood plasma in terms of pH and ionic concentration. The choice of one or another ceramic material depends on the kinetics of HAp deposition, the degradation rate, or the enhanced mechanical behavior if load bearing properties are required. It is also well known that the presence of Ca, Mg, and Si ions can influence proliferation and osteogenesis-related gene expressions in the different stages of osteoblastic differentiation in a way that is favorable in the process of bone remodeling [13,14].

The main disadvantages of ceramics, glasses, bioglasses, and bioactive crystals are their fragility when they have a porous structure, and their surfaces' limited bioactivity when they are completely dense [15,16]. For this reason, some researchers have designed multiphasic ceramics with the ability of generating a porous structure by the dissolution of one of the phases in the presence of SBF. Moreover, an adequate selection of the phases enables one to adjust the mechanical properties, bioactivity, ion release, and resorption rate to the specific needs of the bone. However, the size of the porous structure formed is limited to the size of the resorbable phase, which is micrometric in the case of bioeutectics [8]. Nevertheless, surface microporosity might improve the bioactivity of the scaffolds, thereby enabling the adsorption of proteins and cells to a larger surface area.

Phase dissolution occurs via the breaking of bonds catalyzed by the absorption of protons or hydroxyl ions to such bonds. In the case of Wollastonite dissolution, the release of Ca^{2+} ions is accompanied by H^+ penetration deep into the structure, promoting silica tetrahedral condensation leading to the formation of a thin amorphous silica-rich layer at the surface. Such a layer slows down Wollastonite dissolution by decreasing the surface area exposed to the reactive fluid. This process influences the depth of the porous layer when a resorbable phase is present in a multiphasic bioceramic. Due to the consumption of protons (H^+), the pH increase and the newly formed negative silica layer attracts positive ions, and this gives rise to the re-adsorption of Ca, Mg, and other ions such as HPO_4^{2-} and OH^- from the media.

The role of Mg^{2+} ions in bone remodeling, skeletal development, human metabolism, and cellular processes such as bone cell adhesion and osteoblast proliferation is well established [17,18]. Oelkers et al. [19] reviewed the olivine dissolution rates in aqueous fluids and reported an initial non-stoichiometric release of Mg and SiO_2 due to the equilibration of the olivine (Forsterite) surface with the liquid, and this release was followed by an increase in Mg and SiO_2 concentrations in the liquid linearly with time. These ions are preferably released at low to neutral pH. The dissolution rates of the Forsterite, like other Mg-silicates, appear to decrease monotonically with increasing pH. In acidic conditions, the formation of a passivating amorphous SiO_2 layer is more active and is favored by the high solubility of Mg, which creates an increasing Si-rich surface.

The advantage of using MgO as a soluble phase is that the breaking of Mg–O bonds is the only step in the steady-state dissolution mechanism favoring the formation of interconnected porous pathways. This fact contrasts with multi-oxide silicates that need to break more than one distinct metal–oxygen bond in their structure to complete their dissolution, and this affects the porous formation rates. In these cases, the dissolution rate is established by the release of the less reactive metal since the rupture of the different oxygen metal bonds can occur at speeds that differ in orders of magnitude.

The purpose of our work was to develop a new material obtained from the melt with a composition that includes calcium and magnesium phosphate, silicate bioactive phases, and a primary phase of magnesium oxide that forms pores when dissolved in SBF, creating the mechanical

advantages of a dense material and the biological features of a porous scaffold. The microstructure upon different processing conditions and the bioactivity behavior through immersion in SBF were studied, and mechanical tests on the scaffolds were carried out.

2. Materials and Methods

2.1. Ceramic Preparation and Characterization

The following raw materials in the proportions, indicated in Table 1, were used: SiO_2 (purity: 99.8%, Alfa Aesar, Haverhill, Massachusetts, United States), calcium silicate (purity > 99%, Merck, Darmstaadt, Germany), MgO (purity > 99%, Merck, Darmstaadt, Germany), and $Ca_3(PO_4)_2$ (Carlo Erba, Barcelona, Spain).

Table 1. Composition (wt %) of the starting powder.

MgO	$CaSiO_3$	SiO_2	TCP
36.6	18.7	14.04	30.7

Starting from a powdered material, we generated ceramic rods via cold isostatic pressing. After that, we carried out a sintering process in a Hobersal oven at 1300 °C for 12 h to obtain compacted solids. The crystalline nature of the bioceramic was identified by X-ray diffraction (XRD) (model D-Max/2500, RIGAKU) working at 40 kV and 80 mA, using $K_{\alpha 1,2}$ radiation (1.5418 Å). The scanning was carried out between 5 and 80° (2 h) in 0.03° steps, counting for 1 s per step.

Microstructural characterization was performed in polished transverse and longitudinal cross sections of rods by means of back-scattered electron images obtained in a FE-SEM (Field Emission Scanning Electron Microscope model Carl Zeiss MERLIN, Jena, Germany). Quantitative analyses of Mg, P, Ca, Si, and O were conducted by means of the energy-dispersive X-ray spectroscopy (EDS) detector (INCA 350, Oxford Instruments, High Wycombe, UK) coupled with the FE-SEM. Specimens for this characterization were prepared using conventional metallographic procedures.

2.2. Laser Floating Zone Technique

Using the sintered rods as precursors, we grew crystalline bars by the laser floating zone (LFZ) technique using a CO_2 laser as a heating source (Blade 600, Electronic Engineering). This technique is based on focusing a laser beam on a precursor so that a small molten zone is established and moved along the sample to obtain a directionally solidified rod [20]. To eliminate the precursor porosity, a first densification step was applied at a pulling rate of 250 mm/h. The final directional solidification step was performed with the grown crystal traveling downwards to obtain bubble-free samples. Rods were grown at 50, 100, and 300 mm/h under a 50 rpm counter rotation of the solidified rod and the polycrystalline precursor. The solidified rods had a final diameter in the 2–2.5 mm range and a length of about 50 mm.

Phase formation and elemental composition of the phases at different pulling speeds were examined by FE-SEM.

2.3. Biodegradability Study

To study the biodegradability of the directionally solidified rods, they were cut into slices. After being washed in acetone, they were soaked in simulated body fluid (SBF), as proposed by Kokubo et al. [21,22], in polyethylene bottles kept at 37 °C under static conditions. The initial pH of the SBF was established between 7.2 and 7.4, in the range of normal pH of human plasma.

Disks were removed after 4 weeks and dried in air at room temperature. Sample surfaces and cross sections, before and after the exposure to the SBF, were examined by FE-SEM at 15 keV and EDS elemental microanalysis of calcium, magnesium, silicon, phosphorus, and oxygen were carried out.

The quantitative information of the ions released (Mg, Ca, P, and Si) into the SBF solution was determined by ICP using a Spectroblue TI FMT26 system.

2.4. Micro Hardness Test

Micro indentations were performed on polished surfaces of unsoaked samples using a diamond Vickers indenter, in the form of a pyramid, on a microhardness tester Matsuzawa, MXT 70. The procedure followed for the preparation of samples for the Vickers hardness measurements was the same as that followed for FE-SEM observation. The samples were tested applying a load of 200 gf for 15 s. At least 10 valid indentations were made for each sample, and the data are presented as mean values with standard deviations.

3. Results and Discussion

3.1. Ceramic Analysis

XRD and FE-SEM microstructural analysis of the ceramic precursors after sintering have been conducted, obtaining the results shown in Figures 1 and 2, respectively.

In Figure 1, there are peaks that correspond to periclase (MgO), forsterite (Mg_2SiO_4), and whitlockite ($Ca_{18}Mg_2H_2(PO_4)_{14}$). Because the powder holder is composed of SiO_2, peaks corresponding to this oxide were eliminated.

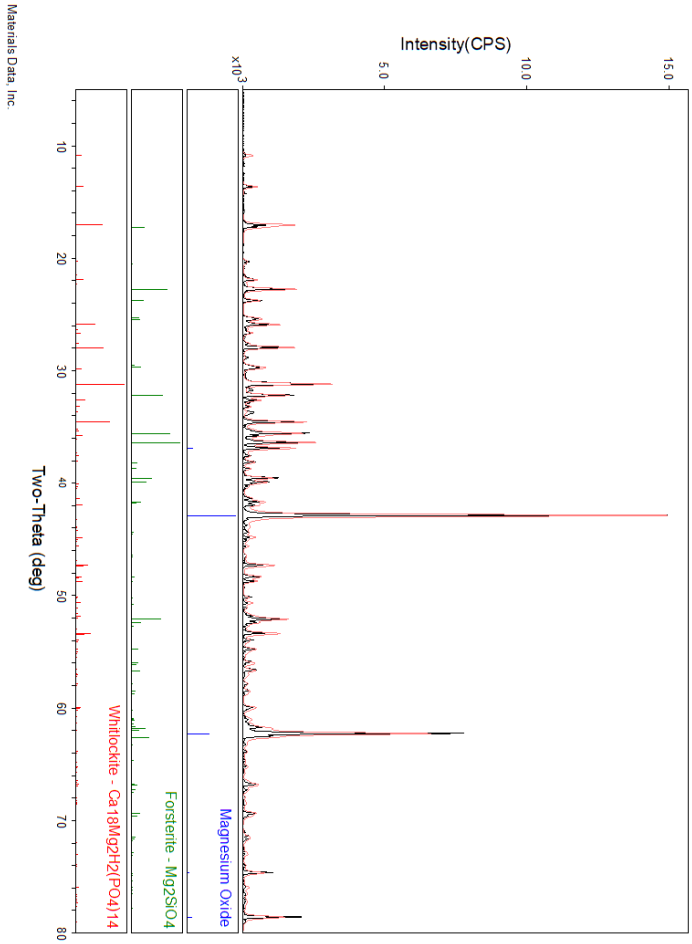

Figure 1. X-ray diffractogram of the ceramic material.

Figure 2 shows the microstructure of the sintered ceramic. It can be seen that, at this sintering temperature (1300 °C), reactions start to happen. For this reason, a light halo with a mixed oxide composition begins to form around SiO_2 grains (labeled as Phase 4, grey in the center of the picture). It is also possible to recognize the phases identified by XRD analysis: MgO (labeled as Phase 1, the darkest grey in the upper right corner of the picture), forsterite (labeled as Phase 3, dark grey), whitlockite (labeled as Phase 2, light grey), and tricalcium phosphate (TCP) (labeled as 5, the whitest phase). The composition of each phase is shown in Table 2. The chemical composition of a large region of the sample (General) corresponds in good approximation to the starting composition. In order to facilitate the identification of the different phases, the atomic percentages have been normalized to one of the ions.

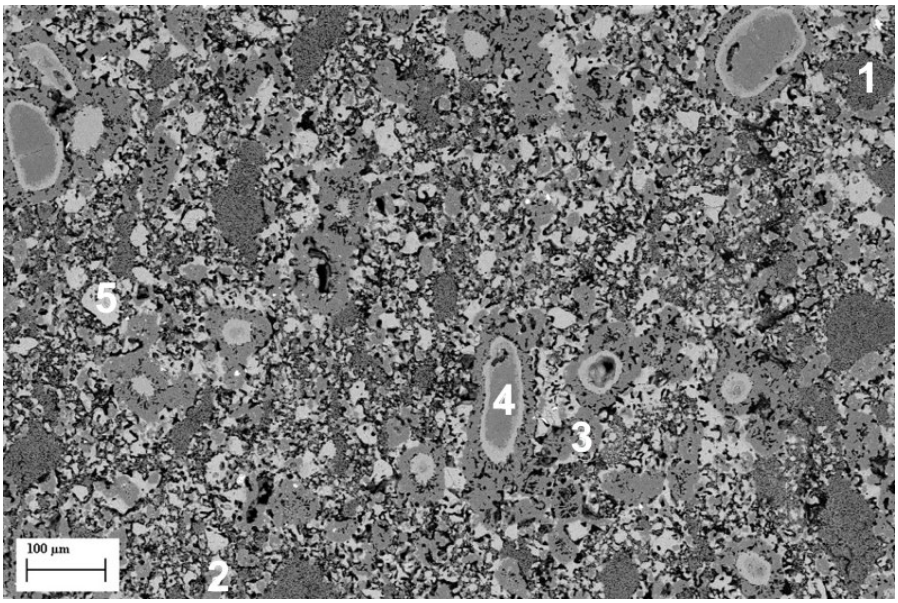

Figure 2. SEM (scanning electron microscope) image of the cross section of a sintered ceramic rod used as a precursor in the sample growth by the LFZ technique.

Table 2. Elemental composition (atom %) of the main present phases in the sintered ceramic rods.

	O	Mg	Si	P	Ca	Phase
General	59.17	21.63	7.02	5.21	6.27	-
1	1.0	1	-	-	-	MgO
2	62.9	2	-	16.9	20.3	Whitlockite ($Ca_{18}Mg_2H_2(PO_4)_{14}$)
3	3.8	1.8	1	-	-	Forsterite (Mg_2SiO_4)
4	2.0	-	1	-	-	SiO_2
5	3.74	-	-	1	1.17	Tricalcium Phosphate ($Ca_3(PO_4)_2$)

3.2. Microstructural Analysis of the Directionally Solidified Rods

Starting from the ceramic bars, directionally solidified rods by the laser floating zone technique were grown. In order to analyze the influence of the solidification rate in the microstructure of the samples, different growth speeds were used. The samples named M50, M100, and M300 correspond to rods grown at 50, 100, and 300 mm/h, respectively. As the axial temperature gradient (G) at the solid–liquid interface were of the order of 5×10^5 K/m in the solid, the cooling rates (CR) were 7, 14, and 41.5 K/s for pulling rates (R) of 50, 100, and 300 mm/h, respectively ($CR = G \times R$).

Figure 3 corresponds to a SEM picture of a transversal cross section of a sample grown at 50 mm/h. Three different phases can be observed: the black one corresponds to magnesium oxide (MgO) (1), the dark gray corresponds to monticellite ($CaMgSiO_4$) (2), and the lighter gray is compatible with a solid solution of dicalcium magnesium silicate ($Ca_{2-x}Mg_xSiO_4$) (3) with phosphorus.

The identification of the phases and atomic percentages are shown in Table 3. In Phase 3, the Mg ion replaced the position of the Ca ion, and this formed a solid solution. As more than 15% of Ca was substituted by Mg, it is expected that the crystallinity of this phase cannot be retained, which forms a vitreous network where phosphorus can be incorporated.

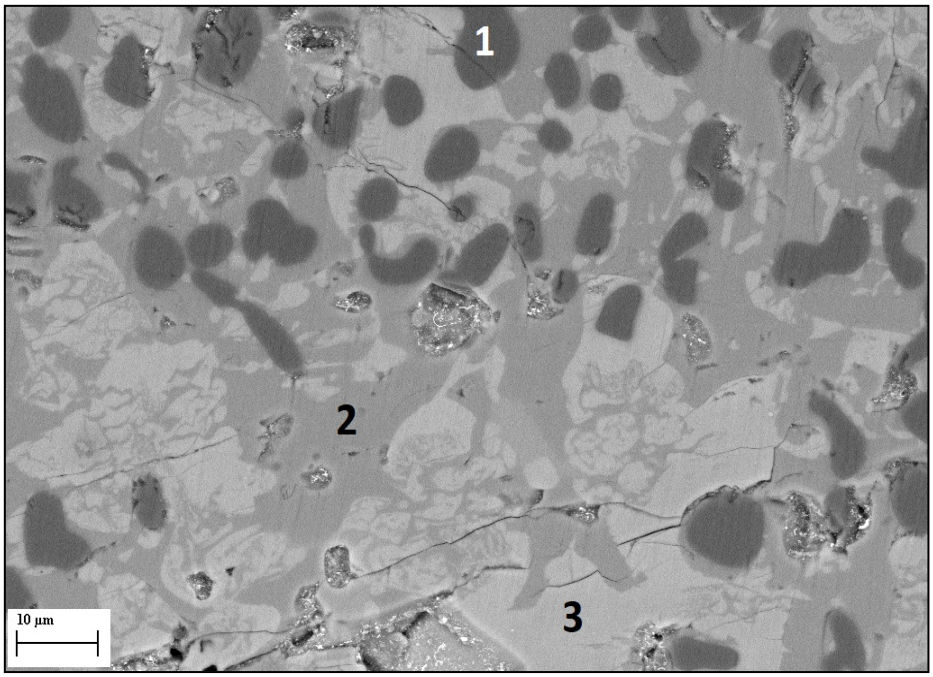

Figure 3. SEM image of a directionally solidified rod grown at 50 mm/h.

Table 3. EDS analysis (atom %) for directionally solidified rods at 50 mm/h.

Spectrum	O	Mg	Si	P	Ca	Phase
General	57.89	16.29	10.52	1.95	13.35	
1	50.67	49.33	-	-	-	MgO
2	57.71	13.96	14.84	0.52	12.98	Monticellite ($CaMgSiO_4$)
3	59.04	3.98	12.28	3.12	21.57	$Ca_{2-x}Mg_xSiO_4$ + P

Figure 4 shows a SEM cross-section view of the sample grown at 100 mm/h. In this micrograph, four phases can be observed: the dark one corresponds to magnesium oxide (MgO) primary phase (1), and the others correspond to monticellite ($CaMgSiO_4$), akermanite (3) ($Ca_2MgSi_2O_7$), and TCP (4). Part of the TCP formed a eutectic constituent with monticellite (2), and the akermanite phase contained phosphorus that was dissolved in its structure. The atomic percentages of the phases are shown in Table 4.

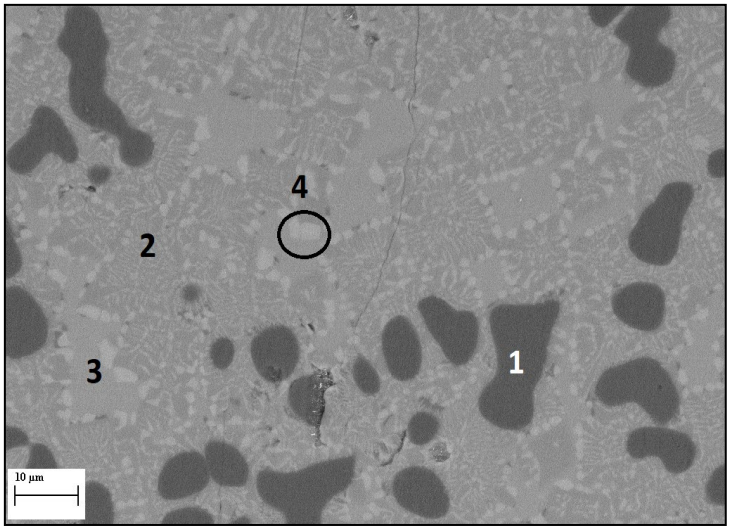

Figure 4. SEM image of a directionally solidified rod grown at 100 mm/h.

Table 4. EDS analysis (atom %) for directionally solidified rods at 100 mm/h.

	O	Mg	Si	P	Ca	Phase
General	58.20	17.54	9.97	9.97	11.30	
1	50.94	48.89	-	-	-	MgO
2	57.93	13.64	11.4	3.32	13.71	Monticellite + TCP (eutectic constituent)
3	60.78	6.54	15.35	3.47	13.86	Akermanite + P (solid solution)
4	60.16	-	-	10.15	19.13	TCP

Monticellite has been considered a candidate for bone replacement [23,24] because of its good cytocompatibility, osteogenic activity, and antibacterial and anti-biofilm properties. Akermanite has shown bioactive properties in both in vivo and in vitro conditions [25,26].

Figure 5 shows a SEM cross-section view of the sample grown at 300 mm/h. Three main phases, whose compositions are indicated in Table 5, can be identified.

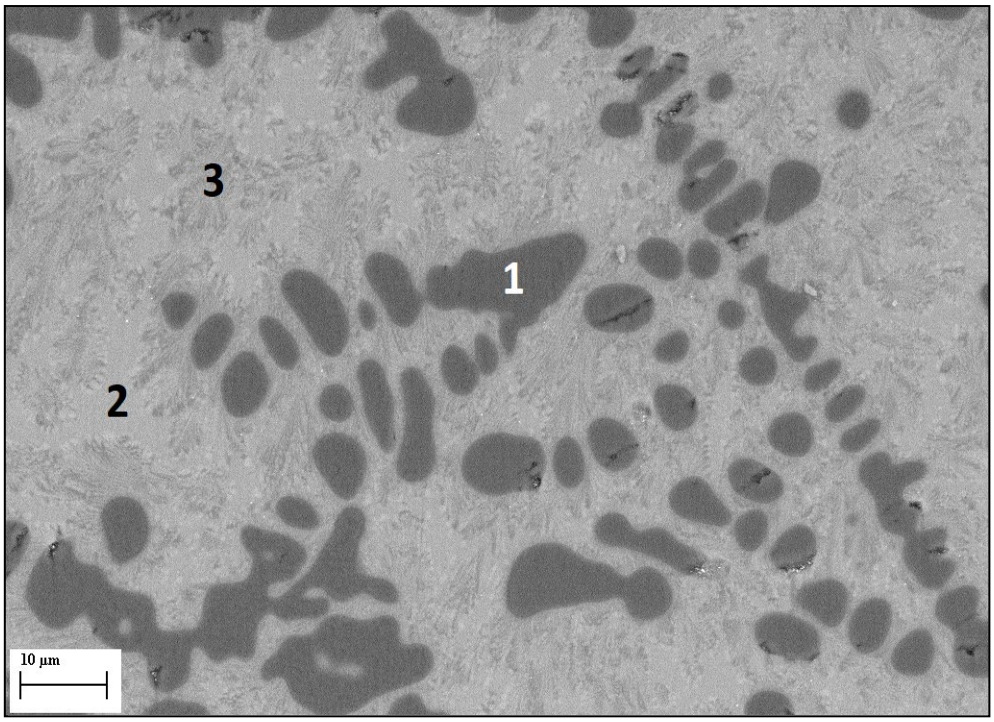

Figure 5. SEM micrograph of a directionally solidified rod grown at 300 mm/h.

It is possible to detect small phases surrounding the akermanite, and these phases can be assigned to TCP based on a comparison with the sample grown at 100 mm/h. In fact, both microstructures are similar except for the smaller size of the phases in the case of the sample grown at a faster rate, as expected.

Table 5. EDS analysis (atom %) for directionally solidified rods at 300 mm/h.

	O	Mg	Si	P	Ca	Phase
General	57.66	21.81	8.27	3.22	9.05	
1	50.52	49.33	-	-	-	MgO
2	60.78	6.31	15.61	3.18	14.36	Akermanite + P (solid solution)
3	59.47	13.06	10.75	4.79	11.93	Monticellite + TCP (eutectic constituent)

At a faster growing rate (300 mm/h), the general composition is more similar to the starting one than that of samples grown at slower rates (100 and 50 mm/h). This fact might be due to the loss by evaporation of the most volatile elements, mainly P, and this loss is higher at lower growth speeds. The loss of phosphorus by evaporation could explain the impossibility of TCP formation in samples grown at lower speeds.

3.3. Micro Hardness Analysis

Hardness values were obtained from Vickers micro hardness tests on polished cross sections of the unsoaked samples. These values are depicted in Table 6 and compared with the hardness of different bioceramics and bone tissues.

Table 6. Vickers hardness comparison of different materials used as bone substitutes. M50, M100, and M300 correspond to samples grown at 50, 100, and 300 mm/h.

Sample	Growing Speed (mm/h)	Vickers Hardness (GPa)
Bone [2]	-	0.42
Enamel [27]	-	3.3–3.6
TCP-5wt % MgO composites [28]	-	4.5
$CaMg(SiO_3)_2$–$Ca_3(PO_4)_2$ [3]	-	4.1 ± 0.4
$CaSiO_3$–$Ca_3(PO_4)_2$ [3]	-	5.1 ± 0.4
$CaSiO_3$–$CaMg(SiO_3)_2$–$Ca_3(PO_4)_2$ (eutectic glass) *	-	4.13 ± 0.35
M50	50	4.63 ± 0.36
M100	100	5.30 ± 0.43
M300	300	5.02 ± 0.33

* Grown by the LFZ technique for this work.

Poor mechanical properties limit the applications of ceramics with good bioactivity. In this sense, the development of Mg–Ca-based ceramics with increasing Mg content (8.3% for akermanite and 14.3 for monticellite) has led to the improvement of the mechanical properties of materials for bone defect repair. As the bond energy of the Mg–O is higher than that of the Ca-O due to their differences in ion radius, the presence of magnesium silicates may be beneficial for the mechanical strength of the scaffolds. In the table, we can observe that the hardness obtained for the present samples are close to the values of other materials used for the same purpose. For this reason, we can conclude that the hardness of this new material is in the required range of a bone substitute.

3.4. Biodegradable Study of the Solidified Rods

To study the bioactive behavior of the directionally solidified rods, we placed some discs of different samples in SBF. After being soaked for 4 weeks, we analyzed them via SEM. Figure 6a

shows the effect of SBF in a directionally solidified rod grown at 50 mm/h (M50). An extended area of the surface in contact with the fluid is presented in Figure 6b. In those images, we can observe the dissolution of one of the phases, which corresponds to the MgO phase.

As adjacent MgO phases dissolve, an open porosity forms, and this provides transport channels for the migration of protons and Mg^{2+} ions. In this case, the contiguity and volume fraction of the MgO phases are important determining factors in the penetration depth of the dissolution reaction.

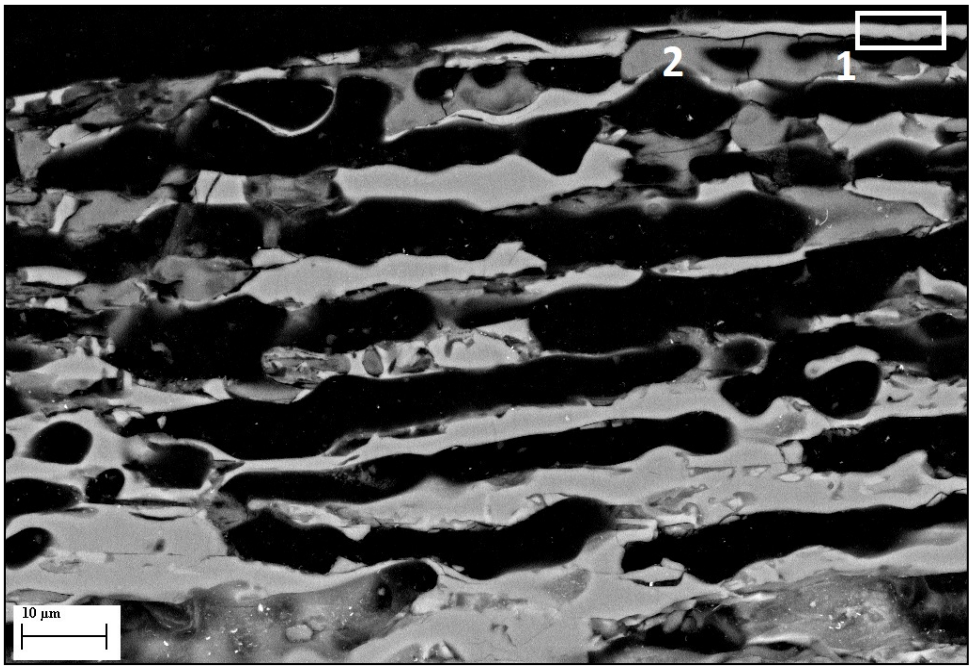

(**a**)

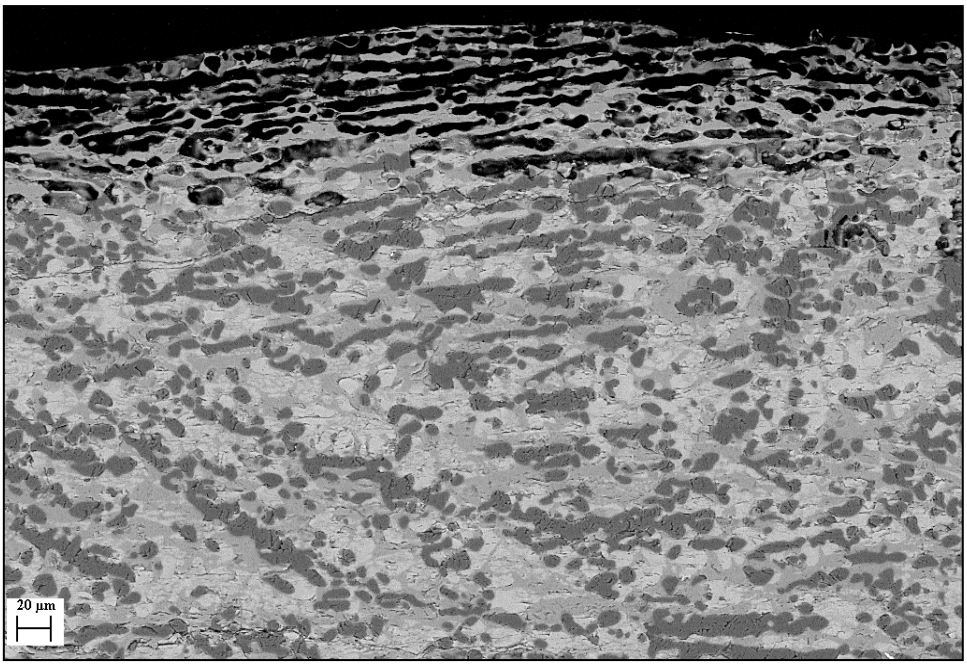

(**b**)

Figure 6. SEM micrographs of a directionally solidified rod grown at 50 mm/h after soaking in the simulated body fluid (SBF) solution for 28 days: longitudinal cross section (**a**) and an extended area of the sample surface in contact with the fluid (**b**).

No external HA layer that would block the dissolution of the MgO was formed. For this reason, the dissolution of the MgO phase could continue, which gave rise to a porous scaffold with channels between 5 and 10 μm in thickness. MgO dissolution is controlled by chemical reactions (Equations (1)–(3)) that involve the dissolution of MgO in a liquid medium to produce Mg^{2+} and OH^-. As a consequence of water molecules, an intermediate brucite product was generated and subsequently dissociated into Mg^{2+} and hydroxyl ions that form water by protonation.

$$MgO\ (s) + H_2O\ (l) \rightarrow MgOH^+\ (aq) + OH^-\ (aq) \quad (1)$$

$$MgOH^+\ (aq) + 2H_2O\ (l) \rightarrow Mg(OH)_2\ (l) + H_3O^+\ (aq) \quad (2)$$

$$Mg(OH)_2\ (l) \rightarrow Mg(aq)^{2+} + 2OH^-\ (aq) \quad (3)$$

In the zone where MgO dissolution occurred, the monticellite phase (1) remained unchanged, while the composition of the other phase (2) changed, losing silicon and incorporating phosphorus to a composition similar to that of the monetite ($CaHPO_4$), as indicated in Table 7.

Table 7. EDS analysis (atom %) for directionally solidified rods grown at 50 mm/h after soaking in the SBF solution for 28 days.

	O	Mg	Si	P	Ca	Phase
1	61.51	13.20	13.22	0.99	11.08	Monticellite
2	70.01	3.09	0.30	14.05	12.56	Monetite

These compositional changes of the phases occurred by interaction of the sample surface with the liquid medium and have an influence on the final composition of the fluid. In Table 8, we present the ICP results of the SBF analysis after being in contact with a directionally solidified rod compared with the concentration values in the SBF before the bioactivity test.

Table 8. Ion concentration of SBF (simulated body fluid) before and after 28 days of sample inmersion. Results in mM.

	Ca	Mg	P	Si
Before Bioactivity	2.5	1.5	1	-
After Bioactivity	2.2	3.5	0.91	0.22

As can be seen in Table 8, during the reaction of the ceramic composite in SBF, the calcium and phosphorus ion concentrations did not increase during exposure, although an increase in the magnesium and silicon ion concentrations can be observed. This fact indicates the surface dissolution of the MgO primary phase and release to the fluid of Si^{4+} from the soluble amorphous silicate phase (Table 3, Phase 3).

Both the increase in the concentration of Mg ion in SBF after the bioactivity test and the porous structure formation evidence the dissolution of the MgO primary phase. This mechanism led to the "in situ" formation of a porous structure that could reproduce the bone structure and its mechanical properties.

The increase in Mg and Si ion concentration is attributed to the exchange of Mg and Si ions from the sample with H^+ ions from the fluid. The MgO dissolution could proceed by the breaking of the relatively weak ionic divalent metal–oxygen bonds, which liberated the Mg ions directly into solution. This fast dissolution of magnesia contrasts to the behavior of other multi-oxide phases that require the breaking of more than one type of metal–oxygen bond. In these cases, the dissolution mechanism involves the sequential breaking of the bonds, which follows an order according to their reactivity. Some studies of the forsterite-rich olivine dissolution mechanisms have been reported by Oelkers et al. [19]. They concluded that olivine dissolution rates are strongly influenced by pH, water activity, and mineral–fluid interfacial surface area.

There is no evidence that a silica-rich layer was formed. When this layer, due to the reaction of Si with OH^-, was formed on the sample, the surface acted as a nucleation agent for HAp formation. In this case, the increase in Mg in the fluid medium can reduce the rate of a stable apatite phase formation, as reported by Vallet-Regi [29]. Moreover, the decrease in P ion concentration in the fluid was consistent with the transformation of the $Ca_{2-x}Mg_xSiO_4{}^+P$ phase to a P-rich and Si-depleted phase, while the monticellite phase remained unaltered.

The longitudinal cross section and surface morphology of the sample grown at 100 mm/h after soaking in SBF for 28 days are shown in Figure 7a. The presence of a large number of pores at different sizes significantly increased the surface roughness and total porosity, as shown in Figure 7b. This morphology contributed beneficially to the process of scaffold integration and influenced the bone healing rate. The composition of the phases in the interaction zone with SBF is given in Table 9. In the active region pores, monticellite and a new phase with a composition compatible with monetite can be identified.

Table 9. EDS analysis (atom %) for directionally solidified rods grown at 100 mm/h after soaking in the SBF solution for 28 days.

	O	Mg	Si	P	Ca	Phase
1	70.2	4.14	0.35	13.45	11.94	Monetite
2	58.10	14.10	14.38	0.81	12.61	Monticellite

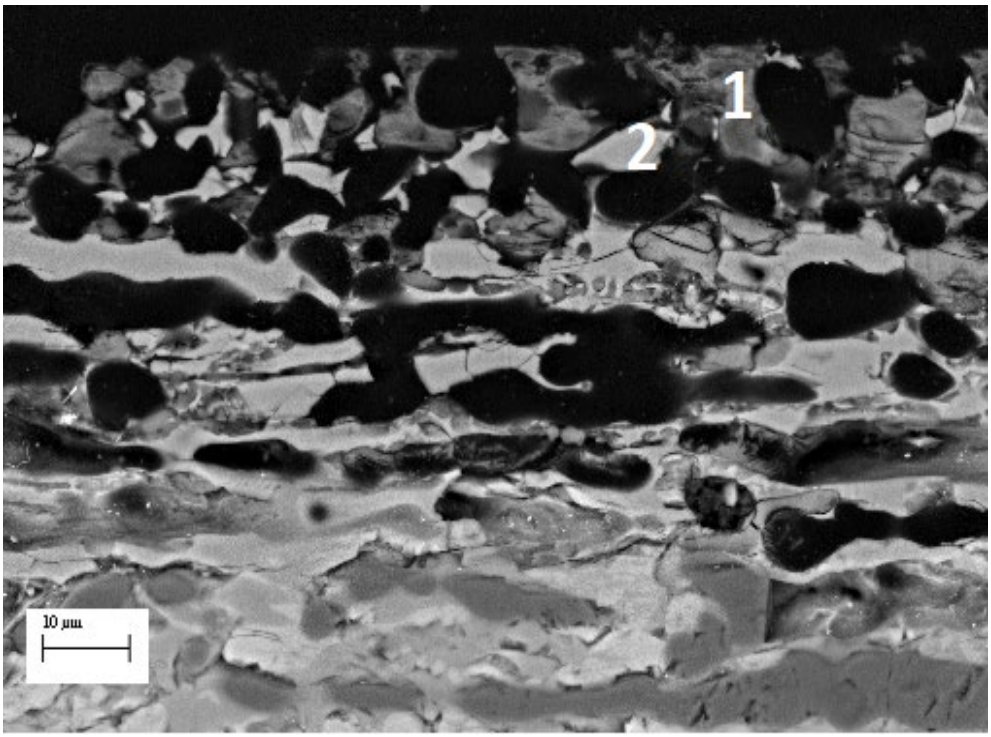

(**a**)

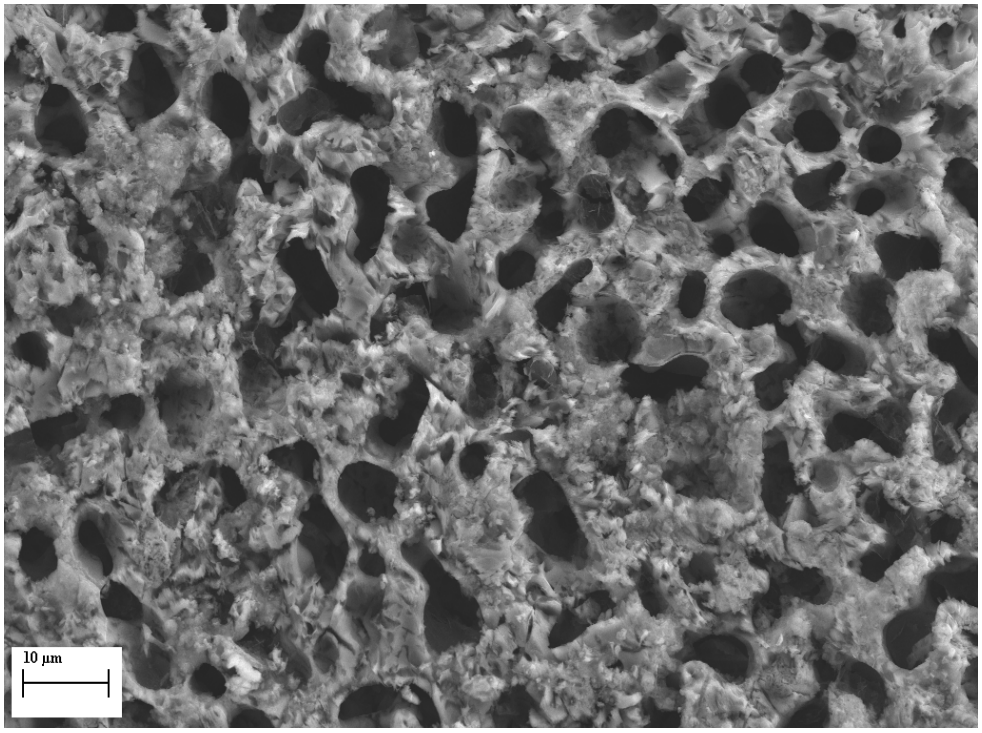

(**b**)

Figure 7. SEM image of a sample grown at 100 mm/h after soaking in the SBF solution for 28 days: longitudinal cross section (**a**) and disc surface (**b**).

A similar behavior was observed in samples grown at 300 mm/h. The FE-SEM micrograph of the polished longitudinal cross section of the sample after soaking in SBF for 28 days is shown in Figure 8a. The surface of the sample was eroded by the dissolution of the MgO phases in the SBF during the period of immersion forming a porous structure layer. The depth of the porous layer at this time was about 20–30 μm.

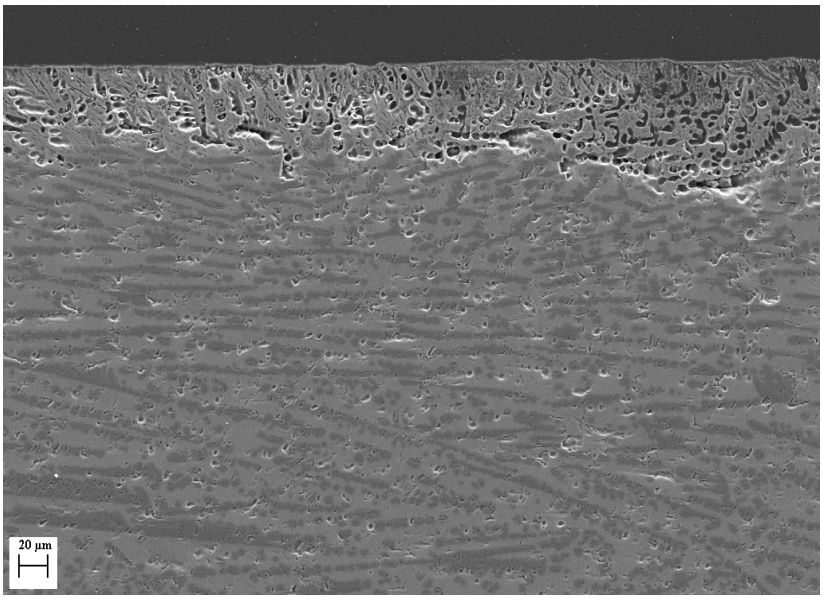

(**a**)

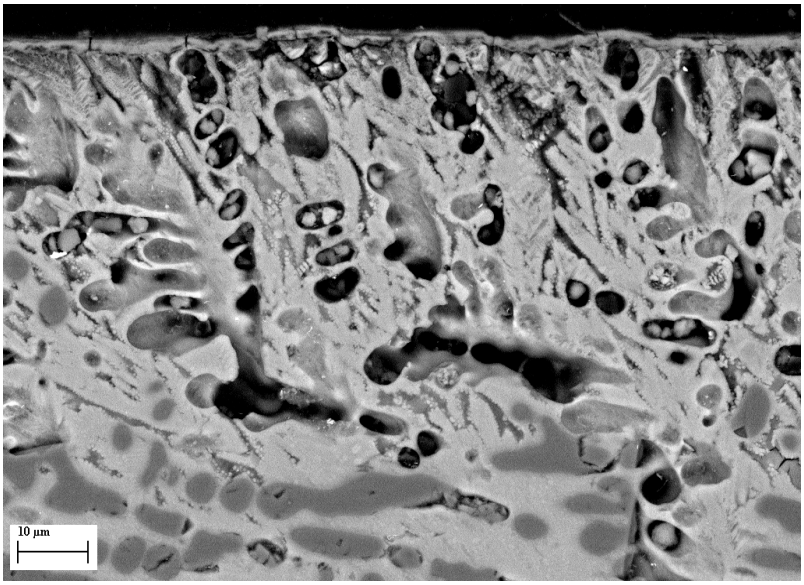

(**b**)

Figure 8. SEM image of a sample grown at 300 mm/h after soaking in the SBF solution for 28 days: longitudinal cross section (**a**) and a detailed zone of the sample surface in contact with the fluid (**b**).

The formation of a thin submicrometric layer was observed on the surface of the sample as shown in Figure 8b. This layer was determined to be bone-like apatite, although from EDS microanalysis the Ca/P ratio was 1.26, lower than that of the hydroxyapatite.

4. Conclusions

At the end of this work, we could establish the following conclusions:

- Crystalline rods with compositions in the $CaO–SiO_2–MgO–P_2O_5$ system were grown via the LFZ technique at speeds of 50, 100, and 300 mm/h, and an MgO primary phase was obtained with other bioactive phases at all speed conditions.
- The surface of the crystalline rods (M50, M100, and M300) presented a response in contact with the SBF, and this response consisted of the dissolution of magnesium oxide phases and the transformation of some of the other phases. The dissolution of MgO phases generated a porous layer with interconnected pores that acted as transport channels for the liquid medium to continue MgO leaching inside the matrix.
- Samples grown at 50 and 100 mm/h after soaking in SBF for four weeks did not form HAp layer, and this favored the dissolution of the MgO phases. The release of biocompatible Mg^{2+} ions acted as an inhibitor of hydroxyapatite crystal growth suppressing unwanted crystallization in vivo.
- The micro hardness of the unsoaked samples lies between 4.63 and 5.30 GPa, which is comparable to other bioceramics used in bone repair. Porosity formation by the leaching of magnesium oxide in SBF can reduce the hardness, bringing it closer to that of natural bone.
- As the material is able to generate a porous scaffold, in order to conclude if this new Mg-based formulation can be used as a bone replacement, cell tests and in vivo experiments are needed.

Author Contributions: J.I.P. and L.G. conceived and planned the experiments. J.G., L.G., M.D.-P and D.S. carried out the experiments. J.I.P. contributed to sample preparation and characterization. All authors contributed to the interpretation of the results and provided critical feedback. J.I.P. wrote the paper with input from all authors. All authors have read and agreed to the published version of the manuscript.

Funding: This project has been partially funded by the PIT2 program of the University of Murcia's own research plan. Fundación Séneca grants No 20647/JLI/18 and the European Union's Horizon 2020 research and innovation program under the Marie Skłodowska-Curie IF No 795630 are also acknowledged.

Acknowledgments: The authors would like to acknowledge the use of Servicio General de Apoyo a la Investigación-SAI, Universidad de Zaragoza.

Conflicts of Interest: The authors declare no conflict of interest.

References

1. Agarwal, R.; García, A.J. Biomaterial strategies for engineering implants for enhanced osseointegration and bone repair. *Adv. Drug Deliv. Rev.* **2015**, *94*, 53–62.
2. Kim, H.W.; Kim, H.E.; Salih, V. Stimulation of osteoblast responses to biomimetic nanocomposites of gelatin-hydroxyapatite for tissue engineering scaffolds. *Biomaterials* **2005**, *26*, 5221–5230.
3. Wei, G.; Ma, P.X. Structure and properties of nano-hydroxyapatite/polymer composite scaffolds for bone tissue engineering. *Biomaterials* **2003**, *25*, 4749–4757.
4. Ma, P.; Wei, G. Nanoestructured scaffolds for tissue engineering and regeneration. *Handb. Nanostructured Biomater. Appl. Nanobiotechnol.* **2005**, *1*, 1–21.
5. Rezwan, K.; Chen, Q.Z.; Blaker, J.J.; Boccaccini, R. Biodegradable and bioactive porous polymer/inorganic composite scaffolds for bone tissue engineering. *Biomaterials* **2006**, *27*, 3413–3431.
6. Salgado, A.J.; Coutinho, O.P.; Reis, R.L. Bone tissue engineering: State of the art and future trends. *Macromol. Biosci.* **2004**, *4*, 743–765.
7. Roseti, L.; Parisi, V.; Petretta, M.; Cavallo, C.; Desando, G.; Bartolotti, I.; Grigolo, B. Scaffolds for Bone Tissue Engineering: State of the art and new perspectives. *Mater. Sci. Eng.* **2017**, *78*, 1246–1262.
8. De Aza, P.N.; Peña, J.I.; Luklinska, Z.B.; Meseguer-Olmo, L. Bioeutectic® Ceramics for Biomedical Application Obtained by Laser Floating Zone Method. In vivo Evaluation. *Materials* **2014**, *7*, 2395–2410.
9. Sola, D.; Paulés, D.; Grima, L.; Anzano, J. Laser-Induced Breakdown Spectroscopy (LIBS) for Monitoring the Formation of Hydroxyapatite Porous Layers. *Materials* **2017**, *10*, 1395–1401.
10. García-Páez, I.H.; Pena, P.; Baudín, C.; Rodríguez, M.A.; Cordoba, E.; De Aza, A.H. Processing and in vitro bioactivity of a β-$Ca_3(PO_4)_2$–$CaMg(SiO_3)_2$ ceramic with the eutectic composition. *Bol. Soc. Esp. Ceram. Vidr.* **2016**, *55*, 1–12.
11. Sainz, M.A.; Pena, P.; Serena, A.; Caballero, A. Influence of design on bioactivity of novel $CaSiO_3$–$CaMg(SiO_3)_2$ bioceramics: In vitro simulated body fluid test and thermodynamic simulation. *Acta Biomater.* **2010**, *6*, 2797–2807.
12. Magallanes-Perdomo, M.; De Aza, A.H., Sobrados, I.; Sanz, J.; Pena, P. Structure and properties of bioactive eutectic glasses based on the $Ca_3(PO_4)_2$–$CaSiO_3$–$CaMg(SiO_3)_2$ system. *Acta Biomater.* **2012**, *8*, 820–829.
13. Sola, D.; Balda, R.; Al-Saleh, M.; Peña, J.I.; Fernández, J. Time-resolved fluorescence line-narrowing of Eu^{3+} in biocompatible eutectic glass-ceramics. *Opt. Express* **2013**, *21*, 6561–6571.
14. Sola, D.; Grima, L. Laser machining and in vitro assessment of wollastonite-tricalcium phosphate eutectic glasses and glass-ceramics. *Materials* **2018**, *11*, 125–126.
15. Qizhi, Z.; Chen, I.D.; Thompson, A.R. 45S5 Bioglasss-derived glass–ceramic scaffolds for bone tissue engineering. *Biomaterials* **2006**, *27*, 2414–2425.
16. Sabree, I.; Gough, J.E.; Derby, B. Mechanical properties of porous ceramic scaffolds: Influence of internal dimensions. *Ceram. Int.* **2015**, *41*, 8425–8432.
17. Diba, M.; Goudouri, O.M.; Tapia, F.; Boccaccini, A.R. Magnesium-containing bioactive polycrystalline silicate-based ceramics and glass-ceramics for biomedical applications. *Curr. Opin. Solid State Mater. Sci.* **2014**, *18*, 147–167.

18. Wu, C.; Chang, J.; Wang, J.; Ni, S.; Zhai, W. Preparation and characteristics of a calcium magnesium silicate (bredigite) bioactive ceramic. *Biomaterials* **2005**, *26*, 2925–2931.
19. Oelkers, E.H.; Declercq, J.; Saldi, G.D.; Gislason, S.R.; Schott, J. Olivine dissolution rates: A critical review. *Chem. Geol.* **2018**, *500*, 1–19.
20. Sola, D.; Ester, F.J.; Oliete, P.B.; Peña, J.I. A Study of the stability of the molten zone and the stresses induced during the growth of Al2O3-Y3Al5O12 eutectic composite by the laser floating zone technique. *J. Eur. Ceram. Soc.* **2011**, *31*, 1211-1218.
21. Kokubo, T.; Kushitani, H.; Sakka, S.; Kitsugi, T.; Yamamuro, T. Solutions able to reproduce in vivo surface-structure changes in bioactive glass-ceramics A-W. *J. Biomed. Mater. Res.* **1990**, *24*, 721–734.
22. Oyanete, A.; Kim, H.; Furuya, T.; Kokubo, T.; Miyazaki, T.; Nakamura, T. Preparation and assessment of revised simulated body fluid. *J. Biomed. Mater. Res. A* **2003**, *65*, 188–195.
23. Chen, X.; Ou, J.; Kang, Y.; Huang, Z.; Zhu, H.; Yin, G.; Wen, H. Synthesis and characteristics of Monticellite bioactive ceramic. *J. Mater. Sci. Mater. Med.* **2008**, *19*, 1257–1263.
24. Kalantari, E.; Naghib, S.M.; Naimi-Jamal, M.R.; Esmaeili, R.; Majidzadeh-A., K.; Mozafari, M. Nanostructured Monticellite: An emerging player in tissue engineering. *Mater. Today Proc.* **2018**, *5*, 15744–15753.
25. Huang, Y.; Jin, X.; Sun, H.; Tu, J.; Tang, T.; Chang, J.; Dai, K. In vitro and in vivo evaluation of Akermanite bioceramics for bone regeneration. *Biomaterials* **2009**, *33*, 5041–5048.
26. Sun, H.; Wu, C.; Dai, K.; Chang, J.; Tang, T. Proliferation and osteoblastic differentiation of human bone marrow-derived stromal cells on Akermanite-bioactive ceramics. *Biomaterials* **2006**, *27*, 5651–5657.
27. Hench, L.L. Bioceramics. *J. Mater. Ceram. Soc.* **1998**, *7*, 1705–1728.
28. Trabelsi, M.; AlShahrani, I.; Algarni, H.; Ayed, F.B.; Yousef, E.S. Mechanical and tribological properties of the tricalcium phosphate-magnesium oxide composites. *Mater. Sci. Eng. C* **2019**, *96*, 716–729.
29. Vallet-Regi, M.; Salinas, A.; Roman, J.; Gil, M. Effect of magnesium content on the in vitro bioactivity of CaO-MgO-SiO_2-P_2O_5 sol-gel glasses. *J. Mater. Chem.* **1999**, *9*, 515–518.

5. Descripción de los artículos publicados.

Atendiendo a este primer objetivo de la tesis se han publicado tres artículos:

1. El propósito fundamental del primero de ellos, "L. Grima, J.I. Peña, M.L. Sanjuán, Pyrochlore-like ZrO_2-PrO_x compounds: The role of the processing atmosphere in the stoichiometry, microstructure and oxidation state, Journal of Alloys and Compounds **923**, 166449 (2022)" reside en examinar la relación entre la composición, la microestructura y el estado de oxidación de los materiales con composición $Pr_{2\pm x}Zr_{2\mp x}O_{7\pm y}$ y estructura de tipo pirocloro. Para ello se plantea la fabricación de materiales del sistema ZrO_2–PrO_x mediante fusión zonal láser (LFZ) bajo diferentes condiciones ambientales desde entornos reductores hasta oxidantes, ya que se consideran materiales interesantes para diseñar catalizadores basados en elementos de valencia mixta.

   Se analizaron los resultados obtenidos de tres composiciones diferentes, P1.7ZO, PZO y P2.24ZO. De este modo pretendemos profundizar en la comprensión de la relación entre las condiciones de procesado, la estequiometría de las muestras y las diferencias estructurales y microestructurales de las mismas.

   Los resultados obtenidos sugieren una influencia significativa de la composición y el tratamiento térmico en las propiedades microestructurales y magnéticas de las muestras estudiadas, arrojando las siguientes conclusiones:

   Existe una estrecha correlación entre la homogeneidad de fase, la microestructura y el contenido de Pr en el estudio. Las muestras con deficiencia de Pr presentan un aspecto microestructural y una composición homogéneos. En contraste, las

composiciones ricas en Pr se fragmentan en granos de 5-25 μm con fases de tipo pirocloro en el centro del grano y fases oxidadas ricas en Pr, mal cristalizadas, en los límites del grano.

El análisis mediante espectroscopia Raman revela la presencia de diferentes tipos de desorden en la subred de oxígeno, dependiendo de la composición y la atmósfera de procesamiento. Las muestras con baja concentración de Pr incorporan oxígeno en sitios inicialmente vacantes para compensar el exceso de carga de Zr^{4+}, mientras que en las muestras ricas en Pr se produce cierto desorden en los oxígenos vecinos a los iones Pr^{3+} o Pr^{4+} que sustituyen a Zr^{4+}, debido a la diferencia de tamaño entre unos cationes y otros.

Las medidas magnéticas indican un contenido notable de Pr^{4+} en la mayoría de las muestras, atribuible a diversos factores, como el estado altamente oxidado del material de partida, la evaporación de Pr y, en composiciones con una proporción molar de praseodimio superior a 0.5, la existencia de fronteras de grano ricas en oxígeno.

2. En el segundo trabajo "L. Grima, J.I. Peña, M.L. Sanjuán, Ceramics with eutectic microstructure in the ZrO_2–PrO_x system. Journal of the American Ceramic Society **106**, 7098–7108 (2023)" se pretende avanzar en el conocimiento del diagrama de fases ZrO_2-PrO_x, por lo que pasamos a estudiar una composición más rica en praseodimio. Hay que señalar que, según publicaciones previas[71, 20, 22, 23], esta es la región más interesante desde el punto de vista catalítico. En este estudio nos centramos en los compuestos eutécticos del sistema ZrO_2–PrO_x, analizando la

sensibilidad de su microestructura, la simetría de las fases formadas y su composición a las variaciones de la atmósfera de procesamiento, desde oxidante hasta reductora. Las muestras se produjeron mediante una técnica de solidificación direccional asistida por láser en atmósferas de O_2, aire, N_2 y 5%H_2 (Ar), y los materiales resultantes fueron analizados mediante SEM/EDX, difracción de rayos X, espectroscopía Raman y susceptibilidad magnética.

Las conclusiones principales de este trabajo son las siguientes:

En aire, N_2 o 5%H_2 (Ar), se forma una microestructura eutéctica de tipo laminar, siendo la fase principal aquella con menor contenido de Pr. Ambas fases eutécticas son de tipo fluorita cuando se procesan en aire, mientras que en N_2 o 5%H_2(Ar), la fase con alto contenido de Pr es del tipo A-R_2O_3, y la fase con bajo contenido de Pr puede describirse como una fase fluorita que contiene regiones ordenadas a corto plazo similares a C-R_2O_3. Los resultados obtenidos para las muestras procesadas en O_2 sugieren que, para valores suficientemente altos de p_{O2}, no se forma ningún eutéctico, en analogía con el sistema ZrO_2–CeO_2.

En cuanto al segundo objetivo de la tesis se publican dos artículos.

1. En el primer artículo, "L. Grima, G.A. Mutch, P.B. Oliete, W. Bucheli, R.I. Merino, E.I. Papaioannou, J.J. Bailey, M.D. Kok, D.J.L. Brett, P.R. Shearing, I.S. Metcalfe, M.L. Sanjuán, High CO_2 permeability in supported molten-salt membranes with highly dense and aligned pores produced by directional solidification, Journal of Membrane Science **630**, 119057 (2021)" describimos la producción de una membrana de separación de gases mediante el uso de una matriz cerámica porosa

obtenida a partir de un eutéctico fibrilar de circona estabilizada con magnesio (MgSZ) solidificado direccionalmente. Tal como se ha descrito más arriba, las fibras de MgO se eliminaron mediante ataque ácido con HCl para crear una matriz porosa con poros altamente alineados, con diámetros de aproximadamente 1 μm.

La tomografía nano-computarizada de rayos X de una porción central del soporte reveló una porosidad del 21% en volumen, con todos los poros alineados dentro de un margen de 10° y alrededor del 76% percolando en la dirección de permeación de la membrana.

Este porcentaje quiere decir que una parte no despreciable de los poros no percola de lado a lado de la membrana. En la figura 25 se presenta en el caso (a) la situación ideal en la que la totalidad de los poros atraviesan la membrana de lado a lado mientras que en (b) se muestra un esquema de situaciones (fibras no vaciadas, poros no percolantes) que podrían conducir a una menor permeación.

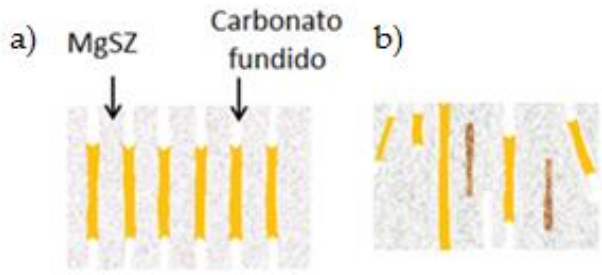

Figura 25. Representación de los canales generados por la disolución de MgO, (a) situación ideal en la que todos los poros son percolantes, (b) situación real en que se observan poros no vaciados y poros no percolantes.

Utilizando esta matriz como soporte para una membrana de carbonatos fundidos, obtuvimos una permeabilidad de CO_2 notablemente elevada, alcanzando $1.41x10^{-10}$

mol m^{-1} s^{-1} Pa^{-1} a 815 °C. Este valor se sitúa entre los más altos reportados para membranas de carbonato fundido soportadas (generalmente en el rango de 10^{-12} a 10^{-10} mol m^{-1} s^{-1} Pa^{-1} a temperaturas similares). En la tabla 1 observamos algunos de los valores de permeabilidad reportados para membranas del mismo tipo, comparados con los valores obtenidos en este trabajo.

Referencia	Material de sustrato	T (°C)	Espesor (μm)	Flujo ($mL.cm^{-2}.min^{-1}$)	Permeabilidad ($mol.m^{-1}.s^{-1}.Pa^{-1}$)
72	YSZ	850	200-400	0.047	9×10^{-12}
73	YSZ on BYS	650	10	0.524	7.69×10^{-13}
74	Al_2O_3 +Ag	650	500	1.25	9.4×10^{-11}
75	SDC		1500	__	1.52×10^{-10}
76	SDC + NiO	700	__	2	$\sim 4 \times 10^{-10}$
77	SDC/BYS	900	120	2.05	$Pce = 3.16 \times 10^{-7}$
78	SDC hollow	700	100-150	4.76	1.06×10^{-10}
79	MgSZ	815	2000	0.47	1.41×10^{-10}

Tabla 1. Valores de flujo, permeabilidad y permeancia de CO2 para membranas duales reportados anteriormente.

Algunos resultados obtenidos para el flujo de CO_2 y O_2 no podían explicarse por la expresión (9), por lo que concluimos que el mecanismo basado en las reacciones (7) y (8) era insuficiente para describir dichos resultados y que estos podían deberse a otras contribuciones, por ejemplo reacciones superficiales en las intercaras entre el soporte y la sal fundida junto con el transporte de CO_2 mediado por iones de pirocarbonato $C_2O_5^{2-}$,[80] formados a través de la reacción 16 en la superficie:

$$CO_2\,(g) + CO_3^{2-}\,(l) \rightleftarrows C_2O_5^{2-} \qquad (16)$$

junto con la reacción 17:

$$C_2O_5^{2-}\,(l) + O^{2-}\,(so) \rightarrow 2CO_3^{2-}\,(l) \qquad (17)$$

Una combinación de las reacciones (6), (16) y (17) podría explicar la permeación y, al mismo tiempo, tener en cuenta la probable participación de la conducción iónica del óxido sólido. Aunque en esta etapa esta conclusión no es más que una hipótesis, está respaldada por las características del soporte de MgSZ utilizado como son un factor de tortuosidad reducido debido a la alineación casi paralela de los poros, la alta densidad de poros y su tamaño micrométrico.

Con este trabajo se ha demostrado, por tanto, que las membranas duales fabricadas de este modo alcanzan una permeabilidad elevada, lo cual se atribuyó a las excelentes características microestructurales de los poros y del óxido sólido. Estas propiedades son específicas del proceso de preparación de solidificación direccional y se suman a las propiedades comunes de las membranas de sales fundidas soportadas, como la idoneidad para operaciones a alta temperatura y una selectividad CO_2/N_2 muy elevada.

2. En el segundo artículo "L. Grima, M. Díaz-Pérez, J. Gil Cortés, D. Sola, J.I. Peña, Generation of a porous scaffold with a starting composition in the CaO-SiO_2-MgO-P_2O_5 system in a simulated physiological environment, Applied Sciences 10, 312 (2020)" se emplea la técnica de zona flotante con láser (LFZ) para la elaboración de un material cristalino denso con la composición que se indica en la tabla 2.

	MgO	**SiO_2**	**$CaSiO_3$**	**TCP**
% peso	36.6	14	18.7	30.7

Tabla 2. Composición del material fabricado como sustitutivo óseo.

Tras el procesado láser se obtiene una estructura que presenta una fase reabsorbible de MgO y otras fases bioactivas. Este material, cuando se encuentra en condiciones fisiológicas, demuestra tener la capacidad de generar un implante poroso controlado mediante la disolución de la fase de MgO, logrando así integrar las ventajas mecánicas de un material denso con las propiedades biológicas inherentes a un andamio poroso.

5. Conclusiones Finales

En resumen, en este trabajo se presentan cuatro estudios distintos, pero interrelacionados a través de la técnica de preparación de los materiales. Dos de ellos están dirigidos a mitigar la emisión de gases contaminantes a la atmósfera y otros dos orientados a la fabricación mediante fusión con láser de materiales densos con óxido de magnesio que, tras su disolución, den lugar a estructuras porosas aplicables en diferentes campos relacionados con la salud y el medio ambiente.

En "L. Grima, J.I. Peña, M.L. Sanjuán, Pyrochlore-like ZrO_2-PrO_x compounds: The role of the processing atmosphere in the stoichiometry, microstructure and oxidation state, Journal of Alloys and Compounds **923**, 166449 (2022)" y "L. Grima, J.I. Peña, M.L. Sanjuán. Ceramics with eutectic microstructure in the ZrO_2–PrO_x system. Journal of the American Ceramic Society **106**, 7098–7108 (2023)", se investigó la interrelación entre la composición, estructura, propiedades y estado de oxidación de muestras pertenecientes al sistema PrO_x-ZrO_2, llegando a la conclusión de que existe una estrecha correlación entre la homogeneidad de fase, la microestructura y el contenido de Pr así como su estado de oxidación.

El análisis mediante espectroscopia Raman ha revelado la presencia de diversos tipos de desorden de oxígeno, dependiendo de la composición y la atmósfera de procesado. En las muestras con baja concentración de Pr, se observa la entrada de oxígeno en sitios inicialmente vacantes para compensar el exceso de carga de Zr^{4+}, mientras que en las muestras ricas en Pr, el desorden de oxígeno ocurre alrededor de los iones Pr^{3+} o Pr^{4+} que sustituyen a $Zr^{4+,}$ debido a la discrepancia de tamaño. Se ha confirmado la presencia significativa de Pr^{4+} en las muestras.

Estos resultados contribuyen de manera significativa al entendimiento de las propiedades fundamentales del sistema PrO_x-ZrO_2 y ofrecen información valiosa para el diseño de materiales con aplicaciones destinadas a la reducción de emisiones atmosféricas.

Adicionalmente, en los dos estudios subsecuentes, "L. Grima, G.A. Mutch, P.B. Oliete, W. Bucheli, R.I. Merino, E.I. Papaioannou, J.J. Bailey, M.D. Kok, D.J.L. Brett, P.R. Shearing, I.S. Metcalfe, M.L. Sanjuán, High CO_2 permeability in supported molten-salt membranes with highly dense and aligned pores produced by directional solidification, Journal of Membrane Science **630**, 119057 (2021)" y "L. Grima, M. Díaz-Pérez, J. Gil Cortés, D. Sola, J.I. Peña, Generation of a porous scaffold with a starting composition in the CaO-SiO_2-MgO-P_2O_5 system in a simulated physiological environment, Applied Sciences 10, 312 (2020)", se buscó la fabricación de materiales densos mediante fusión con láser que contuvieran óxido de magnesio y, tras la disolución de este componente, dieran lugar a estructuras porosas aplicables en diversos campos relacionados con la salud y el medio ambiente. En el primer estudio, se logró la fabricación mediante fusión zonal láser

de una membrana dual capaz de permitir la permeación selectiva de CO_2 a través de la misma. Los valores obtenidos superaron los resultados previamente reportados para membranas de características similares.

En el segundo estudio, se obtuvo un material aplicable en sustitución ósea con una parte biorreabsorbible y otra bioactiva. Este material, al entrar en contacto con sistemas fisiológicos, genera un implante óseo poroso, in-situ, gracias a la disolución de la fase biorreabsorbible (MgO), que satisface tanto los requerimientos mecánicos como los biológicos de un implante, marcando así un avance significativo en el desarrollo de biomateriales innovadores.

Los resultados de estos trabajos ponen de manifiesto la versatilidad de la técnica de solidificación direccional asistida por láser para producir materiales con funcionalidades muy variadas. En algunos casos (óxidos para soportes de membranas duales o andamiajes con aplicaciones biomédicas) la técnica proporciona directamente el material utilizable, tras la adecuada preparación. En otros casos (óxidos del sistema ZrO_2-PrO_x) las temperaturas alcanzadas durante el procesado permiten acceder a regiones del diagrama de fases sobre las que todavía hay incertidumbre, lo que puede ser útil para entender el comportamiento de estos materiales en las condiciones reales de funcionamiento.

6. Bibliografía

[1] IPCC, Informe de Síntesis 2014.

[2] M. J. Ramírez-Moreno et al., Alkaline and Alkaline-Earth Ceramic Oxides for CO_2 Capture, Separation and Subsequent Catalytic Chemical Conversion, en CO_2

Sequestration and Valorization, editado por Claudia do Rosario Vaz Morgado y Victor Paulo Pecanha Esteves

[3] D. Chery, V. Lair and M. Cassir, Overview on CO_2 valorization: challenge of molten carbonates. *Front. Energy Res.*, **3**, 43 (2015).

[4] R. Agarwal, A.J. García, Biomaterial strategies for engineering implants for enhanced osseointegration and bone repair. *Adv. Drug Deliv. Rev.*, ***94***, 53–62 (2015).

[5] H.W. Kim, H.E. Kim, V. Salih, Stimulation of osteoblast responses to biomimetic nanocomposites of gelatin-hydroxyapatite for tissue engineering scaffolds. Biomaterials, **26**, 5221–5230 (2005).

[6] G. Wei, P.X. Ma, Structure and properties of nano-hydroxyapatite/polymer composite scaffolds for bone tissue engineering. Biomaterials, **25**, 4749–4757 (2003).

[7] K.Y. Leong, K.Z. Ku Ahmad, Hwai Chyuan Ong, M.J. Ghazali, Azizah Baharum, Synthesis and thermal conductivity characteristic of hybrid nanofluids – A review, Renewable and Sustainable Energy Reviews, **75**, 868-878 (2017).

[8] R. J. Gorte, AIChE Journal **56**, 1127 (2010).

[9] A. Trovarelli, editor. Catalysis by ceria and related materials, Catalytic science series, vol. 2. London: Imperial College Press; 2002.

[10] P. Fornasiero et al., J. Catal. **151**,168 (1995).

[11] J. Kašpar, P. Fornasiero, Nanostructured materials for advanced automotive de-pollution catalysts, Journal of Solid State Chemistry, **171**, 1–2, 19-29 (2003).

[12] R. Di Monte y J. Kaspar, J. Mater. Chem. **15**, 633-648 (2005).

[13] M. Yashima, T. Hirose, S. Katano, Y. Suzuki, M. Kakihana, y M. Yoshimura, Structural changes of ZrO_2-CeO_2 solid solutions around the monoclinic-tetragonal phase boundary, Phys. Rev. B **51**, 8018 (1995).

[14] C.K. Narula, L.P. Haack, W. Chun, H. W. Jen, G.W. Graham, Single–phase PrO_y–ZrO_2 materials and their oxygen storage capacity: a comparison with single–phase CeO_2–ZrO_2, PrO_y–CeO_2, and PrO_y–CeO_2–ZrO_2, Mater. J. Phys. Chem. B **103**, 3634–3639 (1999).

[15] QY. Wang, GF. Li, B. Zhao, RX. Zhou, Investigation on properties of a novel ceria-zirconia-praseodymia solid solution and its application in Pd-only three-way catalyst for gasoline engine emission control. FUEL, **90**, 10, 3047- 3055 (2011).

[16] J.R. McBride, K.C. Hass, B.D. Poindexter, W.H. Weber, Raman and x-ray studies of $Ce_{1-x}RE_xO_{2-y}$, where RE=La, Pr, Nd,Eu, Gd, and Tb. J Appl Phys, **76**, 2435–2435 (1994).

[17] Xiaodi Wu, Xiaodong Wu, Qing Liang, Jun Fan, Duan Weng, Zhi Xie, Shiqiang Wei, Structure and oxygen storage capacity of Pr/Nd doped CeO_2–ZrO_2 mixed oxides, Solid State Sciences, **9**, 7, 636-643 (2007).

[18] Rui RAN, Duan WENG, Xiaodong WU, Jun FAN, Lei WANG, Xiaodi WU, Structure and oxygen storage capacity of Pr-doped $Ce_{0.26}Zr_{0.74}O_2$ mixed oxides, Journal of Rare Earths, **29**, 11, 1053-1059 (2011).

[19] H. He, H.X. Dai, C.T. Au, Defective structure, oxygen mobility, oxygen storage capacity, and redox properties of RE–based (RE = Ce, Pr) solid solutions, Catal. Today, **90**, 245–254 (2004).

[20] J. Abel, M. Lamirand–Majimel, J. Majimel, V. Belliere–Baca, V. Harle, G. Andre, C. Prestipino, S. Figueroa, E. Durand, A. Demourges, Oxygen non–stoichiometry phenomena in $Pr_{1-x}Zr_xO_{2-y}$ compounds ($0.02 < x < 0.5$), Dalton Trans. **43**, 15183–15191 (2014).

[21] M.B. Bellakki, C. Shivakumara, T. Baidya, A.S. Prakash, N.Y. Vasanthacharya, M.S. Hegde, Synthesis, structure and oxygen–storage capacity of Pr1−xZrxO2-δ and Pr1−x-yPdyZrxO2-δ, Mater. Res. Bull. **43**, 2658–2667 (2008).

[22] M.Y. Sinev, G.W. Graham, L.P. Haack, M. Shelef, Kinetic and structural studies of oxygen availability of the mixed oxides Pr1–xMxOy (M = Ce, Zr), J. Mater. Res. **11**, 1960–1971 (1996).

[23] A.V. Shlyakhtina, J.C.C. Abrantes, E. Gomes, A.N. Shchegolikhin, G.A. Vorobieva, K.I. Maslakov, A.V. Knotko, L.G. Shcherbakova, Effect of Pr^{3+}/Pr^{4+} ratio on the oxygen ion transport and thermomechanical properties of the pyrochlore and fluorite phases in the ZrO_2–Pr_2O_3 system, Int. J. Hydrog. Energ. **41**, 9982–9992 (2016).

[24] A. Rouanet, Contribution a l'etude des systemes zirconia—oxydes des lanthanides au voisinage de la fusion: Memoire de these, Rev. Intern. Hautes Temper. Refract. **8**, 161–180 (1971).

[25] M.D. Krasil'nikov, I.V Vinokurov, S. D. Nikitina, "Physicochemical properties of solid solutions in the zirconium dioxide- praseodymium oxide system in air", Fiz. Khim. Rasplavov Tverd. Elektrolitov, 7th, **3**, 123-125 (1979).

[26] M.A. Subramanian, G. Aravamudan, G.V. Subba Rao, Oxide pyrochlores – a review, Prog. Solid State Chem. **15**, 55–143 (1983).

[27] W.A. Tiller. "Polyphase solidification". Liquid metals and solidification. American Society for Metals, Cleveland, 276-318, (1958).

[28] K.A. Jackson y J.D. Hunt. "Lamelar and roc eutectic growth". *Transactions of the Metallurgical Society of AIME*. **236,** 8, 1129-1142, (1966).

[29] T. Gasser, C. Guivarch, K. Tachiiri, C. D. Jones and P. Ciais, *Nat. Commun.*, **6**, 1–7 (2015).

[30] M. Bui, C. S. Adjiman, A. Bardow, E. J. Anthony, A. Boston, S. Brown, P. S. Fennell, S. Fuss, A. Galindo, L. A. Hackett, H. J. Herzog, G. Jackson, J. Kemper, S. Krevor, G. C. Maitland, M. Matuszewski, I. S. Metcalfe, C. Petit, G. Puxty, J. Reimer, D. M. Reiner, E. S. Rubin, S. A. Scott, N. Shah, B. Smit, J. P. M. Trusler, P. Webley, J. Wilcox and N. MacDowell, *Energy Environ. Sci.*, **11**, 1062–1178 (2018).

[31] G. T. Rochelle, Amine Scrubbing for CO_2 Capture, Science, **325**, 5948, 1652–1654 (2009).

[32] R. S. Haszeldine, Carbon Capture and Storage: How Green Can Black Be?, Science, **325**, 1647–1652 (2009).

[33] S. Choi, J. H. Drese y C. W. Jones, Adsorbent Materials for Carbon Dioxide Capture from Large Anthropogenic Point Sources, ChemSusChem, **2**, 796–854 (2009).

[34] B. Arias, M. E. Diego, J. C. Abanades, M. Lorenzo, L. Diaz, D. Martinez, J. Alvarez and A. Sanchez-Biezma, Demonstration of steady state CO_2 capture in a 1.7 MW_{th} calcium looping pilot, Int. J. Greenh. Gas Control, **18**, 237–245 (2013).

[35] M. Chang, W. Chen, C. Huang, W. Liu, W. Chang, W. Chen, J. Cheng, K. Huang and H. Hsu, Design and Experimental Testing of a 1.9MW_{th} Calcium Looping Pilot Plant, Energy Procedia, **63**, 2100–2108 (2014).

[36] H. A. J. Van Dijk, P. D. Cobden, M. Lundqvist, C. C. Cormos, M. J. Watson, G. Manzolini, S. Van Der Veer, L. Mancuso, J. Johns and B. Sundelin, Cost Effective CO_2 Reduction in the Iron & Steel Industry by Means of the SEWGS Technology: STEPWISE Project, Energy Procedia, **114**, 6256– 6265 (2017).

[37] S. Tonomura, Outline of Course 50, Energy Procedia, **37**, 7160–7167 (2013).

[38] C. Gebald, J. A. Wurzbacher, P. Tingaut, T. Zimmermann and A. Steinfeld, Amine-based nanofibrillated cellulose as adsorbent for CO_2 capture from air, Environ. Sci. Technol., **45**, 9101–9108 (2011).

[39] T. Nguyen, *Chem. Eng. News*, 2017, 15.

[40] X. Jiang, J. Zhu, Z. Liu, S. Guo and W. Jin, *Ind. Eng. Chem. Res.*, 2016, **55**, 3300–3307.

[41] J. Ortiz-Landeros, T. Norton, Y.S. Lin, Effects of support pore structure on carbon dioxide permeation of ceramic-carbonate dual-phase membranes, Chem. Eng. Sci., **104** 891–898 (2013).

[42] G. A. Mutch, L. Qu, G. Triantafyllou, W. Xing, M. Fontaine and I. S. Metcalfe, Supported molten-salt membranes for carbon dioxide permeation, J. Mater. Chem. A, **7**, 21, 12951-12973 (2019).

[43] Bo. Lu and Y. S. Lin, Synthesis and characterization of thin ceramic-carbonate dual-phase membranes for carbon dioxide separation, J. Memb. Sci., **444**, 402–411 (2013).

[44] M. Anderson and Y. S. Lin, Carbonate–ceramic dual-phase membrane for carbon dioxide separation, J. Memb. Sci., **357**, 122–129 (2010).

[45] J. Llorca, V.M. Orera, Directionally solidified eutectic ceramic oxides, Prog. Mater. Sci. **51**, 6, 711–809 (2006).

[46] Phase Equilibria Diagrams Online Database (NIST Standard Reference Database 31), The American Ceramic Society and the National Institute of Standards and Technology, 2020. Figure Number Zr-076-A.

[47] J. Echigoya, H. Suto, S. Hayashi, Growth morphology and orientation relationships in directionally solidified MgO-ZrO_2 eutectic, Trans. Jpn. Instit. Metals, **26**, 895–900 (1985).

[48] F.L. Kennard, R.C. Bradt, V.S. Stubican, Directional solidification of ZrO_2-MgO eutectic, J. Am. Ceram. Soc. **57**, 428–431 (1974).

[49] G. Fiquet, P. Richet, G. Montagnac, High-temperature thermal expansion of lime, periclase, corundum and spinel, PhysChem. Min., 27, 103–111 (1999).

[50] Y. Shiratori, F. Tietz, H.P. Buchkremer, D. St¨over, YSZ–MgO composite electrolyte with adjusted thermal expansion coefficient to other SOFC components, Solid State Ionics, **164,** 27–33 (2003).

[51] V.M. Orera, R.I. Merino, J.A. Pardo, A. Larrea, J.I. Pe˜na, C. Gonz´alez, P. Poza, J. Y. Pastor, J. Llorca, Microstructure and physical properties of some oxide eutectic composites processed by directional solidification, Acta Mater., **48**, 4683–4689 (2000).

[52] D. Sola, P.B. Oliete, R.I. Merino, J.I. Pe˜na, Directionally solidified Ni doped MgO-MgSZ eutectic composites for thermophotovoltaic devices, J. Eur. Ceram. Soc., **39,** 1206–1213 (2019).

[53] S.P.S. Badwal, Zirconia-based solid electrolytes: microstructure, stability and ionic conductivity, Solid State Ionics, **52**, 23–32 (1992).

[54] R.I. Merino, V.M. Orera, J.I. Peña, G.F. de la Fuente, Conductivity anisotropy in directionally solidified $CaZrO_3$-CaSZ and MgO-MgSZ eutectics, Solid State Ionics, **100,** 313–318 (1997).

[55] L. Roseti, V. Parisi, M. Petretta, C. Cavallo, G. Desando, I. Bartolotti, B. Grigolo, Scaffolds for Bone Tissue Engineering: State of the art and new perspectives, Mater. Sci. Eng., **78**, 1246–1262 (2017).

[56] P.N. De Aza, J.I. Peña, Z.B. Luklinska, L. Meseguer-Olmo, Bioeutectic® Ceramics for Biomedical Application Obtained by Laser Floating Zone Method. In vivo Evaluation. Materials, **7**, 2395–2410 (2014).

[57] D. Sola, D. Paulés, L. Grima, J. Anzano, Laser-Induced Breakdown Spectroscopy (LIBS) for Monitoring the Formation of Hydroxyapatite Porous Layers. Materials, **10**, 1395–1401 (2017).

[58] I.H. García-Páez, P. Pena, C. Baudín, M.A. Rodríguez, E. Cordoba, A.H. De Aza, Processing and in vitro bioactivity of a β-$Ca_3(PO_4)_2$–$CaMg(SiO_3)_2$ ceramic with the eutectic composition, Bol. Soc. Esp. Ceram. Vidr., **55**, 1–12 (2016).

[59] M.A. Sainz, P. Pena, A. Serena, A. Caballero, Influence of design on bioactivity of novel $CaSiO_3$–$CaMg(SiO_3)_2$ bioceramics: In vitro simulated body fluid test and thermodynamic simulation. Acta Biomater., **6**, 2797–2807 (2010).

[60] M. Magallanes-Perdomo, A.H. De Aza, I. Sobrados, J. Sanz, P. Pena, Structure and properties of bioactive eutectic glasses based on the $Ca_3(PO_4)_2$–$CaSiO_3$–$CaMg(SiO_3)_2$ system. Acta Biomater., **8**, 820–829 (2012).

[61] Z. Qizhi, I.D. Chen, A.R. Thompson, 45S5 Bioglasss-derived glass–ceramic scaffolds for bone tissue engineering. Biomaterials, **27**, 2414–2425 (2006).

[62] I. Sabree, J.E. Gough, B. Derby, Mechanical properties of porous ceramic scaffolds: Influence of internal dimensions. Ceram. Int., **41**, 8425–8432 (2015).

[63] P. Ma, G. Wei, Nanoestructured scaffolds for tissue engineering and regeneration. Handb. Nanostructured Biomater. Appl. Nanobiotechnol., **1**, 1–21 (2005).

[64] K. Rezwan, Q.Z. Chen, J.J Blaker, R. Boccaccini, Biodegradable and bioactive porous polymer/inorganic composite scaffolds for bone tissue engineering. Biomaterials, **27**, 3413–3431 (2006).

[65] A.J. Salgado, O.P. Coutinho, R.L. Reis, Bone tissue engineering: State of the art and future trends. Macromol. Biosci., **4**, 743–765 (2004).

[66] M. Diba, O.M. Goudouri, F. Tapia, A.R. Boccaccini, Magnesium-containing bioactive polycrystalline silicate-based ceramics and glass-ceramics for biomedical applications. Curr. Opin. Solid State Mater. Sci., **18**, 147–167 (2014).

[67] C. Wu, J. Chang, J. Wang, S. Ni, W. Zhai, Preparation and characteristics of a calcium magnesium silicate (bredigite) bioactive ceramic. Biomaterials, **26**, 2925–2931 (2005).

[68] T. Kokubo, H. Kushitani, S. Sakka, T. Kitsugi, T. Yamamuro, Solutions able to reproduce in vivo surface-structure changes in bioactive glass-ceramics A-W, J. Biomed. Mater. Res., **24**, 721–734 (1990).

[69] A. Oyanete, H. Kim, T. Furuya, T. Kokubo, T. Miyazaki, T. Nakamura, Preparation and assessment of revised simulated body fluid. J. Biomed. Mater. Res. A, **65**, 188–195 (2003).

[70] J. Rodriguez-Carvajal, FULLPROF: A Program for Rietveld Refinement and Pattern Matching Analysis, Abstracts of the Satellite Meeting on Powder Diffraction of the XV Congress of the IUCr, p. 127, Toulouse, France (1990).

[71] L. Grima, J.I. Peña, M.L. Sanjuán, Pyrochlore-like ZrO_2-PrO_x compounds: The role of the processing atmosphere in the stoichiometry, microstructure and oxidation state, Journal of Alloys and Compounds **923**, 166449 (2022).

[72] J.L. Wade, C. Lee, A.C. West, K.S. Lackner, Composite electrolyte membranes for high temperature CO2 separation, J. Membr. Sci., **369,** 20–29 (2011).

[73] B. Lu, Y.S. Lin, Synthesis and characterization of thin ceramic-carbonate dual-phase membranes for carbon dioxide separation, J. Membr. Sci., **444**, 402–411 (2013).

[74] L.A. McNeil, G.A. Mutch, F. Iacoviello, J.J. Bailey, G. Triantafyllou, D. Neagu, T. S. Miller, E.I. Papaioannou, W. Hu, D.J.L. Brett, P.R. Shearing, I.S. Metcalfe, Dendritic

silver self-assembly in molten-carbonate membranes for efficient carbon dioxide capture, Energy Environ. Sci., **13,** 1766–1775 (2020).

[75] T.T. Norton, Y.S. Lin, Ceramic-carbonate dual-phase membrane with improved chemical stability for carbon dioxide separation at high temperature, Solid State Ionics, **263**, 172–179 (2014).

[76] L. Zhang, N. Xu, X. Li, S. Wang, K. Huang, W.H. Harris, W.K.S. Chiu, High CO_2 permeation flux enabled by highly interconnected three dimensional ionic channels in selective CO_2 separation membranes, Energy Environ. Sci., **5,** 8310–8317 (2012).

[77] X. Dong, H.C. Wu, Y.S. Lin, CO_2 permeation through asymmetric thin tubular ceramic-carbonate dual-phase membranes, J. Membr. Sci., **564,** 73–81 (2018).

[78] T. Chen, Z. Wang, J. Hu, M.H. Wai, S. Kawi, Y.S. Lin, High CO_2 permeability of ceramic-carbonate dual-phase hollow fiber membrane at medium-high temperature, J. Membr. Sci., **597,** 117770 (2020).

[79] L. Grima, G.A. Mutch, P.B. Oliete, W. Bucheli, R.I. Merino, E.I. Papaioannou, J.J. Bailey, M.D. Kok, D.J.L. Brett, P.R. Shearing, I.S. Metcalfe, M.L. Sanjuán, High CO_2 permeability in supported molten-salt membranes with highly dense and aligned pores produced by directional solidification, Journal of Membrane Science **630**, 119057 (2021).

[80] L. Zhang, X. Huang, C. Qin, K. Brinkman, Y. Gong, S. Wang, K. Huang, First spectroscopic identification of pyrocarbonate for high CO_2 flux membranes containing highly interconnected three dimensional ionic channels, Phys. Chem. Chem. Phys., **15**, 13147–13152 (2013).